2016

COHERENT MAGNETIZATION DYNAMICS IN NANOSTRUCTURES AND THIN FILMS

GONZÁLEZ FUENTES, CLAUDIO ALEJANDRO

Universidad Técnica Federico Santa María
Departamento de Física
Valparaíso-Chile

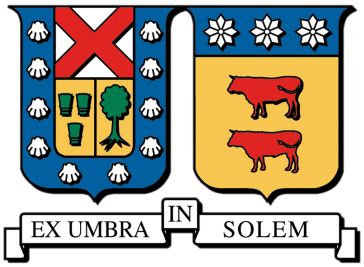

Coherent Magnetization Dynamics in Nanostructures and Thin Films

Tesis de grado presentada por
Claudio Alejandro González Fuentes

Como requisito parcial para optar al grado de
Doctor en Física

Profesor Guía
Pedro Landeros Silva
co-dirigida por
Ricardo Henríquez Correa
Carlos García García

12 de Octubre de 2016

Informe de aprobación
Tesis de Doctorado

Se informa a la Dirección de Postgrado que la Tesis de Doctorado presentada por el candidato

Claudio González Fuentes

ha sido aprobada por la Comisin de Evaluación de la tesis como requisito para optar al grado de Doctor en Física, en el examen de defensa de tesis rendido el día 12 de Octubre de 2016.

Niembros de la comisión:

Dr. Pedro Landeros Silva _____
Universidad Técnica Federico Santa María

Dr. Carlos García García _____
Universidad Técnica Federico Santa María

Dr. Ricardo Henríquez Correa _____
Universidad Técnica Federico Santa María

Dr. Roberto Rodríguez Suárez _____
Universidad Católica de Chile

Abstract

This thesis is a compendium of theoretical and experimental works on ferromagnetic resonance (FMR) in uniformly magnetized nanostructures and thin films.
In the theoretical part, supervised by Dr. Pedro Landeros, a very general and comprehensive model to find the full set of equilibrium states and their stabilities under the action of spin polarized currents is presented. This model allows to find the regime of steady-state oscillations of the magnetization and build complete phase diagrams Moreover, a general model of the detection of the ferromagnetic resonance in nanostructures by the spin rectification effect is presented, which accounts for the excitation of FMR both by spin polarized currents and voltage controlled magnetic anisotropy. The model is successful to explain many published results on this subject.
In the experimental part, supervised by Drs. Carlos García and Ricardo Henríquez, a new methodology for a more precise determination of the spectroscopic g-factor in thin films in FMR experiments, is presented. The results are promising in order to solve the great discrepancy in the values of g that can be found in the literature. FMR was also employed for a study of the intensity of perpendicular magnetic anisotropy (PMA) in CoFeB/Pd multilayers. It was found that there is a critical thickness of Pd for which net PMA appears and that the intensity of the PMA increases with the number of repetitions. These results have been attributed to the continuity of the CoFeB/Pd interface and to the varying PMA intensity as more interfaces are deposited.

Acknowledgements

This thesis was mainly supported by CONICYT PhD Scholarship 21110732, USM-PIIC grant and "Anillos de Investigación en Ciencia y Tecnología" 11063 of CCTVAL. I would also want to acknowledge funding from "FONDECYT de Iniciación en Investigación" 11140787, granted to professor Ricardo Henríquez, "FONDECYT Regular" 1140552, granted to professor Carlos García, and USM-DGIP 11.12.17 granted to professor Pedro Landeros.

Contents

List of Figures

List of Tables

Publications

List of papers included in this thesis:

I **C. Gonzalez-Fuentes**, R. A. Gallardo, and P. Landeros. "Role of polarizer-tilting-angle in zero-field spin-transfer nano-oscillators with perpendicular anisotropy", Applied Physics Letters, Vol. 107, pp. 142402, (October2015)

II A.F. Franco, **C Gonzalez-Fuentes**, R. Morales, C. A. Ross, R. Dumas, J. Åkerman and C. Garcia. "Variable variance Preisach model for multilayers with perpendicular magnetic anisotropy", Physical Review B, Vol. 94, pp. 064431, (August 2016)

III **C. Gonzalez-Fuentes**, J. B. Gonzalez-Diaz, L. Fallarino, J. A. Arregi and A. Berger. "Influence of the light incidence angle on the precision of generalized magneto-optical ellipsometry", Journal of Magnetism and Magnetic Materials, Vol. 386, pp. 150, (March 2015)

IV R. Henriquez, **C. Gonzalez-Fuentes**, J. Correa-Puerta, V. Del Campo, L. Moraga, M. Flores, S. Donoso, F. Marína, S. Bravo, R. Segura and Patricio Häberle. "Effect of electron-surface scattering and thiol adsorption on the electrical resistivity of metallic ultra thin films", Submitted to Applied Surface Science, (September 2015)

Symbols and acronyms

FM	Ferromagnet: single domain ferromagnetic body
$\mathbf{m}$	Unitary vector of the free layer magnetization
γ	Gyromagnetic ratio
γ^*	$\mu_0\gamma$
$\mathbf{m}$	Unitary vector of the free layer magnetization
$\mathbf{p}$	Unitary vector of the polarizer layer magnetization
θ	Relative angle between $\mathbf{m}$ and $\mathbf{p}$
FMR	Ferromagnetic resonance
$\mathbf{H}$	Applied magnetic field
$\mathbf{H}^{\mathrm{e}}$	Effective field
M_s	saturation magnetization
M_{eff}	effective magnetization
α	Gilbert damping constant
LLG	Landau-Lifshitz-Gilbert
LLGS	Landau-Lifshitz-Gilbert-Slonczewski
SV	Spin valve
MTJ	Magnetic tunnel junction
STT	Spin transfer torque
PMA	Perpendicular magnetic anisotropy
H_s	PMA field intensity
IPA	In-plane uniaxial anisotropy
H_u	IPA field intensity
IP-STT	In-plane STT, also called Slonczewsky STT
$\beta_{\parallel}$	IP-STT magnitude
FL-STT	Field-like STT, also called out-of-plane STT
$\beta_{\perp}$	FL-STT magnitude
SSO	Steady state oscillations
SRE	Spin rectification effect
VCMA	Voltage controlled PMA
β_V	VCMA field magnitude
VVPM	Variable variance Preisach model
AMG	Alternating field gradient magnetometry

Introduction

Motivation

Spintronics, or spin electronics, is an emerging technology which takes advantage of the electron's spin degree of freedom to extend, complement and overcome the limitations of the traditional electronics, that exploit only the electron's charge degree of freedom. The birth of the spintronics may be found on the pioneering discoveries regarding spin-dependent transport properties on solids during late 80s, remarkably the giant magnetoresistance (GMR) effect [1, 2], whose discovery was awarded with the 2007 Nobel prize in physics. In the 90s great progress was done on improvement of the GMR materials, leading to the application of GMR on commercial hard disk drives, which substantially increased the bit-per-area density on such devices . In 1996 Slonczwesky [3] and Berger [4] predicted that is possible to manipulate the magnetization orientation on ferromagnets (FMs) through spin polarized currents outgoing from another ferromagnet. This phenomenon is called the Spin Transfer Torque (STT). Shortly thereafter, STT was confirmed by several experiments [5–7]. This groundbreaking discovery aimed numerous research and found an application on the recently developed STT-RAM devices [8]. Despite the enormous advances in the field of spintronics, there are still important issues yet to be solved, like the large amount of currents needed to manipulate the magnetization, the thermal stability of the memory elements and their unwanted stray fields.
A fundamental characterization technique for the current research in spintronics is the ferromagnetic resonance (FMR) spectroscopy. For many decades, FMR spectroscopy has been carried out using single frequency microwave cavities [9]. More recently, the apparition of broadband FMR spectroscopy have meant a qualitative jump in the efficiency of FMR to extract material parameters from ferromagnetic thin films. Moreover, the recent discovery of the spin rectification effect (SRE) has allowed to perform FMR spectroscopy on nanometric structures.
This thesis presents a theoretical and experimental investigation aimed to the improvement of these FMR techniques as well as a study of the valuable information that can be obtained from them. In the following sections we are going to introduce some concepts that are fundamental for the subjects addressed in this thesis, to finally give out a general outline of the upcoming chapters.

Larmor's precession and ferromagnetic resonance (FMR)

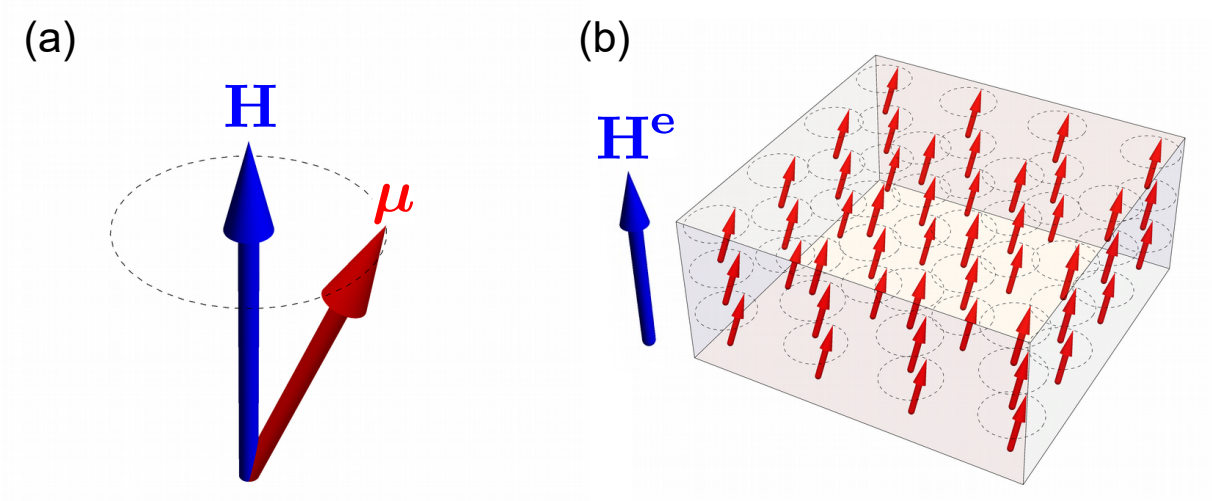

Figure 1: (a) Larmor's precession of an isolated magnetic moments around the external field $\mathbf{H}$. (b) Collective precession of the magnetic moments of a solid around the effective field $\mathbf{H}^{\mathrm{e}}$.

It is well known that a particle that has a fixed magnetic moment vector $\boldsymbol{\mu}$, under a uniform magnetic field $\mathbf{H}$ has a potential energy is given by [10]:

$$U = -\mu_0 \boldsymbol{\mu} \cdot \mathbf{H}, \tag{1}$$

where μ_0 is the vacuum permittivity. The minimum potential energy and most stable orientation for $\boldsymbol{\mu}$ is parallel to $\mathbf{H}$. Let's suppose now that we set $\boldsymbol{\mu}$ in a direction other than $\mathbf{H}$ and let the system to evolve. In absence of dissipative mechanisms, $\boldsymbol{\mu}$ will not directly point to $\mathbf{H}$, instead will trace a perpetual circular orbit around $\mathbf{H}$. This is known as Larmor's precession (see figure 1(a)). The torque on $\boldsymbol{\mu}$ moment is given by:

$$\boldsymbol{\tau} = \frac{d\mathbf{L}}{dt} = \mu_0 \boldsymbol{\mu} \times \mathbf{H},$$

where $\mathbf{L}$ is the mechanical angular momentum of the particle. The ratio between $\mathbf{L}$ and $\boldsymbol{\mu}$ is called the gyromagnetic ratio γ^* and is related to the the ratio between the charge and the mass of the partcle. γ is given by:

$$\gamma = \frac{gq}{2m}, \tag{2}$$

where q and m are the charge and the mass of the particle respectively. g is a dimensionless factor that characterizes the nature of the magnetic moment of the particle. For a classical charged rotating body, one can demonstrate easily that g is equal to 1. This is also true for the magnetic moment generated by the electron's orbital momentum within the atom.

On the other hand, many subatomic particles (and atomic nucleus) have intrinsic magnetic moments, whose origin is not the rotation of electrical charges, instead the origin can be found in the Dirac's equation of relativistic quantum mechanics. The value of g in these particles may differ notably from 1. A well-known case is the electron, which possess an intrinsic magnetic moment or spin that has an associated value of $g = 2$ (exactly 2.0023) with minor corrections arising from quantum field theory.
The precise value of g in elemental particles has a deep importance in since is a test of physical models. In solids the main contribution to the magnetic moment comes from the electron's spin, although orbital magnetic moment may contribute significantly in some cases [11]. In the following, we will use $\mathbf{m}$ for the unit vector pointing in the same direction of the magnetic moment of an isolated electron or an uniformly magnetized ferromagnetic body (FM) . The equation of precession for $\mathbf{m}$, in the case of an isolated electron, will be:

$$\dot{\mathbf{m}} = -\gamma^* \mathbf{m} \times \mathbf{H} \tag{3}$$

where $\gamma^* = \mu_0 \gamma$. The value of γ in this case is obtained from Eq. 2 after replacing q and m with the respective values of elemental charge and electron's mass respectively. The minus sign on the right hand side of 3 comes from the negative charge of the electron. The Larmor's frequency of precession the will be $\omega_L = \gamma \mu_0 H$, with γ =28.04 GHz/T. Since the typical magnetic fields generated in laboratories are up to few T, $\omega_L/2\pi$ falls in the range of few to tens of GHz.
Any physical system that has a natural frequency of oscillation is susceptible to be put in resonance. In this case, it is possible to put $\mathbf{m}$ in resonance with a periodic magnetic field with a frequency close to ω_L. That would be the case of an isolated electron. However, in a FM there are other forces that must be considered, apart from the torque exerted by $\mathbf{H}$:

- The exchange force, that keep the magnetic moments of neighbouring electrons aligned.
- The Magnetostatic fields: the fields generated by the magnetization itself. In a FM the discontinuity of the magnetization at the edges makes up bound magnetic charges that generate magnetic fields.
- The magnetocrystalline anisotropy. A solid with crystalline structure has symmetries that makes more energetically favorable for $\mathbf{m}$ to point in certain directions.

All the above mentioned contributions constitute what is called the effective field $\mathbf{H}^{\mathrm{e}}$. In figure 1(b), $\mathbf{m}$ describes a circular orbit around $\mathbf{H}^{\mathrm{e}}$ analogously to the circular orbit around $\mathbf{H}$ in the Larmor's precession. Ferromagnetic resonance (FMR) is thus, the Larmor's precession extended to FMs.

Landau-Lifshitz-Gilbert equation

Considering the reasons given in the precedent section, the correct equation that describes the temporal evolution of $\mathbf{m}$ in a FM is:

$$\dot{\mathbf{m}} = -\gamma^* \mathbf{m} \times \mathbf{H}^{\mathrm{e}}.$$

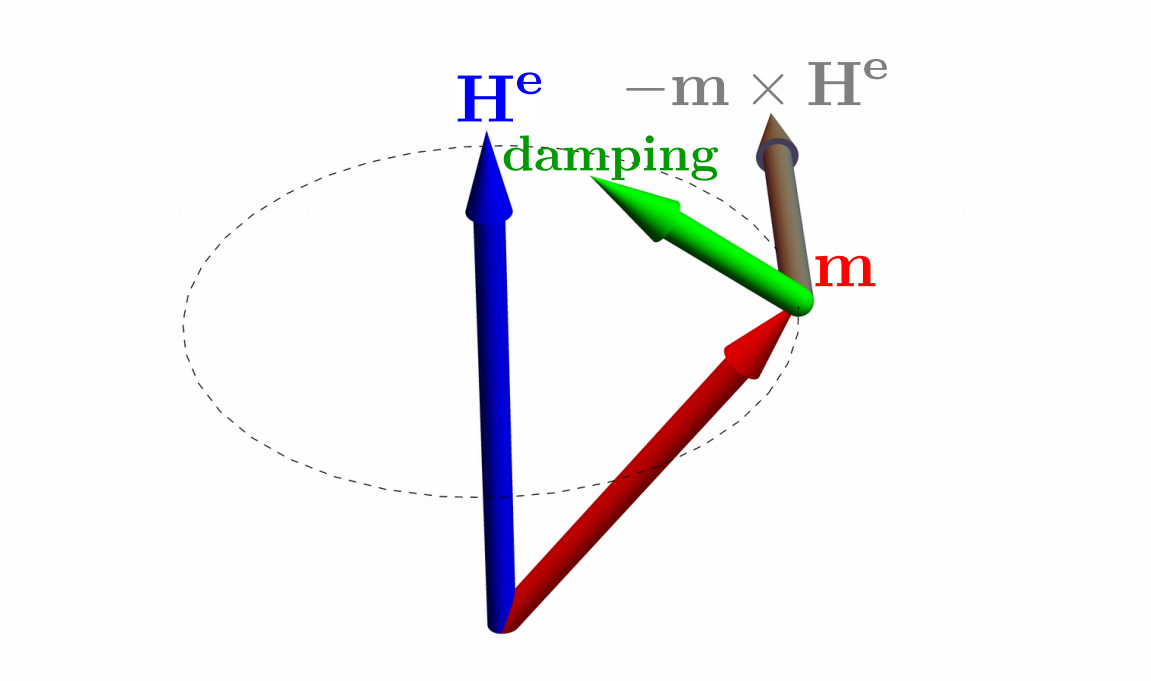

Figure 2: Torques acting on the magnetization of a ferromagnetic body.

Additionally, solids have relaxation mechanisms that dissipate energy, making $\mathbf{m}$ oscillations attenuate and eventually point parallel to $\mathbf{H}^{\mathrm{e}}$. These mechanisms constitute a phenomenological torque called the Gilbert damping. The Gilbert damping makes $\mathbf{m}$ to point in the same direction of $\mathbf{H}_{eff}$ but without altering its magnitude: the appropriate term to fulfill these requirements is $\alpha\mathbf{m}\times\dot{\mathbf{m}}$, as shown in figure 2, where α is a phenomenological constant [12]. The new equation of movement is then:

$$\dot{\mathbf{m}} = \gamma^{*}\mathbf{m} \times \mathbf{H}^{\mathrm{e}} + \alpha\mathbf{m}\times\dot{\mathbf{m}} \tag{4}$$

The above is the Landau-Lifshitz-Gilbert (LLG) equation, which is also valid on a microscopic level for non uniformly magnetized bodies. In such case the exchange forces must be included. However, in this thesis only single domain ferromagnetic bodies are considered, so $\mathbf{m}$ will always be assumed to be uniform inside.

Perpendicular magnetic anisotropy (PMA)

Since this subject will be mentioned recurrently on this thesis, a brief description of the phenomenon is given here.
A FM will always tend to minimize the formation of bound charges on its surface due that it is more energetically favorable. In absence of extrinsic factors, configuration shown in figure 3(a) will be much more stable than the one shown in 3(c), and consequently $\mathbf{m}$ will spontaneously point along the plane of the film.
However, for some types of ultra-thin films made of ferromagnetic materials in contact with non-magnetic metals like Pd and Pt, or insulators like MgO, an interesting interfacial phenomenon appears which favors that $\mathbf{m}$ points perpendicular to plane of

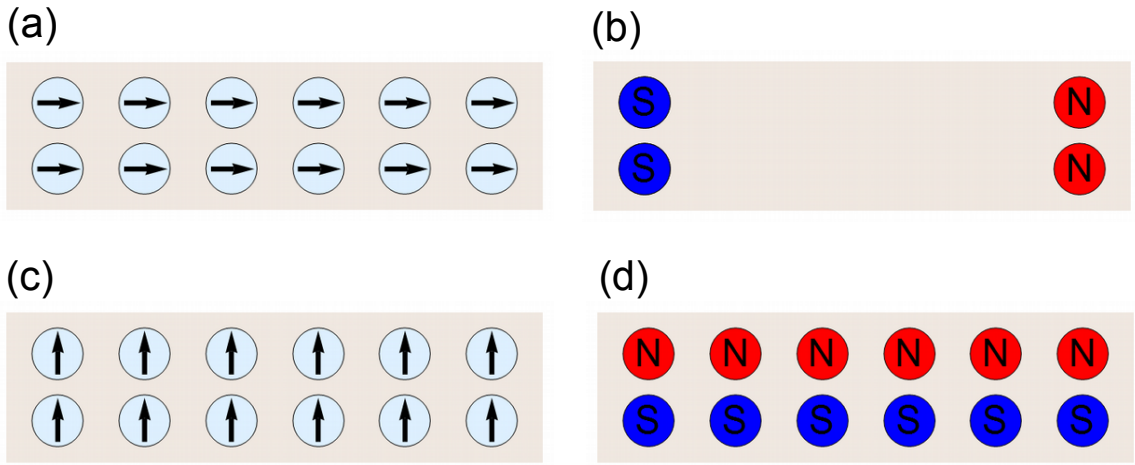

Figure 3: Spontaneous orientation of the magnetization for a thin FM with (a) and without (c) net PMA (c). (b) and (d) depicts the formation of surface bound charges in each case.

the film . This phenomenon is called perpendicular magnetic anisotropy (PMA). In some cases PMA is so strong that **m** will spontaneously point perpendicular to the plane of the film. When this happens we say that the structure has net PMA.

Thin films and nanostructures

The expression **thin film** will be employed when referring to structures whose thickness is nanometric but their lateral dimensions are macroscopic, like the figure 4(a) . Thin films studied in this thesis may be made from single or multiple layers of different materials (represented by different layer colors in Fig. 4(a)).
The term **nanostructure** will be empolyed for structures of both vertical and lateral nanometric dimensions, more specifically nanopillars of elliptical cross section like shown in 4b). These nanopillars are made of two single domain ferromagnetic layers, namely the free and the polarizer layer, separated from a non magnetic material. If the spacer is a metal the device is named Spin Valve (SV) and when the spacer is an insulator is named Magnetic Tunnel Junction (MTJ). The vectors **m** and **p** are the unitary vectors of the magnetization of the free and polarizer layers respectively.
These nanostructures present the giant magnetoresistance (GM) effect in the case of SVs, or tunneling magnetoresistance (TMR) effect in the case of MTJs. This means that their electrical resistance measured across the vertical axis, depends strongly on the relative angle between **m** and **p**. Closely related to this is the presence of the spin transfer torque (STT) effect in these nanostructues. STT effect is the change of the orientation of **m** by spin polarized electric current coming from the polarizer layer. This subject will be addressed in detail in chapter 1.

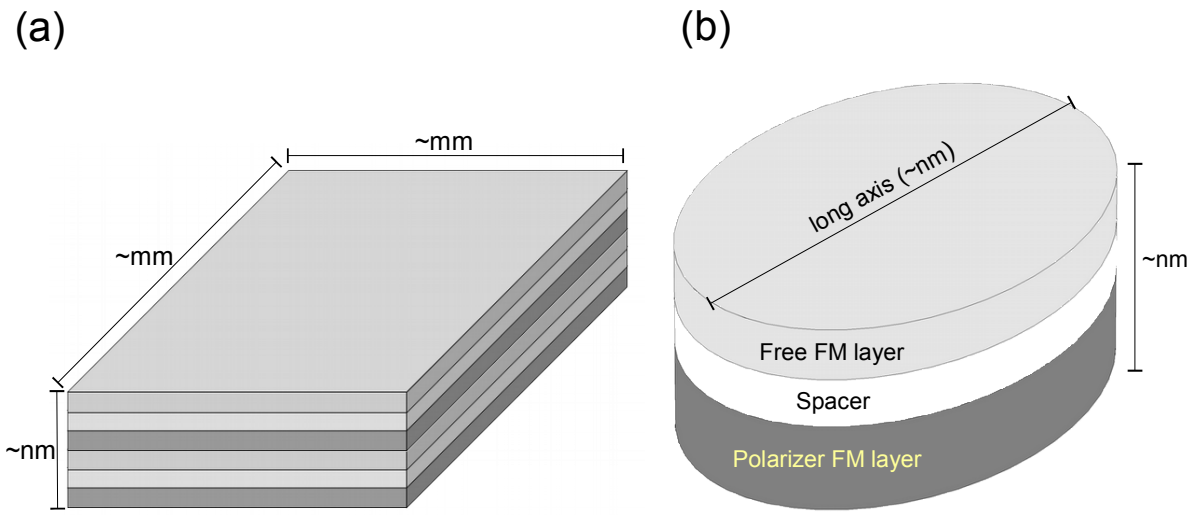

Figure 4: Geometry and dimensions of thin films (a) and nanostructures (b) studied in this thesis.

Thesis outline

The structure of this thesis is outlined on Fig. 5.
The theoretical part of this thesis is exposed in chapters 1 and 2 and deals with the generation and detection of FMR on nanostructures.
Chapter 1 establish a general theoretical framework to find equilibrium states of the magnetization under the presence of spin polarized currents, as well as their stability. These determination of these states is fundamental for the correct application of the theory developed in chapter 2. The layers colors in (a) represent different materials.
Chapter 2 focus on the generation of FMR by spin polarized currents, in addition to a recently discovered effect: the voltage controlled PMA (VCMA). This chapter also addresses the detection of FMR in nanostructures by the spin rectification effect (SRE).
Chapter 3 describes a methodological advance in the broadband FMR spectroscopy technique to improve the accuracy of the determined gyromagnetic factor.
Chapter 4 exposes an application of the broadband FMR spectroscopy with a systematic study of PMA intensity in CoFeB/Pd multilayers.

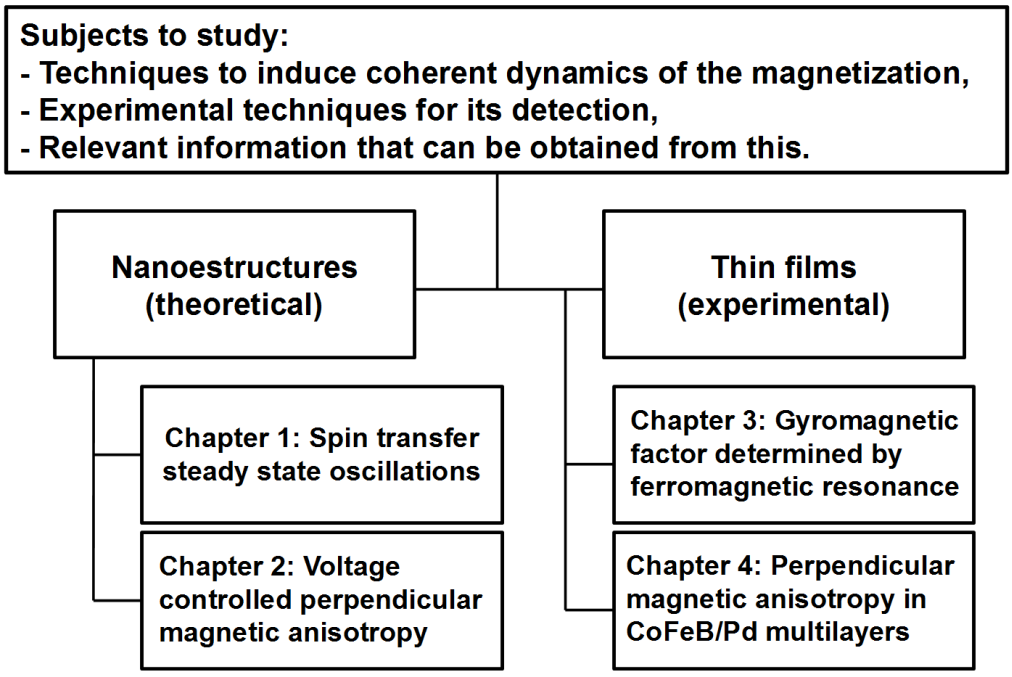

Figure 5: Outline of the thesis

Chapter 1

Spin transfer steady-state oscillators

1.1 Introduction: Spin transfer torque

Let's suppose we have a nanostructure composed by 2 metallic FMs with different magnetization orientations and a metallic non-magnetic spacer between them as shown in Fig. 1.1(a). The Fermi level of each conductor is populated mainly by electrons whose spin points in the same direction of the magnetization. If an electric current starts to flow from bottom to the top layer there will be not only a charge flow but also a transfer of part of the magnetic momentum carried by those electrons, as shown in Fig. 1.1(b). This magnetic moment transfer acts as and extra force in the LLG equation presented in the introduction, and can lead to the cancellation damping force, making possible perpetual oscillations of the free layer magnetization $\mathbf{m}$ around the effective field $\mathbf{H}^{\mathrm{e}}$ (see Fig. 1.2).

1.2 Landau-Liftshitz-Gilbert-Slonczewski equation

The dynamics of $\mathbf{m}$ in a SV or MTJ nanopillar structuretransversed by an electric current is described by the Landau-Liftshitz-Gilbert-Slonczewski (LLGS) equation:

$$\dot{\mathbf{m}} = -\gamma^{*}\mathbf{m} \times \left[\mathbf{H}^{e} - \frac{\alpha}{\gamma^{*}}\dot{\mathbf{m}} - \beta_{\parallel}(\theta)\,\mathbf{m} \times \mathbf{p} - \beta_{\perp}\mathbf{p}\right], \tag{1.1}$$

where $\mathbf{p}$ is the unit vector of the magnetization of the polarizer and θ is the relative angle between $\mathbf{m}$ and $\mathbf{p}$.
Respect to the Eq. 4, Eq. 1.1 includes two extra terms proportional to the electric current. The term

$$\beta_{\parallel}(\theta)\,\mathbf{m} \times \mathbf{p}$$

represents the In-Plane STT (IP-STT), also called the Slonczewski or non-adiabatic STT. This term is not conservative and is the responsible of the anti-damping effect shown in Fig. 1.2. $\beta_{\parallel}(\theta)$ is the IP-STT field magnitude.
On the other side, the term:

$$\beta_{\perp}(\theta)\,\mathbf{p}$$

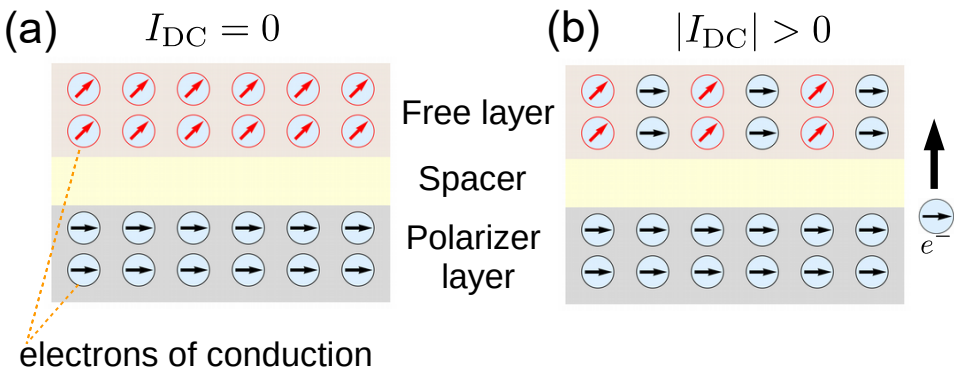

Figure 1.1: Nanostructure with two different orientations of the magetization for the free and fixed layer. In (a) the current is null and in (b) the electric current starts to flow, so the polarizer layer transfers some of its magnetic moment to the free layer.

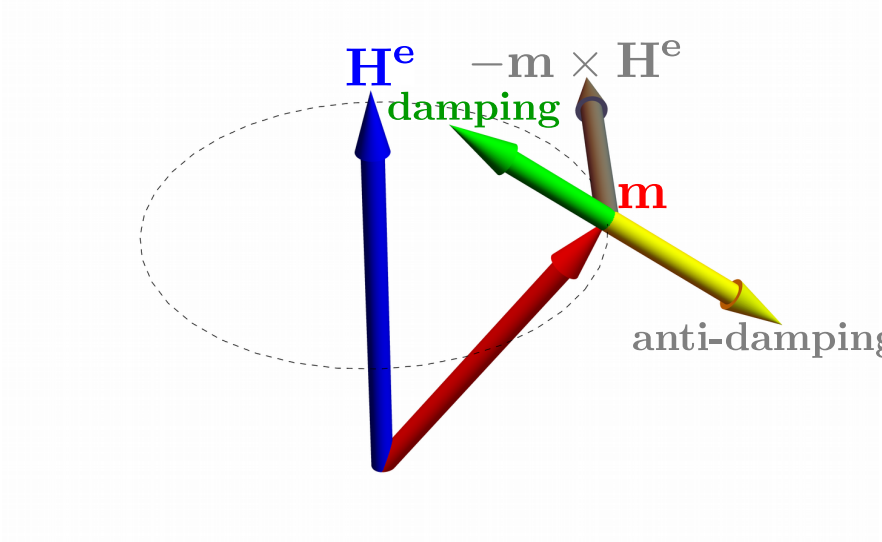

Figure 1.2: Effect of the anti-damping force on the precision of $\mathbf{m}$.

Table 1.1: g dependence on $u = \cos\theta$ for different STT models. $g_1(u)$ is equal to the first derivative of g respect to u . In the ballistic model, $\zeta_{P_f} = 0.25\,(1+P_f)^3\,P_f^{-3/2}$ with P_f the polarizing factor, while in the diffusive model χ is the giant magneto-resistance asymmetry parameter. In MTJs P is the tunneling polarization factor.

Reference	$g(u)$	$g_1(u)$
Ballistic polarization model[3]	$\left(-4+(3+u)\,\zeta_{P_f}\right)^{-1}$	$-\zeta_{P_f} g^2(u)$
Diffusive polarization model[14]	$(P_f(1+\chi))\,(2+\chi(1+u))^{-1}$	$-\chi g^2(u)\,(P_f(1+\chi))^{-1}$
STT in MTJs[15, 16]	$P\,(1+P^2u)^{-1}$	$-Pg^2(u)$

represents the Field-Like STT (FL-STT), also called the out-of-plane or adiabatic STT. This term is conservative and is equivalent to an extra applied magnetic field of magnitude $\beta_\perp(\theta)$.
In general FL-STT is important only in MTJs whereas in SVs is often considered negligible. The most relevant term is the IP-STT. $\beta_\parallel(\theta)$ is given by

$$\beta_\parallel = bg(\theta)$$

with

$$b = \frac{\hbar I_{\mathrm{DC}}}{2\mu_0 q_e M_{\mathrm{s}} V},$$

where $\hbar$ is the reduced plank's constant, q_e is the elementary charge, M_{s} and V are the saturation magnetization and volume of the free layer respectively. I_{DC} is the electric current and is defined positive when the electrons flow from the free to the polarizer layer. $g(\theta)$ is a function that depends on the specific model taken for the STT. A brief summary of the main models that can be found in literature an their respective $g(\theta)$ functions is given in Table 1.1.
In this chapter it is assumed that $\beta_\perp(\theta)$ is proportional to $\beta_\parallel(\theta)$ [13] by a factor ν:

$$\beta_\perp(\theta) = \nu\beta_\parallel(\theta).$$

Then, the LLGS equation can be rewritten in the following form:

$$\dot{\mathbf{m}} = -\gamma^*\mathbf{m}\times\left[\mathbf{H}^{\mathrm{e}} - \frac{\alpha}{\gamma^*}\dot{\mathbf{m}} - \beta_\parallel(\theta)\,(\mathbf{m}\times\mathbf{p}+\nu\mathbf{p})\right] \tag{1.2}$$

It is worth mentioning that up to date, no analytical solutions of $\mathbf{m}(t)$ have been found for the LLGS equation, even in the case of non-angular dependence of $\beta_\parallel(\theta)$.
Nonetheless, it is not necessary to solve directly the LLGS to obtain a full picture of $\mathbf{m}$ dynamics. Instead, the strategy here is to find the set of equilibrium states of $\mathbf{m}$, and the dynamics of the perturbations around them. But first, the next two sections detail the systems of reference employed for the calculations as well as the derivation of $\mathbf{H}^{\mathrm{e}}$.

1.2.1 Systems of Reference

It is convenient to define two systems of reference:

- The standard or experimental system of reference: In this system the **z** axis is perpendicular to the film's plane and the **x** axis points along the easy axis of the nanostructure, as shown in Fig. 1.3.
- The moving system of reference. In this system the **Z** points in the same direction than **m** and the **X** lies on the film's plane, as shown in Fig. 1.4. The cartesian axes in this system of reference will be denoted capital letters $(\mathbf{X}, \mathbf{Y}, \mathbf{Z})$ in order to avoid confusions.

The standard system of reference is more easily seen in the experimental configuration and is better to find the equilibrium states of **m.** On the other hand, the moving system of reference is more convenient for the analysis of the dynamics.

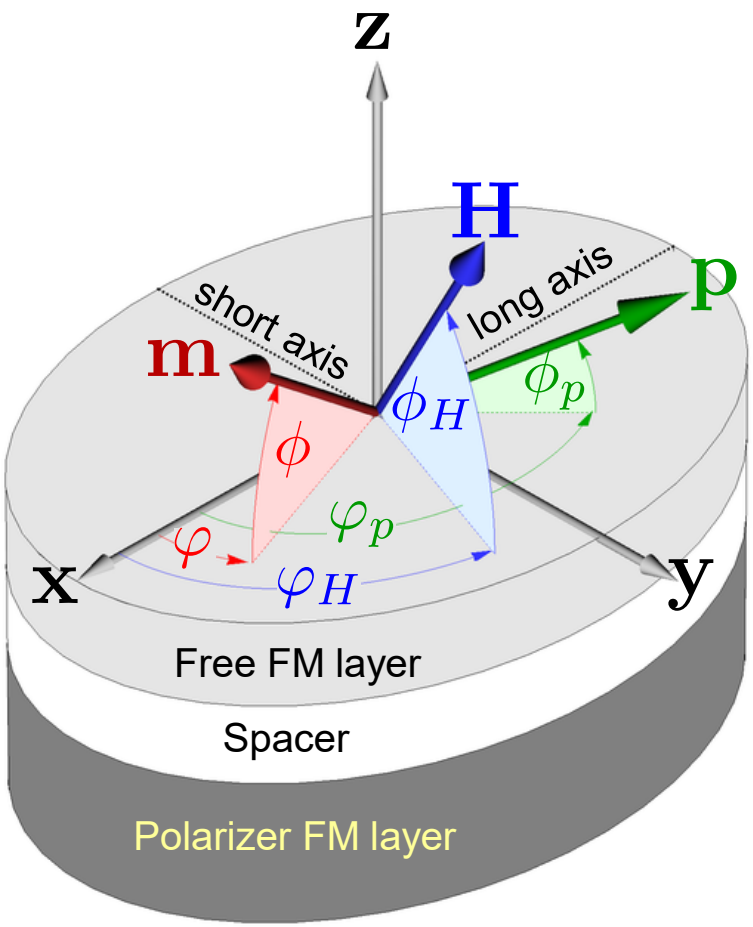

Figure 1.3: Geometry of the nanopillar and the cartesian axes of the standard system of reference considered in the theory.

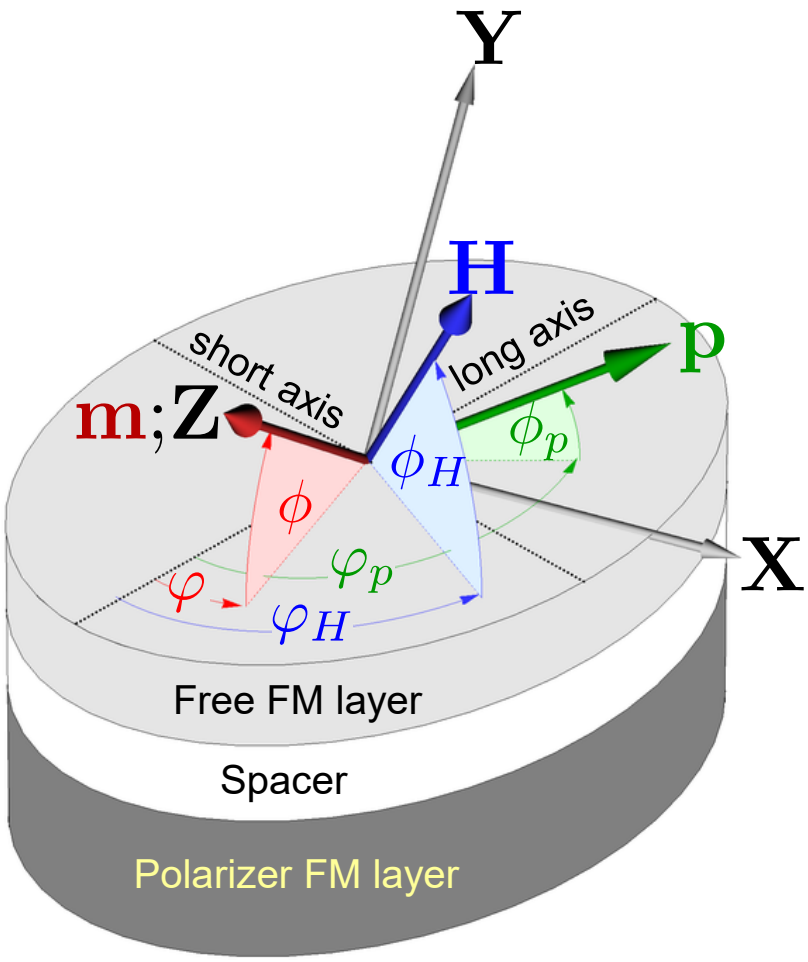

Figure 1.4: Geometry of the moving system of reference considered in the theory.

From Fig. 1.3, the components of **m**, **p** and the applied magnetic field **H** in the standard system of reference are:

$$\begin{aligned}
m_x &= \cos(\phi)\cos(\varphi), \\
m_y &= \cos(\phi)\sin(\varphi), \\
m_z &= \sin(\phi), \\
H_x &= H\cos(\phi_H)\cos(\varphi_H), \\
H_y &= H\cos(\phi_H)\sin(\varphi_H), \\
H_z &= H\sin(\phi_H), \\
p_x &= \cos(\phi_p)\cos(\varphi_p), \\
p_y &= \cos(\phi_p)\sin(\varphi_p), \\
p_z &= \sin(\phi_p).
\end{aligned} \tag{1.3}$$

The components of **H** and **p** in the moving system of reference are obtained by applying successively the rotation matrices respect to **z** and **x** axis: $\mathbf{R}_z[-\pi/2-\varphi]$,

$\mathbf{R}_x\left[-\pi/2+\phi\right]$ on (m_x, m_y, m_z), where the rotation matrices are:

$$\mathbf{R}_x\left[\Omega\right] = \begin{pmatrix} 1 & 0 & 0 \\ 0 & \cos\Omega & -\sin\Omega \\ 0 & \sin\Omega & \cos\Omega \end{pmatrix}; \mathbf{R}_z = \begin{pmatrix} \cos\Omega & -\sin\Omega & 0 \\ \sin\Omega & \cos\Omega & 0 \\ 0 & 0 & 1 \end{pmatrix}.$$

Therefore:

$$\begin{aligned} m_X &= m_Y = 0, \\ m_Z &= 1, \\ H_X &= -H\left(\cos\phi_H \sin\left(\varphi-\varphi_H\right)\right), \\ H_Y &= -H\left(\cos\phi_H \cos\left(\varphi-\varphi_H\right)\sin\phi + \cos\phi\sin\phi_H\right), \\ H_Z &= H\left(\cos\phi\cos\phi_H\cos\left(\varphi-\varphi_H\right) + \sin\phi\sin\phi_H\right), \\ p_X &= -\cos\phi_p \sin\left(\varphi-\varphi_p\right), \\ p_Y &= -\cos\phi_p\cos\left(\varphi-\varphi_p\right)\sin\phi + \cos\phi\sin\phi_p, \\ p_Z &= \cos\phi\cos\phi_p\cos\left(\varphi-\varphi_p\right) + \sin\phi\sin\phi_p = \cos\theta. \end{aligned} \tag{1.4}$$

1.2.2 Effective field

The effective field $\mathbf{H}^{\mathrm{e}}$ accounts for the conservative fields interacting with $\mathbf{m}$ [1]. $\mathbf{H}^{\mathrm{e}}$ is equal to the derivative of the total magnetic energyper unit of volume ε , respect to the magnetization:

$$\mathbf{H}^{\mathrm{e}} = -\frac{1}{\mu_0 M_{\mathrm{s}}}\frac{\delta\varepsilon}{\delta\mathbf{m}},$$

where ε is the sum of the energies arising from the mechanisms listed below:

Zeeman energy

The Zeeman energy arises from the interaction of a magnetized body with the external magnetic field $\mathbf{H}$:

$$\varepsilon_H = -\mu_0 M_{\mathrm{s}}\left(H_x m_x + H_y m_y + H_z m_z\right) \tag{1.5}$$

Magnetostatic Energy

This term is generated by the bound magnetic charges that appear on the surface of a FM. For bodies of ellipsoidal shape, the energy may be put in terms of the demagnetizing factors N_x, N_y, and N_z:

$$\varepsilon_M = \frac{\mu_0 M_{\mathrm{s}}^2}{2}\left(N_x m_x^2 + N_y m_y^2 + N_z m_z^2\right), \tag{1.6}$$

where M_{s} is the saturation magnetization and μ_0 is the vacuum permeability. $\mathbf{D}$ is the demagnetizing tensor:

$$\mathbf{D} = \begin{pmatrix} N_x & 0 & 0 \\ 0 & N_y & 0 \\ 0 & 0 & N_z \end{pmatrix}. \tag{1.7}$$

[1] In fact the FL-STT is also conservative, however, is convenient to put all the current-dependent terms apart from $\mathbf{H}^{\mathrm{e}}$

Thin films may be approximated by an ellipsoid of infinite lateral dimensions, in that case $N_x = N_y = 0$ and $N_z = 1$. In the case of an elliptical cylinder like the free layer of the nanostructure shown in Fig. 1.3, the demagnetizing factors have been obtained explicitly in the work of Beleggia et al. [17].
By convention, the standard system of reference is chosen to have $\pm\mathbf{x}$ as the in-plane spontaneous magnetization axis also called easy axis. Therefore N_x will always be smaller than N_y and N_z and will be along the long axis of the body.

Magnetocrystalline Anisotropy

These terms may arise from the symmetries of the crystalline grid of a FM. In this work 2 types of magnetocrystalline anisotropies are considered:

- **In plane uniaxial magnetic anisotropy (IPA)** IPA promotes **m** along the $\pm\mathbf{x}$ axis. The corresponding energy term is:

$$\varepsilon_u = -\frac{1}{2}\mu_0 M_\mathrm{s} H_u m_x^2 \tag{1.8}$$

  where H_u is the magnitude of the IPA field. Notice that this term is analogous to the N_x term in Eq. 1.6, so the effect of IPA without shape anisotropy, can be obtained by making the change:

$$N_x \to -\frac{H_u}{M_\mathrm{s}},$$

  and set $N_y = 0$, $N_z = 1$. In this work the results are presented in terms of the demagnetizing factors. If the reader wants to apply the results to a thin film or nanostructure with IPA, the above mentioned transformations must to be carried out.

- **Perpendicular magnetic anisotropy (PMA)** PMA promotes **m** along the $\pm\mathbf{z}$ axis. The corresponding energy term is:

$$\varepsilon_s = -\frac{1}{2}\mu_0 M_\mathrm{s} H_s m_z^2. \tag{1.9}$$

  where H_s is the magnitude of the PMA field. In thin films, this term will compete against the demagnetizing field and may eventually overcome it, making the magnetization to point spontaneously out of plane, in such case we say that the films has **net PMA**. A more detailed discussion about the origin and examples of perpendicular magnetic anisotropy will be given in chapter 4.

Total energy density

Now we have and the complete set of energy terms and thus we can get the effective field:

$$\begin{aligned}\mathbf{H}^\mathrm{e} &= -\frac{\delta}{\delta \mathbf{m}}\left(\varepsilon_H + \varepsilon_M + \varepsilon_u + \varepsilon_s\right) = \\ &\mathbf{H} - M_\mathrm{s} N_x m_x \widehat{\mathbf{x}} - M_\mathrm{s} N_y \widehat{\mathbf{y}} + M_\mathrm{eff} m_z \widehat{\mathbf{z}}\end{aligned} \tag{1.10}$$

were:

$$M_{\text{eff}} = H_s - M_{\text{s}} N_z$$

M_{eff} stands for the effective magnetization. If $M_{\text{eff}} < 0$ the FM has net PMA.

1.2.3 Stationary solutions of the LLGS equation

Since at this point all the terms of Eq. 1.1 have been derived as well as the systems of reference, now the calculation of the equilibrium states of the LLGS equation in the standard system of reference is carried out. To start with, the $\beta_{\parallel}$ dependence on θ is neglected, and $\dot{\mathbf{m}}$ is taken as null:

$$\mathbf{0} = -\gamma^* \mathbf{m} \times \left(\mathbf{H}^{\text{e}} - \beta_{\parallel} \left(\mathbf{m} \times \mathbf{p} + \nu \mathbf{p} \right) \right). \tag{1.11}$$

To satisfy the above equation the quantity inside the parenthesis has to be parallel to $\mathbf{m}$:

$$\mathbf{H}^{\text{e}} - \beta_{\parallel} \left(\mathbf{m} \times \mathbf{p} + \nu \mathbf{p} \right) = \lambda \mathbf{m}, \tag{1.12}$$

where λ is a still undetermined constant. The terms of $\mathbf{H}^{\text{e}}$ that are linear on the components of $\mathbf{m}$ are grouped in the left side:

$$\mathbf{L} \cdot \mathbf{m} = -\mathbf{H} + \nu \beta_{\parallel} \mathbf{p}, \tag{1.13}$$

where $\mathbf{L}$ is the matrix:

$$\mathbf{L} = \begin{pmatrix} -M_{\text{s}} N_x - \lambda & -p_z \beta_{\parallel} & p_y \beta_{\parallel} \\ p_z \beta_{\parallel} & -M_{\text{s}} N_y - \lambda & -p_x \beta_{\parallel} \\ -p_y \beta_{\parallel} & p_x \beta_{\parallel} & -M_{\text{eff}} - \lambda \end{pmatrix}.$$

The set of equations implicit in Eq. 1.11 can be solved readily with the Crammer's rule:

$$m_x = \frac{\det \mathbf{L}_1}{\det \mathbf{L}}; \; m_y = \frac{\det \mathbf{L}_2}{\det \mathbf{L}}; \; m_z = \frac{\det \mathbf{L}_3}{\det \mathbf{L}}, \tag{1.14}$$

where $\mathbf{L}_j$ is the result of replacing the j-column of the matrix $\mathbf{L}$ by the vector $-\mathbf{H} + \nu \beta_{\parallel} \mathbf{p}$. Then by applying the normalization condition:

$$m_x^2 + m_y^2 + m_z^2 = 1, \tag{1.15}$$

it is obtained a polynomial equation of degree 6 (or sextic equation) in λ with up to six real solutions. In summary, the vectorial Eq. 1.11 was transformed into a polynomial equation of one variable: λ. According to the Abel-Ruffini theorem [18], the sextic equation can not be, in general, solved algebraically , and hence analytic solutions are not always available. Therefore, Eq. 1.15 was solved numerically using the internal Wolfram Mathematica software root-finding algorithms. Once the set of real solutions for λ are obtained, each one is replaced in the set of Eqs. 1.14 to obtain the corresponding set of equilibrium states of $\mathbf{m}$.

Adding θ dependence

Finally, to obtain a even better estimation of the solutions of Eq. 1.11, the dependence on θ is included. This is done by an iterative method: once the set of equilibrium for $\mathbf{m}$ have been obtained by the above described method, new values of $\beta_{\|}$ are calculated and process is repeated again with this new values. This iterative process is stopped when the difference between the successive values of $\beta_{\|}$ is less than $10^{-4}\%$. A set of many starting values of θ are taken in each calculation, chosen randomly between 0 and 2π.

1.2.4 Dynamical behavior of equilibrium solutions

Once the set of equilibrium orientations of the magnetization $\mathbf{m}_i^{\mathrm{eq}}$ have been obtained, the stability of each one is determined by analyzing the dynamics of perturbations on them. To start with, Eq. (1.1) is put in terms of perturbative magnetization unit vector $\mathbf{m}^{\mathrm{p}}$, perturbative effective field $\mathbf{H}^{\mathrm{ep}}$ and perturbative IP-STT field $\beta_{\|}^{\mathrm{p}}$:

$$\dot{\mathbf{m}}^{\mathrm{p}} = -\gamma^* \mathbf{m}^{\mathrm{p}} \times \left[\mathbf{H}^{\mathrm{ep}} - \frac{\alpha}{\gamma^*} \dot{\mathbf{m}}^{\mathrm{p}} - \beta_{\|}^{\mathrm{p}} \left(\mathbf{m}^{\mathrm{p}} \times \mathbf{p} + \nu \mathbf{p} \right) \right], \tag{1.16}$$

were:

$$\mathbf{m}^{\mathrm{p}} = m_X \widehat{\mathbf{Y}} + m_Y \widehat{\mathbf{Y}} + \left(1 - m_X^2 - m_Y^2 \right) \widehat{\mathbf{Z}}. \tag{1.17}$$

$m_{X,Y}$ accounts for the small time-dependent deviations of $\mathbf{m}^{\mathrm{p}}$ respect to the equilibrium orientation.$\beta_{\|}^{\mathrm{p}}$ is obtained expanding up to first order in m_X and m_Y :

$$\beta_{\|}^{\mathrm{p}}(\theta) \approx b \left[g(p_Z) + g_1(p_Z) \left(m_X p_X + m_Y p_Y \right) \right] \tag{1.18}$$

were g and g_1 are specified in table (1.1). Notice that $p_Z = \cos\theta$, where θ is the relative angle between $\mathbf{p}$ and $\mathbf{m}$.
$\mathbf{H}^{\mathrm{ep}}$ is obtained by first getting the components of $\mathbf{m}^{\mathrm{p}}$ in the standard system of reference ($m_{x,y,z}^{\mathrm{p}}$) as function of the ones from the moving system of reference ($m_{X,Y}$). The later was carried out by applying successively the rotation matrices $\mathbf{R}_x[\pi/2 - \phi]$ and $\mathbf{R}_z[\pi/2 + \varphi]$ on the vector (m_X,m_Y, 1):

$$\begin{aligned} m_x^{\mathrm{p}} &= \cos(\varphi)(\cos\phi - m_Y \sin\phi) - m_X \sin\phi, \\ m_y^{\mathrm{p}} &= m_X \cos\varphi + (\cos\phi - m_Y \sin\phi)\sin\varphi, \\ m_z^{\mathrm{p}} &= m_Y \cos(\phi) + \sin\phi. \end{aligned} \tag{1.19}$$

Then, $\mathbf{H}^{\mathrm{e}}$ from Eq. 1.10 is put in terms of $m_{X,Y}$ using the set of Eqs. 1.19, to finally apply the successive rotation matrices $\mathbf{R}_z[-\pi/2 - \varphi]$, $\mathbf{R}_x[-\pi/2 + \phi]$ on it:

$$\mathbf{H}^{\mathrm{ep}} = \mathbf{R}_x \left[-\frac{\pi}{2} + \phi \right] \cdot \mathbf{R}_z \left[-\frac{\pi}{2} - \varphi \right] \cdot \mathbf{H}^{\mathrm{e}} \tag{1.20}$$

explicitly:

$$
\begin{aligned}
H_x^{\mathrm{ep}} &= \left(M_{\mathrm{s}} N_x m_x^{\mathrm{p}} - H\cos\phi_H\cos\varphi_H\right)\sin\varphi + \cos\varphi\left(-M_{\mathrm{s}} N_y m_y^{\mathrm{p}} + H\cos\phi_H\sin\varphi_H\right), \\
H_y^{\mathrm{ep}} &= \sin\phi\left[\cos\varphi\left(M_{\mathrm{s}} N_x m_x^{\mathrm{p}} - H\cos\phi_H\cos\varphi_H\right) + \sin\varphi\left(\mu_0 M_{\mathrm{s}} N_y m_y^{\mathrm{p}} - H\cos\phi_H\sin\varphi_H\right)\right] + \\
&\quad \cos\phi\left(-M_{\mathrm{eff}} m_z^{\mathrm{p}} + H\sin\phi_H\right), \\
H_z^{\mathrm{ep}} &= \cos\phi\left[H\cos\varphi\cos\phi_H\cos\varphi_H - M_{\mathrm{s}}\left(N_x m_x^{\mathrm{p}}\cos\varphi + N_y m_y^{\mathrm{p}}\sin\varphi\right) + H\cos\phi_H\sin\varphi\sin\varphi_H\right] \\
&\quad + \sin\phi\left(-M_{\mathrm{eff}} m_z^{\mathrm{p}} + H\sin\phi_H\right). \qquad (1.21)
\end{aligned}
$$

Finally inserting Eqs. 1.21, 1.18 and 1.17 into 1.16 and solving for $\dot{m}_{X,Y}$, the following set of equations is obtained:

$$
\begin{aligned}
\dot{m}_X &= A_{11} m_X + A_{12} m_Y. \\
\dot{m}_Y &= A_{21} m_X + A_{22} m_Y, \qquad (1.22)
\end{aligned}
$$

where:

$$
\begin{aligned}
A_{11} &= \gamma^*\left[-H_{XY} - \alpha H_{XX} + \right. \\
&\qquad \left. bI_{\mathrm{DC}}\left(p_Z g\left(p_Z\right)\left(1+\alpha\nu\right) - p_X g_1\left(p_Z\right)\left(p_X\left(1+\alpha\nu\right) + p_Y\left(\nu-\alpha\right)\right)\right)\right], \\
A_{12} &= \gamma^*\left[-H_{YY} - \alpha H_{XY} - \right. \\
&\qquad \left. bI_{\mathrm{DC}}\left(p_Z g\left(p_Z\right)\left(\alpha-\nu\right) + p_Y g_1\left(p_Z\right)\left(p_X\left(1+\alpha\nu\right) + p_Y\left(\nu-\alpha\right)\right)\right)\right], \\
A_{21} &= \gamma^*\left[H_{XX} - \alpha H_{XY} - \right. \\
&\qquad \left. bI_{\mathrm{DC}}\left(p_Z g\left(p_Z\right)\left(\nu-\alpha\right) + p_X g_1\left(p_Z\right)\left(p_Y\left(1+\alpha\nu\right) + p_X\left(\alpha-\nu\right)\right)\right)\right], \\
A_{22} &= \gamma^*\left[H_{XY} - \alpha H_{YY} + \right. \\
&\qquad \left. bI_{\mathrm{DC}}\left(-p_Z g\left(p_Z\right)\left(1+\alpha\nu\right) - p_Y g_1\left(p_Z\right)\left(p_Y\left(1+\alpha\nu\right) + p_X\left(\alpha-\nu\right)\right)\right)\right], \qquad (1.23)
\end{aligned}
$$

with:

$$
\begin{aligned}
H_{XX} &= H_Z - M_{\mathrm{eff}}\sin^2\phi + \\
&\qquad M_{\mathrm{s}}\left[N_y + \left(N_x - N_y\right)\sin^2\varphi - \cos^2\phi\left(N_x\cos^2\varphi + N_y\sin^2\varphi\right)\right], \\
H_{XY} &= H_{YX} = M_{\mathrm{s}}\left(N_x - N_y\right)\sin\phi\sin\left(2\varphi\right), \\
H_{YY} &= H_Z + \cos\left(2\phi\right) M_{\mathrm{eff}} - \frac{M_{\mathrm{s}}\cos\left(2\phi\right)}{2}\left[N_x + N_y + \left(N_x - N_y\right)\cos\left(2\varphi\right)\right]. \qquad (1.24)
\end{aligned}
$$

Terms of order higher than one in $m_{X,Y}$ have been neglected as well as terms proportional to α^2. The set of Eqs. 1.22 may be written in the matrixial form:

$$\dot{\mathbf{m}} = \mathbf{A}\cdot\mathbf{m}$$

The eigenvalues of $\mathbf{A}$ evaluated at each $\mathbf{m}_i^{\mathrm{eq}}$ determine whether the equilibrium point is stable or not: if the real part of both eigenvalues is negative, $\mathbf{m}_i^{eq}$ will be stable, in any other case will be unstable. The two eigenvalues of $\mathbf{A}$ can be obtained straightforwardly:

$$\lambda_{\pm} = \frac{1}{2}\left(A_{11} + A_{22} \pm \sqrt{\left(A_{11} - A_{22}\right)^2 + 4A_{12}A_{21}}\right) \qquad (1.25)$$

Apart from the stability, the real and imaginary parts of $\lambda_\pm$ give out qualitative description of the trajectory described by $\mathbf{m}$ when approaching to (distancing from) stable (unstable) equilibrium points in the unitary sphere that represents the domain of $\mathbf{m}$, as is shown in Fig. 1.5. There are two groups of cases:

- $(A_{11} - A_{22})^2 + 4A_{12}A_{21} > 0$: λ_+ and λ_- have null imaginary and different real part. The trajectory described by $\mathbf{m}$ is in quite direct. Those points are denoted as "nodes", as shown in Fig. 1.5(a)

- $(A_{11} - A_{22})^2 + 4A_{12}A_{21} < 0$: λ_+ and λ_- have not null imaginary part and the same real part is given by:

$$\mathrm{Re}[\lambda_\pm] = \frac{1}{2}(A_{11} + A_{22}). \tag{1.26}$$

  Also, the magnitude of the imaginary part of the two eigenvalues is the same and given by:

$$|\mathrm{Im}[\lambda_\pm]| = \frac{1}{2}\sqrt{(A_{11} - A_{22})^2 + 4A_{12}A_{21}}.$$

  The trajectory described by $\mathbf{m}$ in the unitary sphere is in spiral, as shown in Fig. 1.5(b). In this case, $|\mathrm{Im}[\lambda_\pm]|$ corresponds to the angular velocity of the spiral. Notice that FMR can be considered as the case in which $\mathbf{m}$ follows a spiral trajectory towards a stable equilibrium point, however, a source of energy prevents $\mathbf{m}$ from reach it, making him to orbit perpetually that point. Therefore, one can infer that $|\mathrm{Im}[\lambda_\pm]|$ evaluated at $\alpha = I_{\mathrm{DC}} = 0$ (i.e. excluding damping and anti-damping mechanisms), is the natural frequency of oscillation ω_N. As in other physical systems ω_N is very close, but not equal, to the resonance frequency ω_R. The exact value of ω_R will be obtained in chapter 2.

1.3 Application: self-oscillations in magnetic tunnel junctions

In order to illustrate the theory exposed above, we have studied the magnetization dynamics of a typical spintronics device: a MTJ under the action of a spin polarized current and no external magnetic field. The absence of the magnetic field is interesting since is more desirable condition to real application devices[19].
In this type of MTJs is common that the free and polarizer layer are of CoFeB alloy whereas the spacer is MgO. The following parameters for the MTJ free layer are taken: $M_\mathrm{s} = 1.1 \times 10^6$A/m, $\alpha = 0.01$, $\mu_0 H_u = 0.01$ T, $P = 0.57$, $\nu = -0.1$, thickness $d = 1.6$ nm and a junction area $A = \pi \times 150\mathrm{nm} \times 70\mathrm{nm}$. These values were taken from an elliptical cross-section MTJ studied in reference [19], with exception of H_s wich was modified in order to better expose the results: $\mu_0 H_s = 1.58$ T. Therefore the free layer has a small but significant net PMA: $\mu_0 M_{\mathrm{eff}}$=-0.2 T. The demagnetizing factors were set to equal to the ones from an infinite thin film: $N_x = N_y = 0$; $N_z = 1$. Nonetheless, notice that the shape anisotropy have been included by the finite value of the in-plane anisotropy field H_u

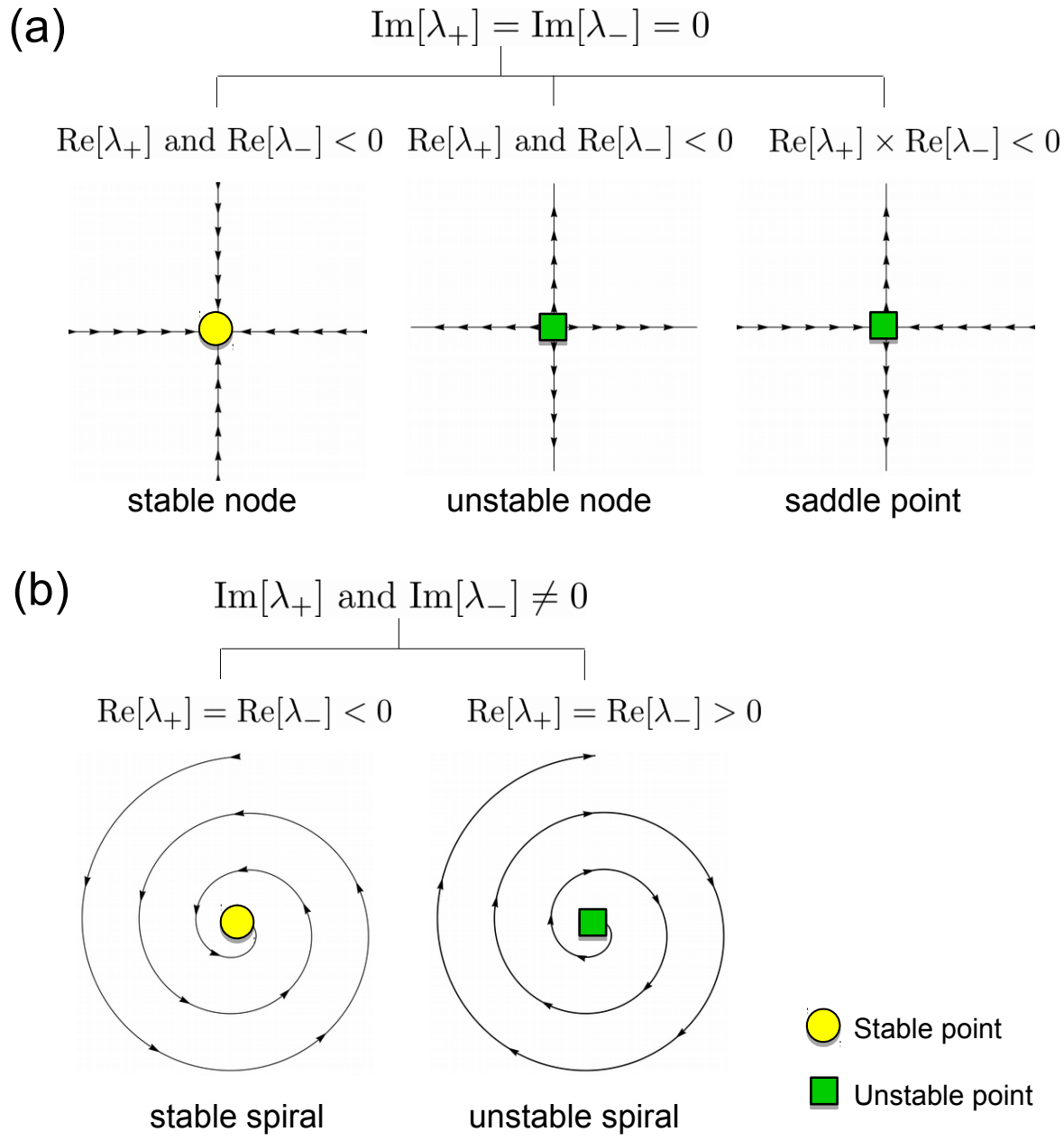

Figure 1.5: Qualitative sketch of the possible trajectories of $\mathbf{m}$ close to an equilibrium point in the unitary sphere, and their dependence on the complex eigenvalues of $\mathbf{A}$ matrix .

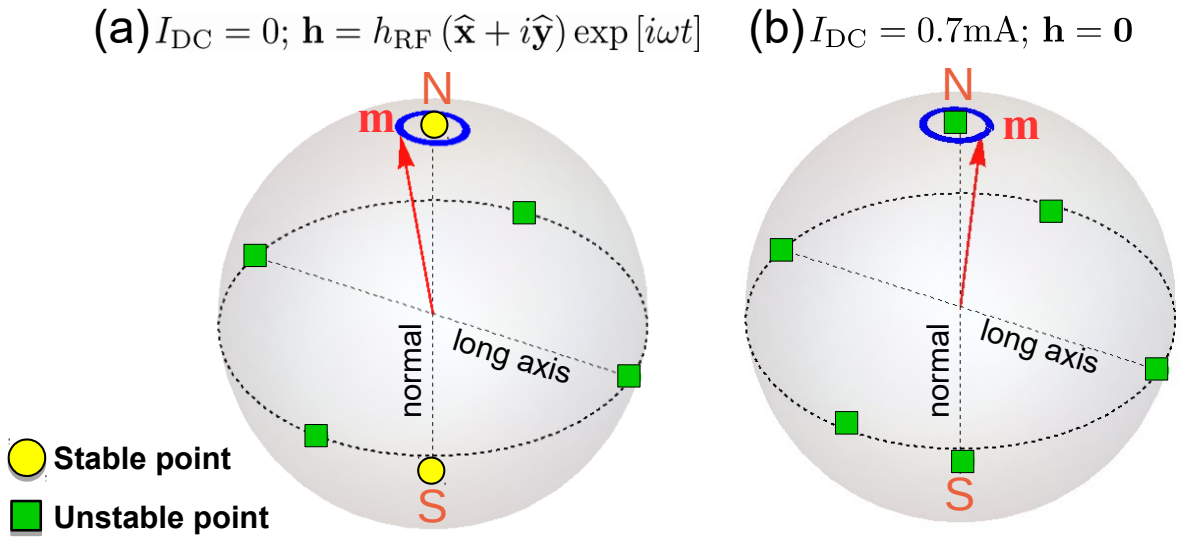

Figure 1.6: Simulations of $\mathbf{m}$ trajectory (blue) at the proximity of the N equilibrium point of the unitary sphere, for a MTJ nanostructure under zero applied field. In (a) the oscillations are around the stable N point and are induced by an oscillating magnetic field: $h_{RF} = 0.25$ mT; $\omega = 5.6$ GHz, where ω was set at the natural frequency of oscillation. In (b) steady state oscillations appear spontaneously around the unstable N point. The starting point of $\mathbf{m}$ in both cases is set at $\phi = 81°$; $\varphi = 0°$.

Emergence of steady self-oscillations

In the zero current case, there are six possible equilibrium states $\mathbf{m}_i^{eq}$, as shown in Fig. 1.6 plotted as points on a unitary sphere. Among them, only the two ones out of the plane are stable, namely the N and S points. Therefore, independently of the initial orientation of $\mathbf{m}$, it will end up at one of those two stable points. One can check from Eqs.1.23 and 1.24 that $(A_{11} - A_{22})^2 + 4A_{12}A_{21}$ evaluated at both N or S points is negative, so the real part of both λ_+ and λ_- will be given by the expression 1.26 which corresponds to the case shown Fig. 1.5(b). Since $A_{11} + A_{22} < 0$, the stability of N and S points is confirmed.
If $\mathbf{p}$ is kept at ϕ_p=0° and I_{DC} is increased, the equilibrium points S and N do not change their position in the unitary sphere. However $A_{11} + A_{22}$, increases with I_{DC}, passing from negative values at $I_{DC} = 0$ to positive values at certain critical value I_{DC}^c. For $I > I_{DC}^c$ there will not longer be stable equilibrium points on the unitary sphere, since the other 4 equilibrium points maintain their unstability.
One may think that in this case the orbit of $\mathbf{m}$ on unitary sphere turns chaotic, however, chaos is precluded in dynamic systems with two degrees of freedom by the Poincare-Bendixson theorem [20]. What really happens is that the orbit of $\mathbf{m}$ end up in a steady state oscillations (SSO) regime around one of the unstable points of the unitary sphere, as shown in Fig. 1.6(b).
The value of I_{DC}^c can be derived from Eq. 1.26 by solving:

$$A_{11} + A_{22} = 0.$$

After some algebra:

$$I_{DC}^{c} = \frac{2\alpha q_e M_s V}{(1+\alpha\nu)\hbar|g_1(0)|}\left(|\mu_0 M_{\text{eff}}| - \frac{H_u}{2}\right). \tag{1.27}$$

To better visualize the results, numerical simulations of **m** trajectory on the unitary sphere are shown in Fig. 1.6. The value of I_{DC} was set at 0.7 mA (slightly above $I_{\text{DC}}^{c} = 0.63$ mA). In the simulations **m** initially approaches the N point, and then starts to orbit perpetually around it (see Fig. 1.6(b)). Notice that the SSO regime is completely analogous to conventional FMR: the same simulation was carried out with $I_{\text{DC}} = 0$ and including a oscillating perturbative extra magnetic field. The result is shown in Fig. 1.6(a): **m** describes an orbit around the stable N point.
A main outcome of this work is the demonstration of the impossibility to generate SSO with zero external magnetic field with g_1 null i.e without angular dependence of IP-STT. This can be concluded from 1.27: if $\beta_{\parallel}$ were not dependent on θ, g_1 would be zero and hence I_{DC}^{c} diverges. This conclusion have been also presented in the references [21] and [22]. In those works the existence of SSOs at zero external field was attributed to a special "wavy angular dependence" of STT. In contrast, this work it has demonstrated that is a general consequence for of any type of $\beta_{\parallel}$ dependence on θ.
Experimentally SSOs can be detected through the oscillatory changes on the magnetoresistance on SVs or MTJs ,this subject will be treated in more detail in chapter2. The technological importance of the SSOs comes from the fact that is a new way to produce microwave oscillating electric signals from a non-oscillatory source: the DC current.

1.3.1 Stability phase diagrams

The results shown in the precedent sections were illustrative examples for fixed values of **p** and I_{DC}. A very general picture of the dynamics of the system can be seen in the stability phase diagram (Fig. 1.7(a)) in which ϕ_p and the current density J vary continuously from 0 to 15 and 0 to $2{\times}10^{11}$A/m. The phase stability diagram identifies the cases where two states are stable (lighter color in zone I and III), only one state is stable (intermediate color in zones II, V and VI) and all states are unstable (darker color in zone IV). In zone I, the orientations of **m** toward N and S are stable and therefore the magnetization can end up in any of them depending on its initial condition. In zone II only the orientation towards S (or N) is stable if $\phi_p > 0$ ($\phi_p < 0$). In zone III, again two stable equatorial states appear, where one of them lies in the plane (G_1 for $\phi_p > 0$ and G_2 for $\phi_p < 0$) and the other one is located in S (N) for $\phi_p > 0$ ($\phi_p < 0$). For the area VI, only the orientation towards S (N) is stable if $\phi_p > 0$ ($\phi_p < 0$), since the point G_1 (G_2) is not an equilibrium state anymore. In zone V only the in-plane state remains stable (point G_1 or G_2), while in zone IV all states are unstable and hence OSSs are expected [20]. Besides, notice that there is a small asymmetry in the phase diagram regarding the change in sign of ϕ_p, which is originated by the FL-STT.
It's worth mentioning that OSSs can exist outside of zone IV as well, namely the coexistence of both a stable equilibrium and OSSs. Nevertheless, OSSs inside the zone IV are independent of the initial condition $\mathbf{m}(t = 0)$, whereas that the coexisting of

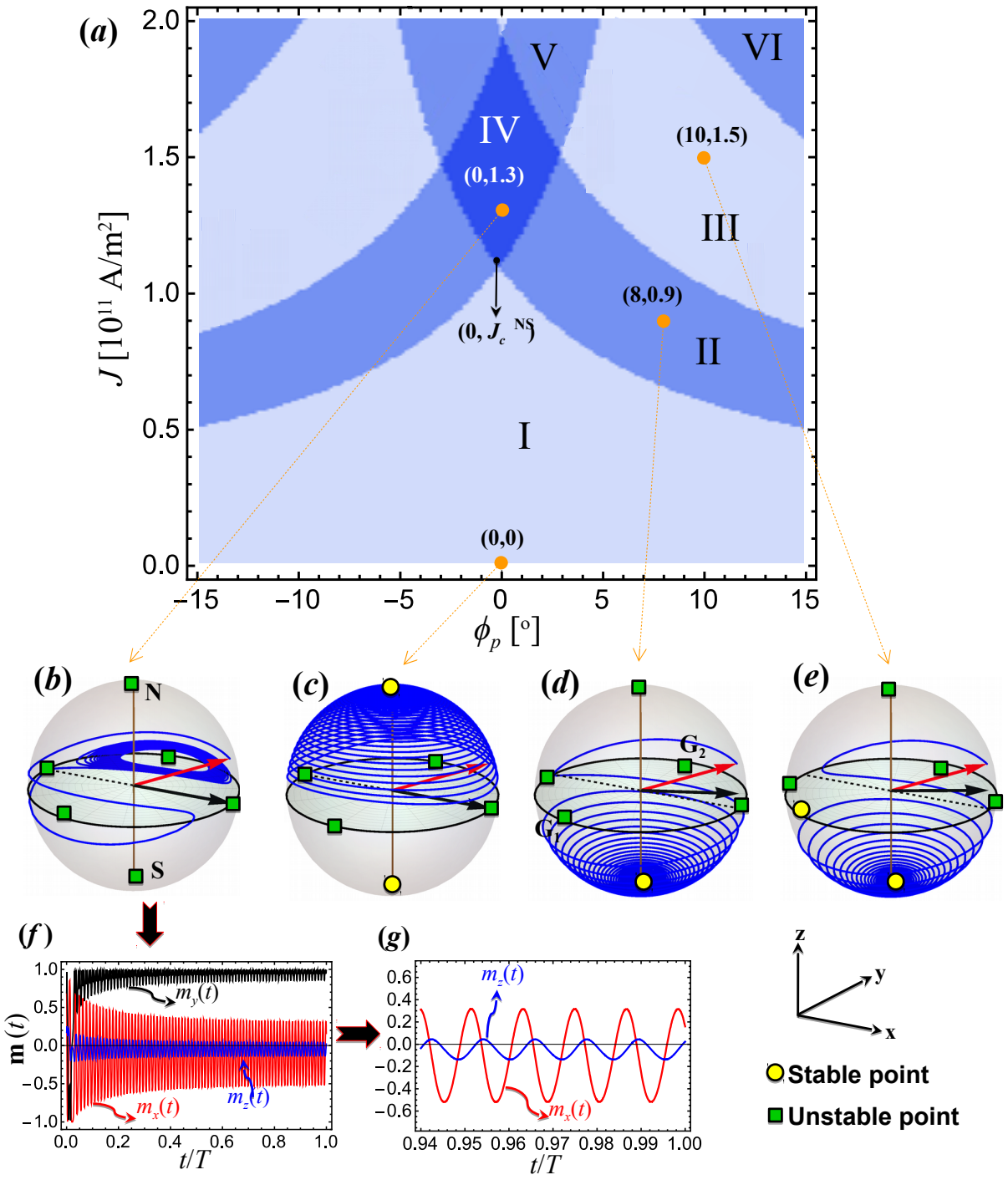

Figure 1.7: Phase stability diagram. The color identifies the following cases: two states are stable (lighter color in zone I and III), only one state is stable (intermediate color in zones II, V, and VI), and all states are unstable (darker color in zone IV). (b)-(e) represent magnetization orbits solved for some points (ϕ_p, J) of zones I-IV. The point $\left(0, J^{NS}\right)$ shows local destabilization of both N and S. (f) and (g) depict **m** components as a function of t/T, with T=328 ns.

OSSs with a stable equilibrium point depends on the initial condition, since whether $\mathbf{m}(t=0)$ is close to stable equilibrium point $\mathbf{m}$ will reach such state.
To corroborate the analytical results, the LLGS equation has been solved numerically, as illustrated in Figs. 1.7(b)–(g), where the orbits of $\mathbf{m}$ are shown. The initial condition of $\mathbf{m}$ (red lighter arrow) is arbitrarily chosen as $\phi(t=0) = 10°$ and $\varphi(t=0) = 45°$. The equilibrium states are shown by means of yellow circles and green squares for stable and unstable states, respectively. In Fig. 1.7(b) all states are unstable, hence the magnetization reaches the OSSs regime. $\mathbf{m}$ components are plotted in Figs. 1.7(f)–(g) in order to see clearly the oscillating steady-states. In zone V, the magnetization reaches the point G_1 and OSSs states are not feasible (not shown). Overall, analytical results are in very good agreement with the numerical ones. It has been shown that at $p_Z = 0$ a destabilization of all equilibrium states is feasible and its range is limited by simultaneous stabilization of in-plane points G_1 and G_2 (and also by simultaneous stabilization of N and S). Furthermore, when $p_Z \neq 0$ the OSSs zone increases up to reach the point where both the stabilization of N and G_2 (or S and G_1) occurs simultaneously and again the broadening of IV is limited.

1.4 Summary

I have developed a model that allows to find the equilibrium states an of the magnetization of the free layer in nanostructures type spin valve or magnetic tunnel junction, subjected to spin polarized currents, as well as the stability of those states . The advantage of the model developed in this work, with respect to previous ones, is its completeness and generality: all the fixed points and their stabilities are found for any value of the experimental parameters. This information let us to build very comprehensive phase diagrams like the example of the Fig. 1.7. Much of the previous works have consider only certain orientations of the polarizer or take into account only two of the fixed points [22–24]
Moreover, in our work the angular dependence of $\beta_\parallel$ is included. This contrast with other works in which similar phase diagrams were calculated [23]. Although this may not have significant effect in the position of the fixed points, has enormous influence on their stability and should never be excluded. A summary of the main outcomes of the work presented in this chapter have been published in reference [25], in collaboration with Rodolfo Gallardo and Pedro Landeros.

Chapter 2

Voltage controlled perpendicular magnetic anisotropy

2.1 Introduction

In chapter 1 it was shown how spin polarized currents can be employed to manipulate the magnetization on single domain FMs. Despite the important advances in this subject, there is still a problem to overcome: the high current density needed to manipulate the magnetization. A promising alternative to solve this issue is to use voltages instead of currents to manipulate the magnetization. During the last years it has been demonstrated theoretically [26–28] and experimentally [29] that is possible to modify the magnitude and of the interfacial PMA between a ferromagnetic metal and an oxide by the application of a electric field across the structure. A qualitative description of this phenomenon is shown in Figure 2.1: let's suppose that we have a MTJ structure like the one depicted on Figure 2.1 with significant PMA. Under 0 applied voltage, the equilibrium magnetization is pointing in some angle ϕ_p between the film's plane and the normal. If we then apply a voltage across the MTJ, there will be charge accumulation on the interface between the free layer and the insulator. This charge accumulation will modify the occupation of the Fermi levels at interface, and consequently the interfacial electronic states that give origin to the PMA. The magnitude of the PMA is thus modified and ϕ_p increases or decreases depending on the sign of the voltage. This effect has been called Voltage Controlled Magnetic Anisotropy (VCMA). The work of Wang et al.[30] demonstrated that the effect may be strong enough to switch the magnetization of the ferromagnet by the application of a voltage. Ndo et al. [31] verified the VCMA effect in the $Co_{40}Fe_{40}B_{20}$/MgO junctions. This is interesting since this combination of materials have also been widely employed on STT devices. Therefore, provided that the lateral dimensions of a MTJ nanopillar are nanometric, the application of a voltage would produce simultaneously both VCMA and STT effects. Regarding this, it is worth to note that if we apply an oscillating voltage across a MTJ like the one shown on Figure 2.1, it would induce FMR through the VCMA, STT or both effects, in the same way of any other oscillating parameter in the LLGS equation would do.
In this respect the theoretical-experimental work of Zhu et al. [13] was the first in demonstrating the coexistence of VCMA and STT in electrically induced FMR at MTJ.

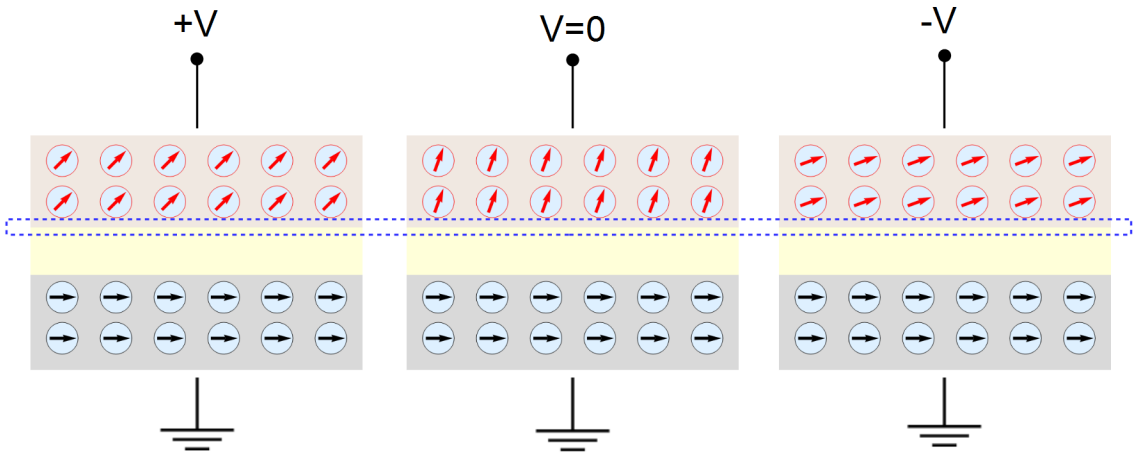

Figure 2.1: Voltage Controlled Magnetic Anisotropy (VCMA) in a magnetic tunnel junction (MTJ): the charges accumulated at the interface between the free layer and the insulator (blue dashed rectangle) modify the interfacial electronic states, resulting in a change of the perpendicular magnetic anisotropy (PMA).

However their theoretical results were done only with simulations and consequently have a lack of generality.
This work has been motivated in great measure by the above mentioned work of Zhu et al. [13], and is aimed to fulfill such lack of generality by developing a comprehensive and analytical model to distinguish and quantify VCMA and STT effects through FMR experiments in MTJ nanopillars. To start with, we have to explain how FMR is detected in nanostructures by means of the Spin rectification effect.

2.2 Spin Rectification Effect

The microwave currents driving the magnetization dynamics in SVs or a MTJs can couple with the same magnetization dynamics that the are generating leading to the appearance of a DC voltage across the device, this effect, known as the spin rectification effect (SRE), enables the FMR to be electrically detected in structures much smaller than available by conventional detection. The SRE was first observed by Tulapurkar et al.[32] and since then has been extensively used to study the magnetization dynamics in nanostructures.
A conceptual depiction of the SRE is shown in figure 2.2. The precession of **m** gives rise to periodic changes in the TMR from low (2.2(a)) to high resistance states (2.2(a)). Now, let's suppose that the microwave current is negative in the first half of the cycle and positive in the second half. The time average of the voltage will be different from zero, because for equal magnitude of the microwave current , the resistance in the first half of the cycle is lower than in the second one. This voltage will be proportional to the amplitude of the oscillations of **m** and hence will be maximum at the resonance frequency.
In the following section we will theoretically derive the lineshape of the FMR spectrum

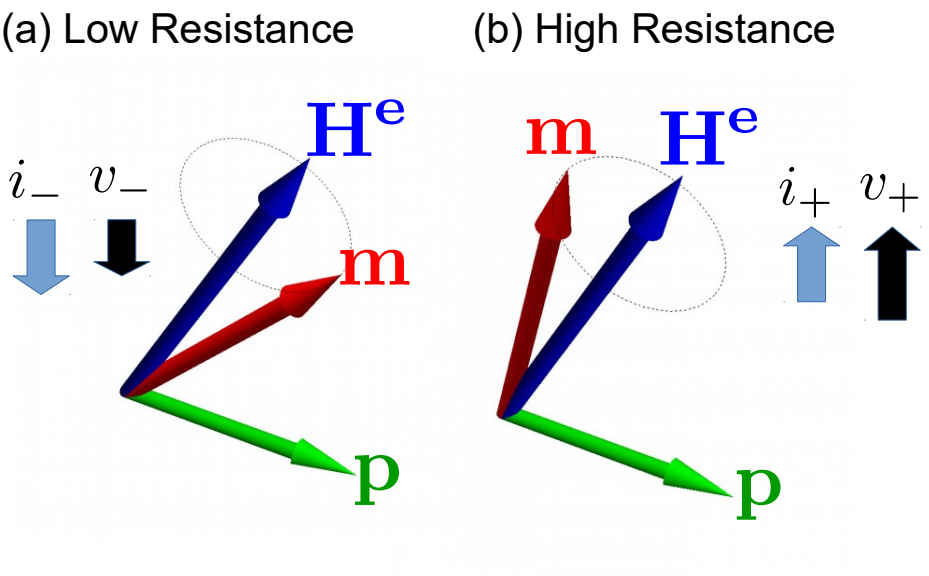

Figure 2.2: Spin Rectification Effect (SRE): during the first half of the oscillation cycle (a), the electric current is negative, and positive during the second half (b). Although the time average of the electric current is zero, the voltage is not: in the first part of the cycle the resistance is lower due to the $\mathbf{m} \cdot \mathbf{p}$ dependence of the tunnel magnetoresistance. The time average of the voltage reflects the amplitude of $\mathbf{m}$ oscillations

around the resonance frequency and show how this can be used to the quantification of the magnitude of the spin torque vector and the recently discovered VCMA effect.

2.3 Rectified DC voltage across a MTJ

The typical experimental setup [33–35] to detect FMR electrically is depicted in figure 2.3. A microwave current $I_{RF}(t)$ and a DC current I_{DC} are injected simultaneously into the sample through a bias tee. The temporal average of voltage $\langle V \rangle$ across the sample can be detected with a nanovoltmeter or alternatively by a lock-in amplifier in order to improve the signal-to-noise ratio. In the later case the microwave generator must modulate the microwave current to a low frequency (hundreds of Hz), which is taken as reference by the lock-in amplifier. $\langle V \rangle$, will depend on the total current $I(t)$ flowing through the MTJ and its electrical resistance $R[t]$, which in turn depends directly on relative angle $\theta(t)$ between $\mathbf{m}$ and $\mathbf{p}$. It is assumed that $I(t) = I_{DC} + I_{RF}(t)$ and $\theta(t) = \theta_0 + \delta\theta(t)$, where $I_{RF}(t)$ and $\delta\theta(t)$ are the time-dependent perturbations on I_{DC} and θ_0: the equilibrium values of those quantities.
A good approximation of $\langle V \rangle$ is obtained expanding it up to second order:

$$\begin{aligned}\langle V \rangle &= \Bigg\langle V(I_{DC}, \theta_0) + \frac{\partial V}{\partial \theta}\Big|_{\theta_0} \delta\theta(t) + \frac{\partial V}{\partial I}\Big|_{I_{DC}} I_{RF}(t) + \frac{1}{2}\frac{\partial^2 V}{\partial I^2}\Big|_{I_{DC}} I_{RF}(t)^2 + \\ &\quad \frac{\partial^2 V}{\partial I \partial \theta}\Big|_{I_{DC},\theta_0} I_{RF}(t)\,\delta\theta(t) + \frac{1}{2}\frac{\partial^2 V}{\partial \theta^2}\Big|_{\theta_0} \delta\theta(t)^2 \Bigg\rangle \end{aligned} \tag{2.1}$$

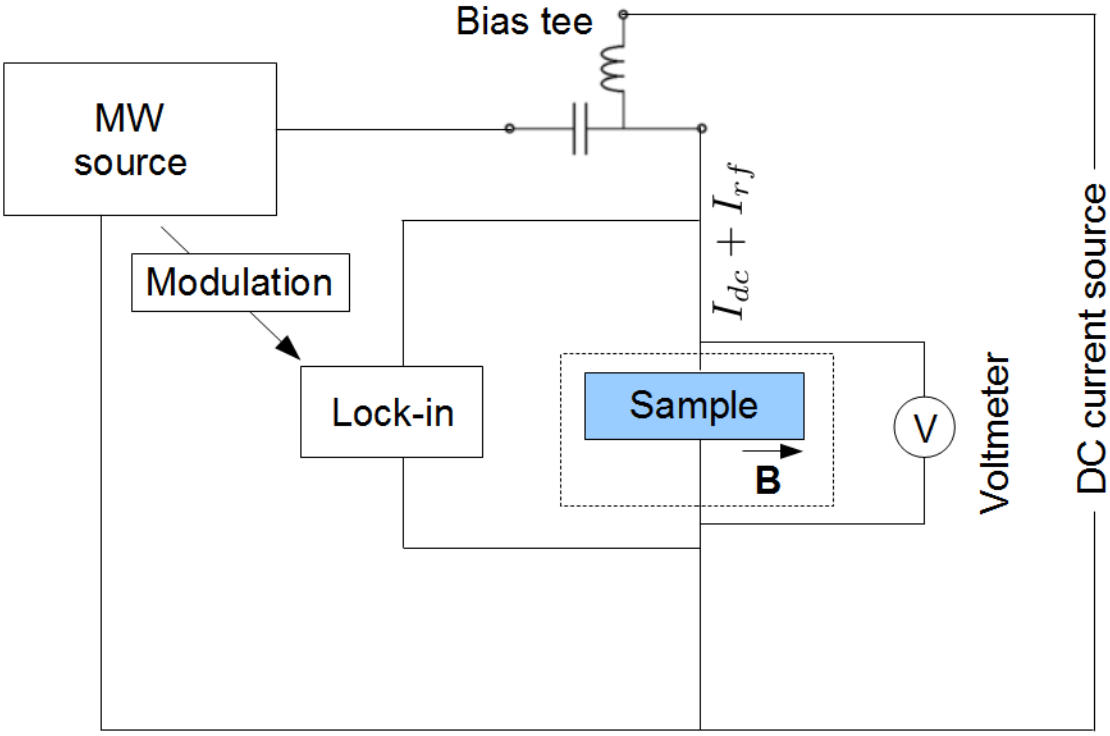

Figure 2.3: Experimental set-up of electrically detected FMR

The relevant part is only on the time average of the perturbative part of the voltage, namely the rectified voltage δV. Then, the equilibrium component $V(I_{DC}, \theta_0)$ will be disregarded in the following. Moreover, since $\delta\theta(t)$ and $I_{RF}(t)$ have a periodic time dependence, both second and third terms averages zero. Then:

$$\delta V = \frac{1}{2}\frac{\partial^2 V}{\partial I^2}\Big|_{I_{DC}} \langle I_{RF}(t)^2 \rangle + \frac{\partial^2 V}{\partial I \partial \theta}\Big|_{I_{DC},\theta_0} \langle I_{RF}(t)\,\delta\theta(t) \rangle + \frac{1}{2}\frac{\partial^2 V}{\partial \theta^2}\Big|_{\theta_0} \langle \delta\theta(t)^2 \rangle \qquad (2.2)$$

The first term arises from the non-linearity of the I-V curve and gives rise to non-resonant background in δV [36]. Second and third terms are the most relevant: they are proportional to the amplitude of the precession of $\mathbf{m}$ and hence are key to detect the FMR. In the following, it will be assumed that the non-resonant background has been conveniently subtracted in the analysis of the experimental data.
The following expression for the voltage is considered:

$$V = R(I, \theta)\, I$$

where R is the tunnel magnetoresistance. Recalculating 2.2:

$$\delta V = \left(\left(\frac{\partial^2 R}{\partial\theta \partial I}\Big|_{I_{DC},\theta_0} \right) I_{DC} + \frac{\partial R}{\partial \theta}\Big|_{\theta_0} \right) \langle I_{RF}(t)\,\delta\theta(t) \rangle + \frac{1}{2} I_{DC} \left(\frac{\partial^2 R}{\partial \theta^2}\Big|_{\theta_0} \right) \langle \delta\theta(t)^2 \rangle$$

The term proportional to I_{DC} within the first term of δV, is expected to be small respect to the second one [37] and hence is neglected. This is as a consequence of the relatively weak dependence of $R(I,\theta)$ on I.
Respect to the last term of δV, although may be important in anisotropic magnetoresistance experiments [38], it has been argued that is not relevant in the SRE unless $I_{\mathrm{DC}} \gg I_{\mathrm{RF}}$ [36]. A further demonstration of the latter assumption, is the fact that in reported SRE experiments δV does not follow a linear relationship with I_{DC}. Finally:

$$\delta V = \left(\frac{\partial R}{\partial \theta}\Big|_{\theta_0} \right) \langle I_{RF}(t)\, \delta\theta(t) \rangle \tag{2.3}$$

For the TMR, the Slonczewsky [39] expression is assumed:

$$R = \frac{R_0}{1 + P^2 \cos\theta}. \tag{2.4}$$

Where P is the polarization factor, and R_0 is the electrical resistance at $\theta = \pi/2$. Also $I_{RF}(t) = I^0_{RF} \cos(\omega t)$ with I^0_{RF} and ω are the amplitude and frequency of the microwave current, respectively. Then:

$$\delta V = \frac{R_0 P^2 \sin\theta_0 I^0_{RF}}{(1 + P^2 \cos\theta_0)^2} \langle \cos(\omega t)\, \delta\theta(t) \rangle . \tag{2.5}$$

Since $\delta\theta(t)$ is a perturbation, it can be put in terms of the components of the perturbed $\mathbf{m}$ in the moving system of reference: $\mathbf{m}^p$, already employed in the stability analysis of the chapter 1. Expanding $\delta\theta(t)$ up to first order:

$$\theta(t) = \arccos(\mathbf{m}^p \cdot \mathbf{p}) = \arccos(m_X(t)\, p_X + m_Y(t)\, p_Y + \cos\theta_0) \tag{2.6}$$

$$\approx \theta_0 - \frac{m_X(t)\, p_X + m_Y(t)\, p_Y}{\sin\theta_0}, \tag{2.7}$$

then:

$$\delta\theta(t) = -\frac{m_X(t)\, p_X + m_Y(t)\, p_Y}{\sin\theta_0} \tag{2.8}$$

Replacing in 2.5 :

$$\delta V = \frac{R_0 P^2 I^0_{RF}}{(1 + P^2 \cos\theta_0)^2} \langle -\cos(\omega t)\, (m_X(t)\, p_X + m_Y(t)\, p_Y) \rangle$$

At this point is convenient to define a new function to distinguish the ω-dependent part of δV from the scaling prefactor. This function corresponds to the double of the time average inside the angle brackets, is adimensional, and defines the "lineshape" of the FMR response:

$$L_S(\omega) = \langle -2\cos(\omega t)\, (m_X(t)\, p_X + m_Y(t)\, p_Y) \rangle .$$

Replacing this in Eq. 2.5:

$$\delta V = \frac{R_0 P^2 \sin\theta_0 I^0_{RF}}{2(1 + P^2 \cos\theta_0)^2} L_S(\omega)$$

The following subsection is about the derivation of $m_{X,Y}(t)$ in order to get $L_S(\omega)$.

2.3.1 Obtaining $\mathbf{m}(t)$

We look for stationary solutions for the perturbations $m_{X,Y}(t)$ in the magnetization using the LLGS equation as the starting point:

$$\dot{\mathbf{m}} = -\gamma^* \mathbf{m} \times \left[\mathbf{H}^e - \frac{\alpha}{\gamma^*} \dot{\mathbf{m}} - \beta_{\parallel} \mathbf{m} \times \mathbf{p} - \beta_{\perp} \mathbf{p} \right] \tag{2.9}$$

In chapter 1 the magnitude of FL-STT was assumed proportional to the IP-STT by a constant: $\beta_{\perp} = \nu \beta_{\parallel}$. Notice that the objective in that case was to build phase-diagrams assuming a specific model for the STT vector. In this chapter the scenario is different: we want to provide a model to get $\beta_{\parallel}$ and $\beta_{\perp}$ directly from the experiment, so it is not assumed a priori any particular relationship between them.
For the clarity of the results presented in this chapter, it is convenient put LLGS in terms of the spin torque efficiency. The STT efficiency for each component is defined by:

$$\begin{aligned} \beta'_{\parallel} &= \frac{d\beta}{dI} \\ \beta'_{\perp} &= \frac{d\beta}{dI} \end{aligned}$$

So, the LLGS equation is rewritten:

$$\dot{\mathbf{m}} = -\gamma^* \mathbf{m} \times \left[\mathbf{H}^e - \frac{\alpha}{\gamma^*} \dot{\mathbf{m}} - I(t) \left(\beta'_{\parallel} \mathbf{m} \times \mathbf{p} + \beta'_{\perp} \mathbf{p} \right) \right] \tag{2.10}$$

The following replacements should be made:

$$\mathbf{m} = m_X(t) \widehat{\mathbf{X}} + m_Y(t) \widehat{\mathbf{Y}} + \widehat{\mathbf{Z}}$$

$$I(t) \rightarrow I_{DC} + I^0_{RF} \cos(\omega t) \tag{2.11}$$

The oscillating current injected into the MTJ, simultaneously excites both VCMA and STT dynamically. The effect on the STT is simply to vary the magnitudes of $\beta_{\parallel}$ and $\beta_{\perp}$ periodically. The case of the VCMA effect is somewhat different, since is proportional to the voltage instead of the current. The voltage that is generating the microwave current has the same frequency ω, but in principle, not the same phase because of the capacitive component of the MTJ. This voltage will make a periodic modulation of the PMA field:

$$H_s(t) = H^0_s - \frac{dH_s}{dV} \left(V_{DC} + V^0_{RF} \cos(\omega t + \Delta) \right) \tag{2.12}$$

Where H^0_s is the magnitude of the unperturbed PMA field, V_{DC} and V^0_{RF} are the DC component and the amplitude of the microwave voltage respectively. dH_s/dV is the efficiency of the VCMA effect. Respect to its sign, it has been found that $H_{\perp}$ increases when the free FM layer is charged positively [13, 34], so dH_s/dV is positive in the the above expression. Moreover, in the work of Zhu et al. [13, 34], it was found that dH_s/dV is pretty constant over the full range of voltages employed. Δ is the phase shift between the microwave current and voltage across the MTJ. A circuit analysis must be done in order to get Δ. The current flow through the MTJ can be treated like the

leakage current of a two paralel plates capacitor [40] . Therefore, the complex impedance to this current is the same as in a parallel RC circuit:

$$Z = \frac{R}{1 + i\omega RC}$$

Where C is the capacitance. Considering that the typical MTJs have lateral dimensions are tens of nm and spacer thickness is less than 2 nm, therefore, their capacitance can be approximated as the corresponding to an infinite parallel plates capacitor: $C = A\varepsilon/d$. Since $A \sim 10^{-14}$ m , $d \sim 10^{-9}$m and ε for MgO is around ten times the vacuum permittvity [41] ($\varepsilon_0 = 8.85 \times 10^{-12}$ Fm^{-1}), it comes out that C falls in the sub 10^{-15}F range. The product ωRC then results to be a few mΩ, which is five orders of magnitude below typical $R[\theta]$ values. Therefore, it is safe to assume that $Z = R[\theta]$ and that the microwave current and voltage are in phase i.e. $\Delta = 0$. Rewriting equation in terms of current:

$$H_s = H_s^0 - \beta'_V \left(I_{DC} + I_{RF}^0 \exp\left(i\omega t\right)\right) \tag{2.13}$$

where:

$$\beta'_V = \frac{dH_s}{dI} = \frac{1}{R}\frac{dH_s}{dV}$$

β'_V is the current efficiency of the VCMA effect and has the same units than $\beta'_\parallel$ and $\beta'_\perp$. Turning back to the specification of the components of equation 2.10, notice that he inclusion of the VCMA results in a change of the perturbed effective field respect to the given in equation 1.10, so the following replacement is made:

$$\mathbf{H}^e \rightarrow \mathbf{H}^e - \beta'_V \left(I_{DC} + I_{RF}^0 \exp\left(i\omega t\right)\right) m_Z \widehat{\mathbf{z}}.$$

The above is written for the standard system of reference. The corresponding replacement in the moving system of reference is:

$$\mathbf{H}^e \rightarrow \mathbf{H}^e - \beta'_V \left(I_{DC} + I_{RF} \cos\left(\omega t\right)\right) \left(m_Y\left(t\right) \cos\phi + \sin\phi\right) \left(\cos\phi \widehat{\mathbf{Y}} + \sin\phi \widehat{\mathbf{Z}}\right), \tag{2.14}$$

where the transformation was carried out following the procedures exposed in chapter 2. At this point, all the terms of equation 2.10 have been specified. The stationary solutions of $m_{X,Y}\left(t\right)$ are obtained assuming they will end up oscillating at the same frequency ω of the microwave current:

$$\begin{aligned} m_X\left(t\right) &= m_X^0 \exp\left(i\omega t\right), \\ my\left(t\right) &= m_Y^0 \exp\left(i\omega t\right) \end{aligned} \tag{2.15}$$

where $m_{X,Y}^0$ are complex quantities whose imaginary part reflects the phase difference between the magnetization dynamics and the microwave current.
After making the replacements indicated in equations 2.11, 2.14 and 2.15 in 2.10 and linearizing, taking $m_{X,Y}^0$ and I_{RF}^0 as perturbations, the following set of equations are obtained:

$$\left(J_{11} - i\omega\right) m_X^0 + \left(J_{12} - i\alpha\omega\right) m_Y^0 = T_X \tag{2.16}$$

$$\left(J_{21} + i\alpha\omega\right) m_X^0 + \left(J_{22} - i\omega\right) m_Y^0 = T_Y \tag{2.17}$$

where α^2 has been taken as 0, and

$$\begin{aligned}
J_{11} &= -\gamma^* \left(H_{XY} - I_{DC}\beta'_{\parallel}\cos\theta_0\right) \\
J_{12} &= -\gamma^* \left(H_{YY} + I_{DC}\left(\beta'_{\perp}\cos\theta_0 - \beta'_V\cos\left(2\phi\right)\right)\right) \\
J_{21} &= \gamma^* \left(H_{XX} - I_{DC}\left(\beta'_{\perp}\cos\theta_0 + \beta'_V\sin^2\phi\right)\right) \\
J_{22} &= \gamma^* \left(H_{XY} + I_{DC}\beta'_{\parallel}\cos\theta_0\right) \\
T_X &= \gamma^* I^0_{RF}\left[\beta'_{\parallel}p_X + \beta'_{\perp}p_Y - \frac{\beta'_V}{2}\sin\left(2\phi\right)\right] \\
T_Y &= \gamma^* I^0_{RF}\left(\beta'_{\perp}p_X - \beta'_{\parallel}p_Y\right)
\end{aligned} \tag{2.18}$$

The values of, H_{XX}, H_{XY} and H_{ZZ}, as well as the components of the vector $\mathbf{p}$ in the moving system of reference, were already given in chapter 1 and were not modified here. Notice that the terms T_X and T_Y, are both proportional to I^0_{RF} ,thus reflecting the excitation input into the system.
It is worth noting that the terms derived from the angular dependence of the STT, i.e. the terms proportional to g_1, are not present in equations 2.18 . Although it was demonstrated in chapter 1 that those terms are fundamental for the correct analysis of the stability of fixed points, they are not relevant for the results of this chapter and have been omitted. This was carefully verified by also carrying out all the upcoming calculations but also including the terms proportional to g_1: the results presented only second order corrections respect to the presented here.
The equation (2.11) can be put in terms of a matrixial equation for the components of $\mathbf{m}^0_{\perp}$:

$$\mathbf{J}' \cdot \mathbf{m}^0_{\perp} = \mathbf{T}_{\perp}, \tag{2.19}$$

with

$$\mathbf{J}' = \begin{pmatrix} J_{11} - i\omega & J_{12} - i\alpha\omega \\ J_{21} + i\alpha\omega & J_{22} - i\omega \end{pmatrix}, \tag{2.20}$$

$$\mathbf{m}^0_{\perp} = \begin{pmatrix} m^0_X \\ m^0_Y \end{pmatrix}, \tag{2.21}$$

$$\mathbf{T}_{\perp} = \begin{pmatrix} T_X \\ T_Y \end{pmatrix}. \tag{2.22}$$

The system of Equations (2.19) can be solved directly using Cramer's rule:

$$\begin{pmatrix} m^0_X \\ m^0_Y \end{pmatrix} = \frac{1}{-\det\mathbf{J}'} \times \begin{pmatrix} -J_{22}T_X + J_{12}T_Y + i\left(T_X - T_Y\alpha\right)\omega \\ J_{21}T_X - J_{11}T_Y + i\left(T_X\alpha + T_Y\right)\omega \end{pmatrix} \tag{2.23}$$

where $\det\mathbf{J}'$ is

$$-\det\mathbf{J}' = \omega^2 - \omega_R^2 - i\lambda\omega,$$

and

$$\begin{aligned}
\omega_R^2 &= J_{11}J_{22} - J_{12}J_{21}, \\
\lambda &= -\left(J_{11} + J_{22} + \left(J_{12} - J_{21}\right)\alpha\right), \\
S_X &= -T_X + T_Y\alpha, \\
A_X^S &= -J_{22}T_X + J_{12}T_Y, \\
S_Y &= -T_X\alpha - T_Y, \\
A_Y^S &= J_{21}T_X - J_{11}T_Y.
\end{aligned}$$

The time dependence of $m_X(t)$ and $m_Y(t)$ then will be:

$$\begin{pmatrix} m_X(t) \\ m_Y(t) \end{pmatrix} = \Re\left[\frac{\exp(i\omega t)}{\omega^2 - \omega_R^2 - i\lambda\omega}\begin{pmatrix} A_X^S - iS_X\omega \\ A_Y^S - iS_Y\omega \end{pmatrix}\right] \tag{2.24}$$

or more explicitly:

$$\begin{aligned}
\begin{pmatrix} m_X(t) \\ m_Y(t) \end{pmatrix} = \frac{1}{\left(\omega^2 - \omega_R^2\right)^2 + \lambda^2\omega^2} \times \Bigg[&\cos(\omega t)\begin{pmatrix} A_X^S\left(\omega^2 - \omega_R^2\right) + \lambda\omega^2 S_X \\ A_Y^S\left(\omega^2 - \omega_R^2\right) + \lambda\omega^2 S_Y \end{pmatrix} + \\
&\sin(\omega t)\begin{pmatrix} \lambda\omega A_X^S - S_X\omega\left(\omega^2 - \omega_R^2\right) \\ \lambda\omega A_Y^S - S_Y\omega\left(\omega^2 - \omega_R^2\right) \end{pmatrix}\Bigg].
\end{aligned} \tag{2.25}$$

2.3.2 Lineshape of the FMR spectrum

We have obtained explicitly $m_{X,Y}(t)$ in the last subsection, so we can now evaluate the lineshape function:

$$\begin{aligned}
L_S(\omega) &= 2\left\langle -\cos(\omega t)\left(m_X(t)\,p_X + m_Y(t)\,p_Y\right)\right\rangle = \\
&\quad -\frac{\left(A_X^S p_X + A_Y^S p_Y\right)\left(\omega^2 - \omega_R^2\right) + \lambda\omega^2\left(S_X p_X + S_Y p_Y\right)}{\left(\omega^2 - \omega_R^2\right)^2 + \lambda^2\omega^2}
\end{aligned}$$

It is convenient to put the above expression in terms of

$$\begin{aligned}
S &= -\left(S_X p_X + S_Y p_Y\right), \\
A_S &= -\left(A_X^S p_X + A_Y^S p_Y\right).
\end{aligned}$$

then:

$$L_s(\omega) = \frac{A_S\left(\omega^2 - \omega_R^2\right) + \lambda\omega^2 S}{\left(\omega^2 - \omega_R^2\right)^2 + \lambda^2\omega^2} \tag{2.26}$$

$L_s(\omega)$ is a dimensionless function that defines the "lineshape" of the FMR lineshape. Finally:

$$\delta V = \frac{R_0 P^2 I_{RF}^0}{2\left(1 + P^2\cos\theta_0\right)^2} L_S(\omega) \tag{2.27}$$

Equation 2.27 together with 2.26 are is the main result of this chapter.

2.3.3 Lineshape features

The factors S and A_S are quatities related to the symmetric and antisymmetric components of the lineshape. Since A_S has units of frequency^2 while S has units of frequency, it is convenient to define

$$A_S^* = \frac{A_S}{\omega_R} \tag{2.28}$$

knowledge of the relative magnitude of A_S^* in comparison with S, as well as their respective signs, gives out valuable qualitative information of the shape of $Ls\,(\omega)$ around ω_R, as is shown in figure 3.11.

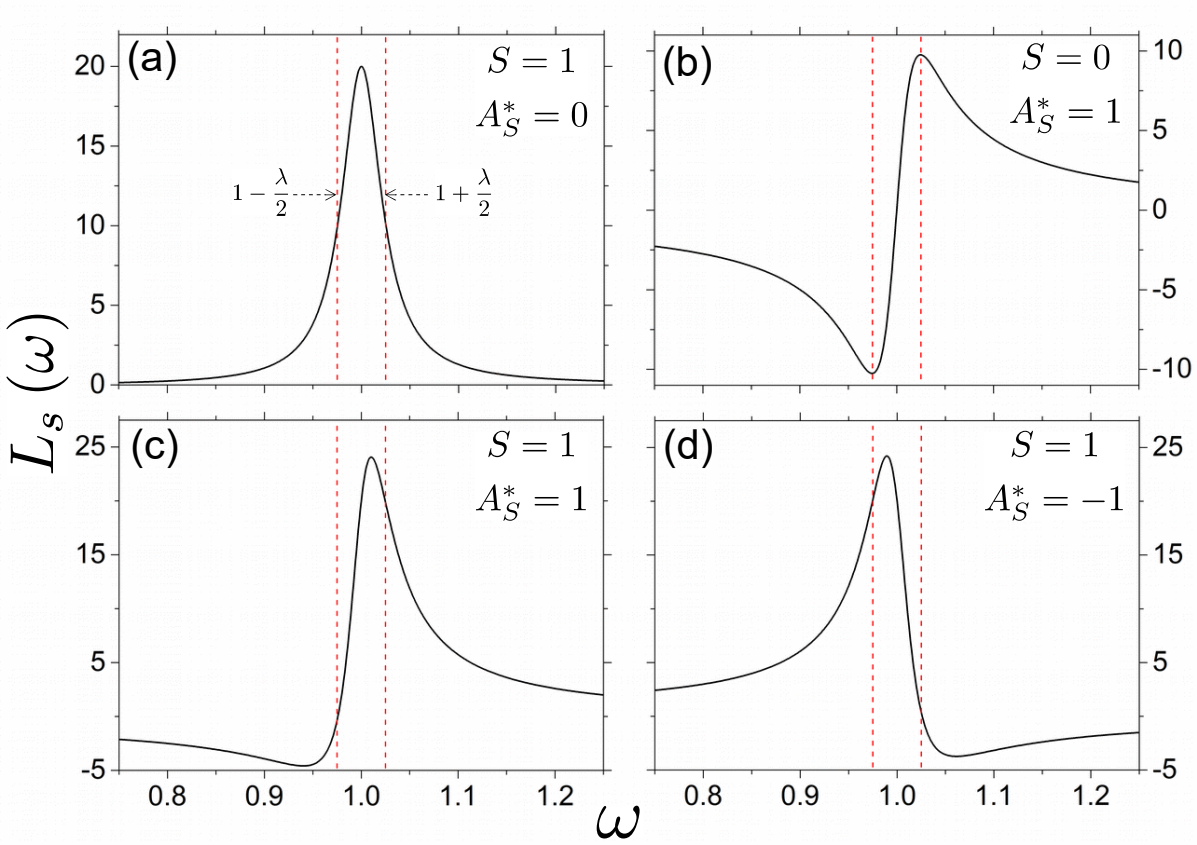

Figure 2.4: Lineshape function $L_s\,(\omega)$ plotted for different values of S and A_S^*: (a) and (b) show the completely symmetric and asymmetric case, respectively; (c) and (d) show the sum of a completely symmetric and antisymmetric $L_s\,(\omega)$ with equal and opposed signs, respectively. Red dashed vertical lines demarcate the ω region of width λ centered at the resonance frequency ω_R. All the quantities are normalized to ω_R, except for $L_s\,(\omega)$ which is dimensionless.

After some algebra, it is possible to show that for a completely symmetric lineshape ($A_S^* = 0$), ω_R is the resonance frequency i.e. the frequency where $L_s\,(\omega)$ takes its maximum amplitude. Furthermore, this maximum value is equal to $|S\lambda|$ and λ is the full width at half maximum of the peak.

On the other side, for a completely asymmetric lineshape ($S = 0$), ω_R is the the frequency where $L_s(\omega)$ makes null. Moreover, for $\lambda \ll \omega_R$, the values of ω where $L_s(\omega)$ takes its extreme values are given by $\omega_R \pm \lambda/2$ (see figure 3.11) and the absolute value of $L_s(\omega)$ at those points is equal to $|A_S^*/(2\lambda)|$.

2.4 Special cases

In the following sub-sections expressions for S and A_S^* in experimentally relevant configurations will be derived and compared with published results. In all the exposed cases $\mathbf{p}$ points along the $+\widehat{\mathbf{x}}$ axis. Also, second order terms arising from the expansions of S and A_S^* have been disregarded.
Notice that all the parameters on which δV depends can be readily obtained from the information given in the articles, with the exception of I_{RF}^0, which is amplitude of the microwave current that is actually reaching the MTJ. I_{RF}^0 can not be determined directly from the power applied to the MTJ, due to the unexpected impedance mismatch in microwave circuits. The work of Sankey et al. [35] presents a method to obtain I_{RF}^0 from the non-resonant background arising from the first term of equation 2.2. However all the other works cited here, do not provide such information. Therefore, only the lineshape features are predicted the magnitude of the prefactor in 2.2 is disregarded. In any case, this is not importnat being that the relevant physics can be inferred from the symmetric and asymmetric part of $L_s(\omega)$.

2.4.1 m spanning the x-y plane

This configuration can be seen in the works of Sankey et al.[35] and Kubota et al. [42]. The VCMA effect is null since $\mathbf{m}$ lies in the plane.
Nonetheless, this case is included because is important to verify that our predictions are also applicable to purely STT experiments. It is obtained that:

$$\frac{S}{I_{RF}^0\gamma^*} = \beta'_{\parallel}\sin^2\varphi, \tag{2.29}$$

$$\frac{A_S^*}{I_{RF}^0\gamma^*} = -\beta'_{\perp}\sin^2\varphi \times \left[\gamma^*\omega_R^{-1}\left(M_{eff} + H_u\cos^2(2\varphi) + H\cos\phi_H\cos(\varphi-\varphi_H)\right)\right]. \tag{2.30}$$

It is readily seen that S (A_S^*) is always proportional to the IP-STT (FL-STT) component of STT vector. Also, both S and A_S^* are proportional to $\sin^2\varphi$, however A_S^* includes an extra, dimensionless factor (inside the square brackets) that may modify its proportion respect to the S component. We can check the validity of our predictions looking at the figure 2.5 taken from reference [35]. The Figure shows the ST-FMR peaks for different DC biases. For $I_{DC} = 0$ (figure 2.5(b)), the lineshape is completely symmetric, indicating that $\beta'_{\perp}$ makes null at zero current. For $I_{\mathrm{DC}} < 0$ (figure 2.5(a)), the contribution of the asymmetric part is significative and has equal sign respect to the symmetric one, confirming the predictions of equations 2.29 and 2.30. For $I_{DC} > 0$ the asymmetric part is roughly of the same amplitude as for negative current but its sign is

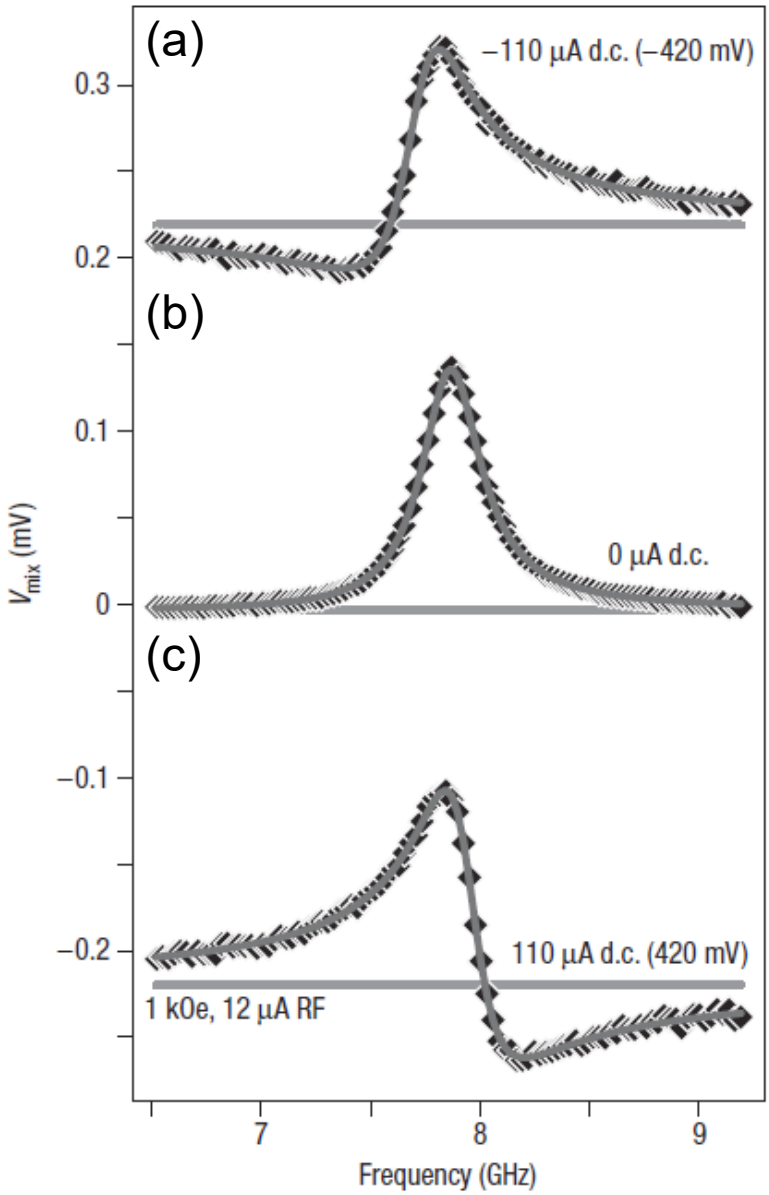

Figure 2.5: Spin rectified voltage on a magnetic tunnel junction, for negative (a), zero (b) and positive (c) values of I_{DC}. **p** and **H** point in $+\mathbf{x}$ and $+\mathbf{y}$ directions respectively and **m** is aligned with **H** which has a magnitude of 0.1T. Reprinted with permission from [35].

opposite (figure 2.5(c). These observations are consistent with a model of STT in which $\beta_{\parallel}$ is linear and $\beta_{\perp}$is quadratic on current, so $\beta'_{\parallel}$ is a constant and $\beta'_{\perp}$ is linear on it.

2.4.2 m spanning the x-z plane

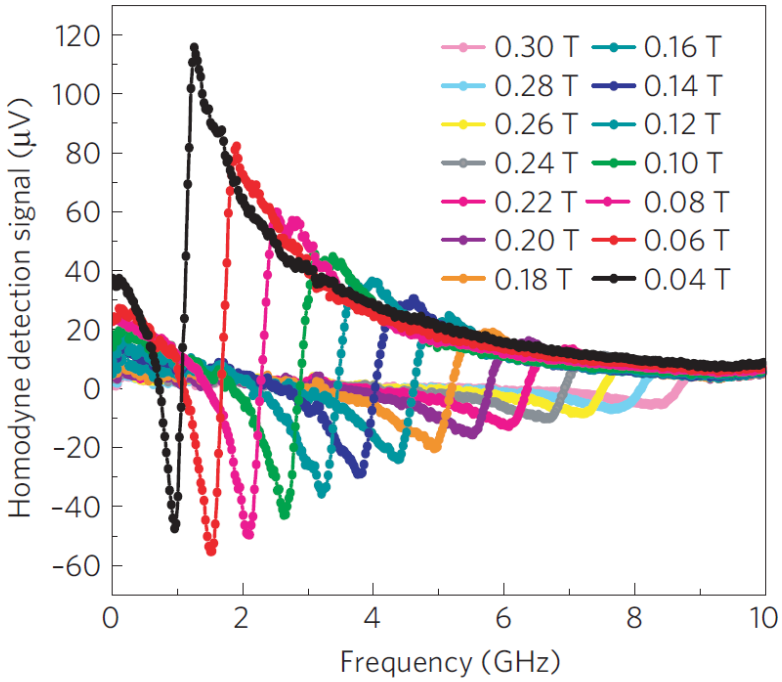

Figure 2.6: Spin rectified voltage on a magnetic tunnel junction (MTJ) at different magnitudes of the magnetic field **H**, which lies within the x-z plane and has an elevation angle of $\phi = 55°$. It is assumed that **m** is approximately aligned with **H**. In this experiment, only VCMA is present as the lateral dimensions of the MTJ are micrometric ($1 \times 1\mu m^2$). Reprinted with permission from [34]

This configuration can be seen in the Refs. [34],[13] and in one of the cases of reference [43]. The results are reproduced on Figs. 2.6, 2.7 and 2.8. Notice that in the last case the magnitude of the magnetic field was swept at a fixed microwave frequency, and consequently our model is not applicable from a quantitative point of view, however, we expect the same qualitative lineshape features, provided that the resonant frequency is a monotonic function of the resonant field.
The following expressions for S and A_S^* are obtained for this configuration:

$$\frac{S}{I_{RF}^0 \gamma^*} = \beta'_{\parallel} \sin^2\phi, \tag{2.31}$$

$$\frac{A_S^*}{I_{RF}^0 \gamma^*} = (-\beta'_{\perp} + \beta'_V \cos\phi\cos\varphi)\sin^2\phi \times \left[\gamma^* \omega_R^{-1}\left(H_u \cos^2\phi - M_{eff}\sin^2\phi + H\left(\cos\phi\cos\varphi\cos\phi_H\cos\varphi_H + \sin\phi\sin\phi_H\right)\right)\right], \tag{2.32}$$

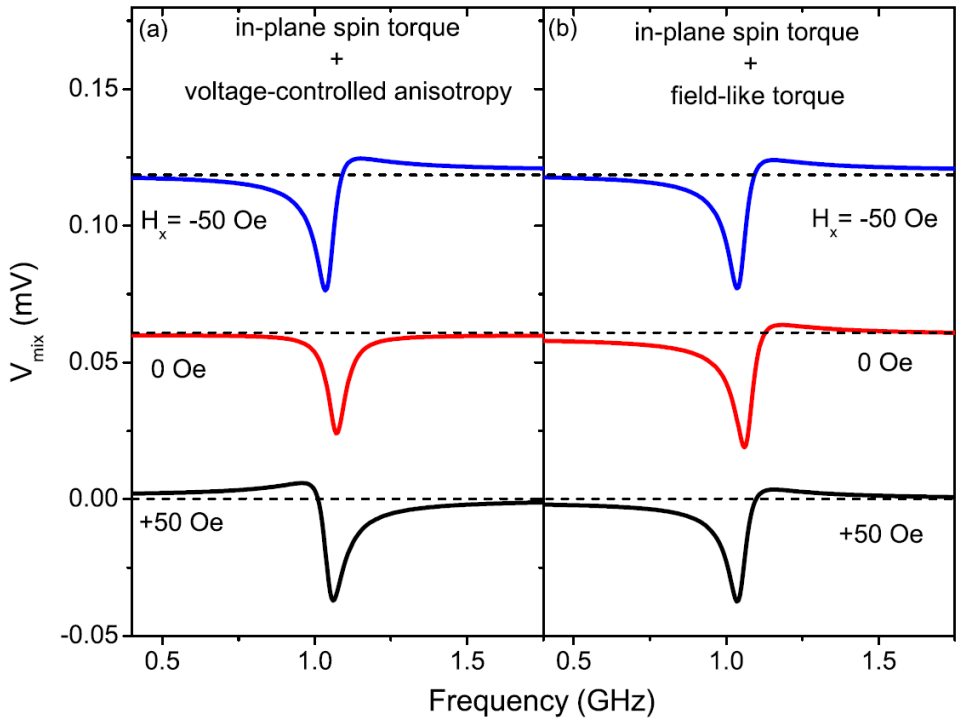

Figure 2.7: Macrospin simulations of the spin rectified voltage on a MTJ arising from the combined action of VCMA and STT effects. In (a) there is zero FL-STT (IP-STT+VCMA) whereas in (b) there is zero VCMA (IP-STT+FL-STT) . **H** points in the $\pm\mathbf{x}$ direction and the free layer has a small net PMA. Reprinted with permission from [13]

where φ can take only the values 0 or π.
One of the main outcome of equations 2.31 and 2.32 is that in the absence of STT the lineshape will be always completely asymmetric. This can be confirmed in figure 2.6 extracted from the work of Nozaki et al.[34] and figure 2.8 extracted from the work of Shiota et al. [43] (filled squares plots). In above mentioned works, only the VCMA effect is present since the lateral dimensions of the studied MTJs are micrometric. Notice that the results show that the sign of A_S^* is different in each case. This may be explained because in the experiment of reference [34], $\mu_0 M_{eff}$ is small in comparison to H, being that the thickness of the free layer was intentionally tunned to cancel the demagnetizing field, so the sign of the factor inside the square parenthesis is positive. On the other side, for the experiment of reference [43], $\mu_0 M_{eff}$ is large in comparison to H, being that the free layer is thin enough (2.0 nm) to have no net PMA, so the sign of the factor inside the square parenthesis is negative. Another important feature predicted by equation 2.32, which is confirmed in the work of reference [43], is the sign reversal of A_S^* upon direction reversal of **H** (see figure 2.8). This is originated by the $\cos\varphi$ factor accompanying β_V' in equation 2.32: when φ changes from 0 to π, A_S^* reverses its sign. The interplay between STT and VCMA is studied on the work of Zhu et al. [13]. It is mentioning that in the above mentioned paper the sign convention for the current is opposite to the employed in my calculations (and opposite to all other examples showed

here), so the expressions for S and A_S^* in equations 2.31 and 2.32 must be considered as multiplied by -1. Another important feature of this work is that FL-STT was assumed to be linear on the current, so $\beta'_\perp$ is constant and has a finite value when $I_{DC} = 0$.
The figure 2.7 was extracted from the above mentioned work, and show macrospin simulations of the SRE voltage around the resonance frequency. In Figure 2.7(a) is shown the case in which both IP-STT and VCMA are present whereas in figure 2.7(b) IP-STT and FL-STT are present. The free layer has a small net PMA, so at zero magnetic field, **m** points out of the plane ($\phi \simeq \pi/2$).
When $\mathbf{H} = \pm 50$ Oe $\widehat{\mathbf{x}}$, there is a small deviation of ϕ respect to the normal, so a reversal of **H** leads to a sign reversal of m_x, which is equivalent to a change from $\varphi = 0$ to π in equation 2.32.
Then, according to expression 2.32, for the IP-STT + VCMA case ($\beta_\perp = 0$), A_S^* reverses its sign upon reversal of **H** (see figure 2.7(a) for $H_x = \pm 50$ Oe). Moreover when **H** makes null, A_S^* also does, so the lineshape becomes completely symmetric (see figure 2.7(a) for H_x=0). In contrast, for the IP-STT + FL-STT case ($\beta_V = 0$), A_S^* does not reverse its sign upon reversal of **H** (see figure 2.7(b) for $H_x = \pm 50$ Oe) and hence does not makes null for $\mathbf{H} = 0$ (see figure 2.7(b) for H_x=0).

2.4.3 m spanning the y-z plane

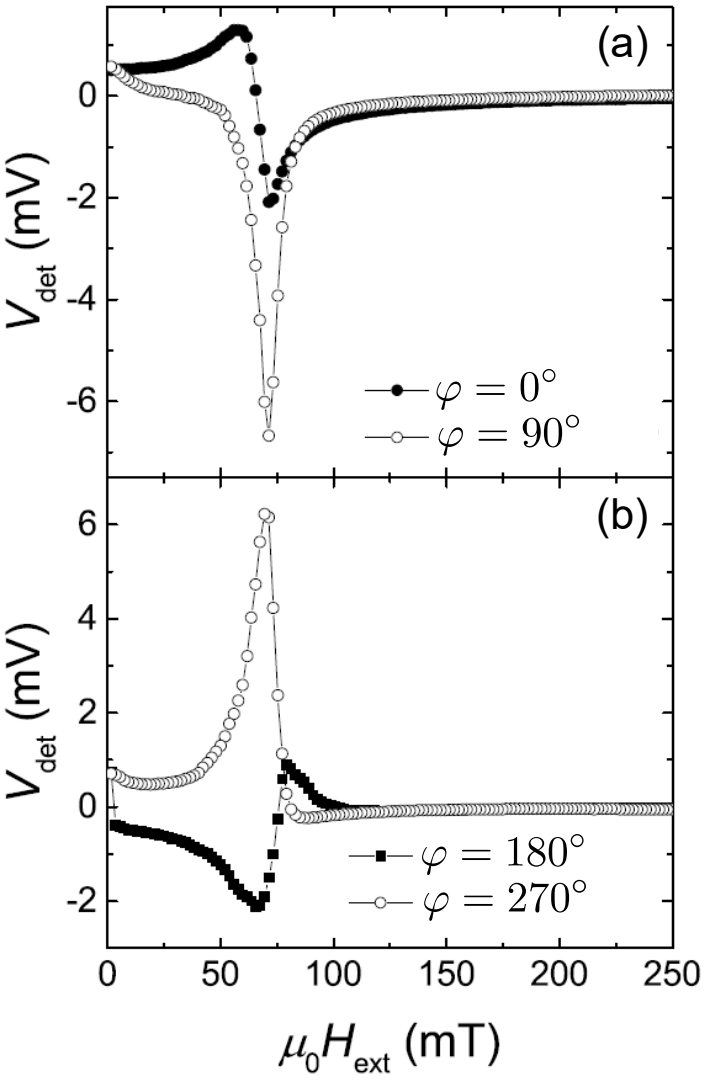

Figure 2.8: Spin rectified voltage on a magnetic tunnel junction (MTJ) at RF frequency of 1.0 GHz and different orientations of the magnetic field **H**: (a) $\varphi = 0°$ (filled squares) and $\varphi = 90°$ (open circles), (b) $\varphi = 180°$ (filled squares) $\varphi = 270°$. In this experiment, only VCMA is present as the lateral dimensions of the MTJ are micrometric ($1 \times 4\mu$ m^2). Reprinted with permission from [43]

This configuration has been studied only in two of the SRE measurements reported in the reference [43], which are reproduced in Fig. 2.8: open circle plots in figure 2.8(a) and 2.8(b) corresponds to $\varphi = \pi/2$ and $\varphi = -\pi/2$ cases respectively. In such case, the lateral dimensions of the structure ($1 \times 4\mu$m^2) are large enough to ensure that STT is

not present. The S and A_S^* components of the lineshape will be:

$$\frac{S}{I_{RF}^0\gamma^*} = \beta'_{\parallel} - \frac{1}{2}\beta'_V \sin(2\phi)\sin\varphi \tag{2.33}$$

$$\frac{A_S^*}{I_{RF}^0\gamma^*} = -\beta'_{\perp} \times \left[\gamma^*\omega_R^{-1}\left(M_{eff}\cos(2\phi) + H\left(\cos\phi\cos\phi_H\sin\varphi\sin\varphi_H + \sin\phi\sin\phi_H\right)\right)\right] \tag{2.34}$$

where φ can take only the values $-\pi/2$ and $\pi/2$.
According to the above equations, in absence of STT, the lineshape will be always completely symmetric and the sign of S reverses upon **H** reversal, which is confirmed from Fig.2.8. Moreover, the sign of S is also correctly predicted in each case.
An interesting feature predicted for equations 2.33 and 2.34 is the interplay between the IP-STT and VCMA effects in the symmetric part of the lineshape that would result in a cancellation ($\varphi = \pi/2$) or a reinforcement ($\varphi = -\pi/2$) of it. This contrast with all the other experimental configurations presented here, in which they never form part of S at the same time. This is interesting, since the maximization of S is a more efficient way for increasing the magnitude of δV than A_S^* (see figure 3.11), and, being that these effects usually are both much stronger than the FL-STT in MTJs. Then this configuration is optimal for maximizing the sensitivity of the MTJs thinking on its potential application as r.f. diode[44]. Up to date, I have not found reported experiments in that direction.

2.5 Summary

I have obtained general analytic expressions for the spin rectified voltage across magnetic tunnel junctions and spin valve nanopillars of elliptical cross section, subjected to an microwave oscillating current applied perpendicular to the plane. The model accounts for the simultaneous existence of spin transfer torque (STT), both in-plane and field-like, and voltage controlled magnetic anisotropy (VCMA). The relative magnitudes of those effects can be obtained from the analysis of the lineshape of the ferromagnetic resonance (FMR) spectrum. Our results are applicable for arbitrary applied magnetic field vector, magnetization vector of the polarizer layer and lengths of the elliptical major and minor axis . Overall, the results are in excellent agreement with the experimental results published on this subject, which in summary are particular cases of the general model exposed here. These results may be useful for future experimental works aimed to distinguish and quantify the STT and VCMA effects through ferromagnetic resonance spectroscopy in nanostructures. Moreover, these results will be a guideline to optimize the rectified voltage, considering the application of these devices as r.f. diodes.

Chapter 3

g-factor determined by ferromagnetic resonance

3.1 Introduction

Since its discovery in 1946 [45], ferromagnetic resonance spectroscopy (FMR) has been an essential tool in the area of experimental magnetism. FMR is a widely employed tool to probe multiple dynamic and static properties of magnetic materials, like the spectroscopic g-factor, saturation magnetization, magnetic damping and magnetocrystalline anisotropies.
In recent times, broadband FMR is being increasingly adopted. In this variant of FMR, the microwave magnetic fields reach the sample through a coplanar waveguide unlike the classic FMR in which the sample must be introduced in a fixed-frequency microwave cavity. Therefore it is possible to set many different frequencies without altering the experimental set-up. With the use of broadband FMR, the most important magnetic parameters can be determined in a matter of minutes.
Among all the parameters that can be determined with broadband FMR, g and M_s are always present. Determination of g is important because unlike M_s there are almost no experimental technique other than FMR to find it . Moreover g value is directly related to the relative contribution of the orbital and spin angular momentum to the total magnetic moment a ferromagnet.

$$\frac{\mu_L}{\mu_s} = \frac{g-2}{2} \tag{3.1}$$

Since the orbital angular momentum is largely quenched by the crystalline field in bulk 3d ferromagnets, the value of g is generally quite close to 2. Two mechanisms may contribute to the incomplete quenching of the orbital momentum leading to perturbations on that value, one is the spin-orbit coupling of the electrons of the d-band and the other is the reduction of the crystalline field symmetries at the interfaces of ultrathin ferromagnetic films. The study of the above effects thus requires measuring g with very high accuracy, however the determination of g with better than 1% precision has been tricky with the use of in-plane broadband FMR technique [9, 46]. For example in the case of bulk Permalloy there is large spreading of the values of g given the literature.

Recently the work of Shaw et al. [47] dealt with this problem: they attributed the large spreading of the values of g and M_s among the literature, to the differing ranges of frequencies employed among the different broadband FMR experiments. To solve this problem, they presented a data analysis methodology in which the correct value of g and M_s are determined by extrapolating their fitted values to the case in which the range of frequencies goes to infinity.
In this chapter we study theoretically two sources of systematic error propagation in broadband FMR experiments that may have spoiled the correct determination of g and M_s in previous studies, as well be the cause of the apparent dependence of their values on the range of frequencies employed. One is the incorrect determination of the static magnetic field in the place where the sample is, and the other is the disregarding of the presence of in-plane anisotropy terms. We test our results with simulated and real broadband FMR data of a Ni_80Fe_20 (Permalloy) sample.
Furthermore, we propose and test experimentally a simple methodology to reduce significantly the above mentioned sources of systematic errors..

3.2 Propagation of systematic errors in the Kittel equation

It is well known that in the in-plane geometry the relationship between the frequency and resonance magnetic field is given by [48]:

$$f = \frac{g\mu_B\mu_0}{h}\left[H_{res}\left(H_{res}+M_s\right)\right]^{1/2} \tag{3.2}$$

Where h is Plank's constant, μ_0 is the permeability of free space, and μ_B is the Bohr magneton. The way to obtain g and M_s in broadband ferromagnetic resonance is simple fit of the resonance fields for a set of different frequencies with the above expression. In the next section we analyze how large is the deviation of g and M_s from its actual values due to an error in the measurement of H_{res}.

3.2.1 g error propagation

To start with, we put Eq. 3.2 in terms of g

$$g = \frac{fh}{\mu_0\mu_B}\left[H_{res}\left(H_{res}+M_s\right)\right]^{-1/2} \tag{3.3}$$

The error propagation is simply the derivative of g respect to H_{res}

$$\frac{dg}{dH_{res}} = -\frac{fh}{2\mu_0\mu_B}\left(2H_{res}+M_s\right)\left[H\left(H_{res}+M_s\right)\right]^{-3/2}$$

Replacing with Eq. 3.2

$$\frac{dg}{dH_{res}} = -\frac{g\left(2H_{res}+M_s\right)}{2H_{res}\left(H_{res}+M_s\right)} \tag{3.4}$$

It is more clear to put the error propagation in terms of f, to do so, we solve Eq. 3.2 for H_{res} and replace into Eq. 3.4, to obtain

$$\frac{dg}{dH_{res}} = -\frac{g\left[1+4\overline{f}^2\right]^{1/2}}{2M_s\overline{f}^2} \tag{3.5}$$

were

$$\overline{f} = \frac{hf}{g\mu_0\mu_B M_s} \tag{3.6}$$

3.2.2 M_s error propagation

We start applying derivative respect to M_s in Eq. 3.3

$$\frac{dg}{dM_s} = -\frac{H_{res}fh}{\mu_0\mu_B}\left[H_{res}\left(H_{res}+M_s\right)\right]^{-3/2} \tag{3.7}$$

Applyig chain rule with Eq. 3.4

$$\frac{dM_s}{dH_{res}} = \frac{dg}{dH_{res}}\left(\frac{dg}{dM_s}\right)^{-1} = \frac{(2H_{res}+M_s)}{H_{res}} \tag{3.8}$$

We put this in terms of f

$$\frac{dM_s}{dH_{res}} = 2 + u^{-2} + \frac{(1+4u)^{1/2}}{2u^2} \tag{3.9}$$

Eqs. 3.5 and 3.9 are the main results of this section.
Fig. 3.1. shows the error propagation vs frequency using the standard values of g and M_s of bulk $Ni_{80}Fe_{20}$ ($g = 2.11$ and $\mu_0 M_s = 1.02$ T). Notice that the signs of the error propagation on g and M_s are always opposite and the vertical scale is logarithmic. To illustrate how large can be the deviations of g and M_s in this case, let's assume that for example we measure the resonance fields vs frequencies in a range of frequencies around f=3 GHz and our Hall sensor is miscalibrated in such a way that it gives a value of the magnetic field that is 15 Oe below the actual one. According to Fig.3.1 the fittings will give us a value of $g = 1.95$ and $\mu_0 M_s = 1.22$ T. If the frequency were 20 GHz, the given values would be much more close: $g = 2.10$ and $\mu_0 M_s = 1.01$ T
The later example shows how a relative small shift of the measured magnetic field can lead to a relatively large systematic deviations of g and M_s from their actual values, especially at low frequencies. This may explain the large spreading of the values of g than can be found in the literature for Permalloy [47].
A recently published paper from Shaw et al. [47] was devoted this problem: they propose a methodology to resolve the exact value of g with less than 1% precision. They found that there is a significant variation of the value of the g depending on the range of frequencies employed to the fitting: if the range selected goes from 4GHz to f_{up}, the value of g progressively goes up approaching the convergence value (g=2.11) as f increases, starting from $g = 2.01$ at $f_{up} = 20$ GHz and ending at $g = 2.10$ at $f_{up} = 60$ GHz. On the other side, the value of M_s converges in the the opposite way: goes down approaching the actual value $\mu_0 M_s$=1T decreasing from higher values as f_{up} increases. Our calculations show that this behavior may be explained from the systematic error propagation arising from a shift of the measured magnetic field respect to the actual one.

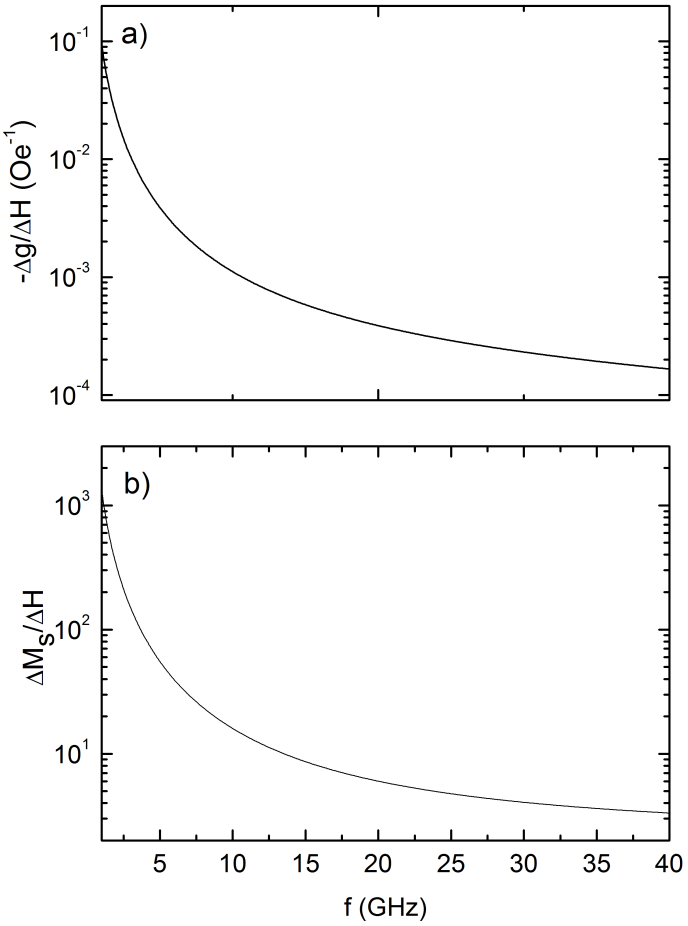

Figure 3.1: Error propagation for g (a) and (b) M_s respect to measured value of H_{res} . Notice that the vertical scale is logarithmic and that the sign of the g error propagation is negative

3.3 Simulated results

In order to better visualize and test our results , we have performed fittings on simulated ferromagnetic resonance data adding a shift in the magnetic field . The parameters chosen were $g = 2.11$ and $\mu_0 M_s = 1$T corresponding to bulk permalloy [47]. The procedure is as follows: values of H_{res} are calculated solving exactly Eq. 3.2 setting $f = 2$ GHz up to $f = 20$ GHz in steps of 0.5 GHz. The values of H_{res} are then incremented or reduced in 5 Oe. We fit the altered data with the Kittel equation without include any extra fitting parameters, in a range that goes from $f = 2$ GHz up to f_{up} with f_{up} going from 10 to 20 GHz. The fitted values for g and M_s are then plotted vs f_{up}. The results are shown in Fig. 3.2. In the first case, plotted in black filled circles the measured values of H_{res} are 5 Oe below the actual value, i.e. δH =-15 Oe, whereas in the second case, shown in black open circles panel of the same figure, the measured values of H_{res} are 5 Oe above the actual values, i.e. δH =5 Oe.
It is worth mentioning that the true values of g, $\mu_0 M_s$ and the magnitude of δH were

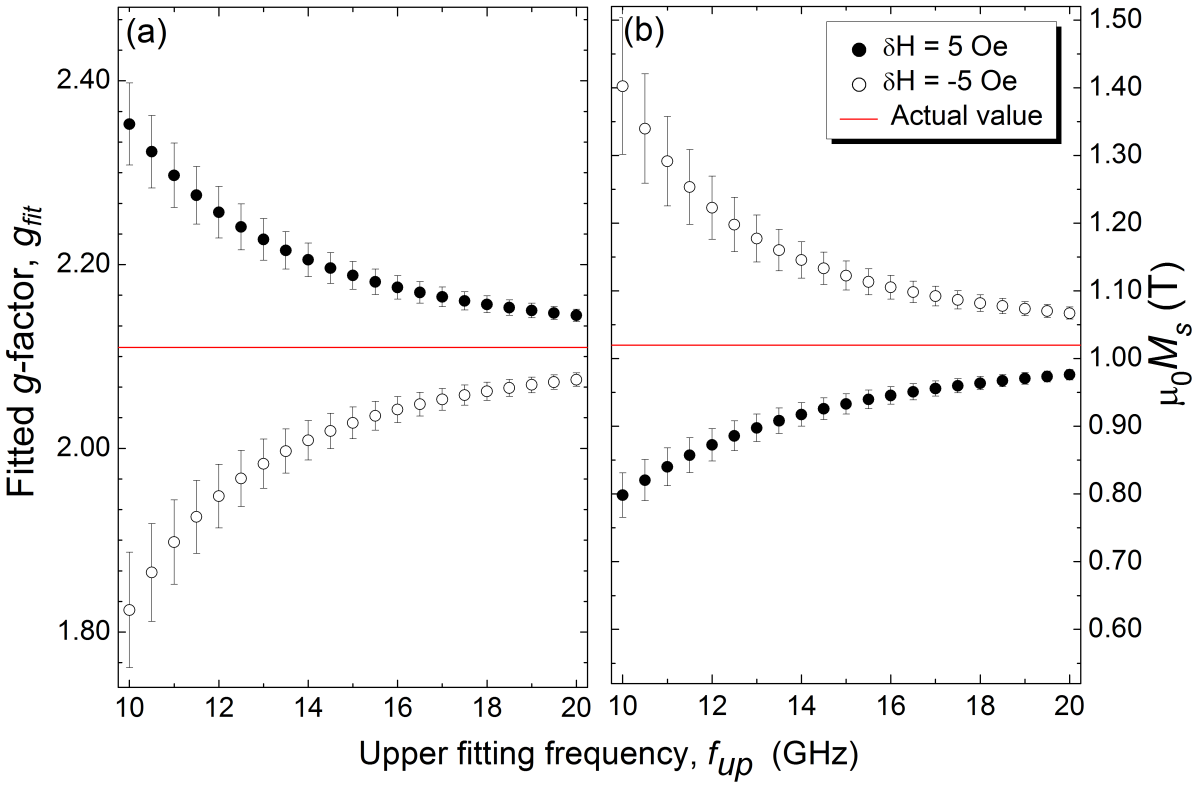

Figure 3.2: Fitted values of g (a) and $\mu_0 M_s$ (b) vs upper fitting frequency (f_{up}) of the simulated data, in which the exact values of the resonance magnetic field H_{res} were altered by adding a positive (black, filled circles) and negative shift (black, open circles) of 5 Oe to its exact value.

deliberately chosen to better comparison with Fig. 2 of reference [47].
It this clear from Fig. 3.2 that the magnetic field shift, positive or negative, produces significant systematic deviations of g and M_s respect to the actual values. This deviations, in each case, have opposite signs and decrease as more high frequency data is included, all of which is in accordance with Eqs. 3.5 and 3.9.

3.4 Experimental methodology

A 5 nm thick film of $Ni_{80}Fe_{20}$ (Permalloy) was dc magnetron sputtered at room temperature onto a Si/SiO_2 substrate and subsequently capped with 1.5 nm of Al to prevent oxidation . The base pressure of the chamber was less than 3 x 10^{-8} Torr and the substrate was rotated during all the process to inhibit the formation of in-plane magnetic anisotropies. The Broadband FMR measurements were performed in a NanOsc PhaseFMR instrument with a 200-μm-wide coplanar waveguide (CPW). The DC magnetic field H generated by the electromagnet is modulated with a low frequency (490 Hz) field $h_{ac}(t)$ parallel to H generated by Helmholtz coils attached to magnet poles Fig. ??(a). Since the sign of H is just a matter of convention, we have defined the positive values of H as cases in which the magnetic field vector points to the pole with

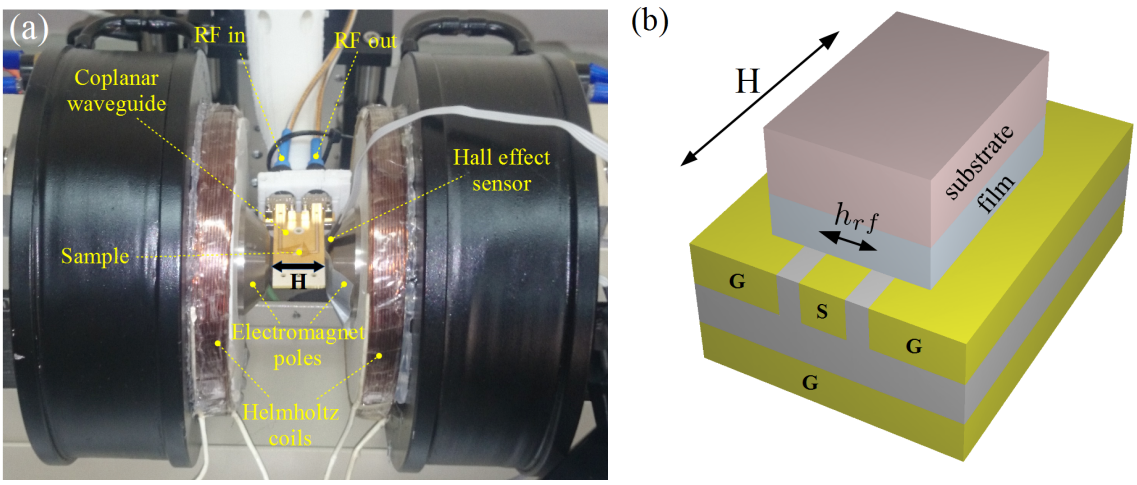

Figure 3.3: (a) Picture of the broadband FMR set-up indicating his main components.(b) Diagram of a slice of the coplanar waveguide with the sample on it.

the Hall sensor attached (see Fig. ??(a)).
The sample is put face down on the waveguide and a microwave signal of frequency f is injected into the waveguide through the RF-in cable. The sample is thus subjected a microwave field h_{rf} perpendicular to the modulated field $H + h_{ac}(t)$ (Fig. ??(b)). The returning signal is injected into the PhaseFMR instrument through the RF-out cable, its microwave component is rectified by a RF diode and then injected in a lock-in amplifier whose reference signal source is the same that the one of the modulating field $h_{ac}(t)$. The signal detected by the lock-in is thus proportional to the slope of S_{21} parameter. Two sets of measurements were done, one with positive and other with negative values of H. In both cases the magnitude of the H was varied from 0 to 3.5 kOe and f was varied from 3 GHz to 17 GHz in steps of 0.5 GHz.
To estimate the actual value of H were the sample is, the following procedure is carried out: A Hall effect sensor is placed at the middle point of the gap between the poles of the electromagnet, as shown in Fig. 3.4 (a). This Hall effect sensor is connected to an external gaussmeter and we assume that its reading is equal to the value of H felt by the sample in the measurement configuration (Fig. 3.4 (b)). A second Hall effect sensor is permanently fixed to one of the poles and connected to the internal gaussmeter of the PhaseFMR instrument, we denote the reading of this sensor H_P. Then, a wide set of DC current values are injected into the electromagnet in order to vary H across the full possible range. The readings of both Hall effect sensors are collected and linear relationship is established between them by fitting with:

$$H = C_1 H_P + C_2 \tag{3.10}$$

where C_1 and C_2 are the fitting constants. The values of C_1, C_2 are grabbed by PhaseFMR instrument allowing it to interpolate H by the reading of H_P when executing the FMR measurements. It should be noted that in the ideal case, the value of C_2 must be always 0, given that there is no reason to get a non-zero value for H when $H_P = 0$. However, having performed the calibration protocol described above in a set of independent FMR experiments, we found that C_2 varies typically around $\pm$ 25 Oe.

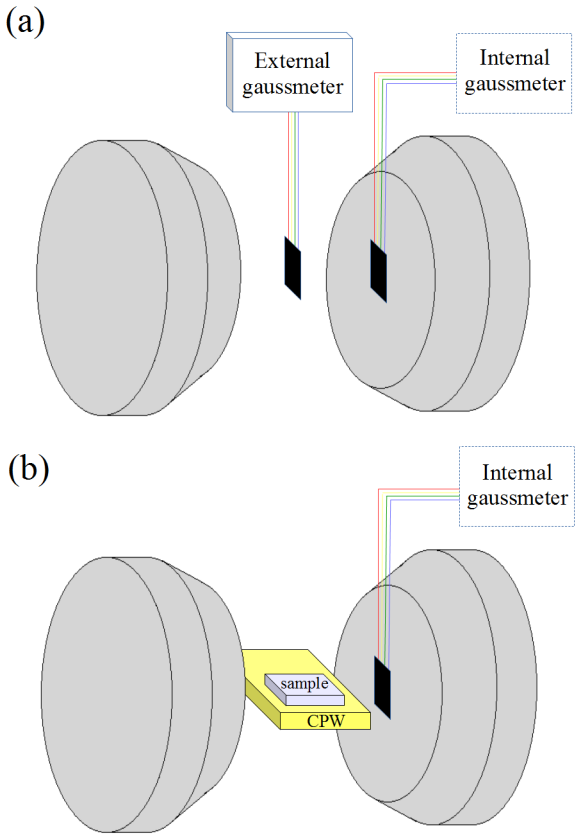

Figure 3.4: Magnetic field calibration steps: (a) An external Hall effect sensor is placed in the gap between the magnet poles and its readings are correlated with another permanently attached to one of the poles, (b) During measurements the value of H felt by the sample is interpolated by the reading of the fixed Hall effect sensor.

3.4.1 Results and discussion

The H spectrum recorded for each value of frequency was fitted by the derivative of the sum of an symmetrical and antisymmetrical Lorentzian [38]:

$$P = \frac{d}{dH}\left[\frac{S\left(\Delta H\right)^2 + A_S\left(H - H_{res}\right)}{4\left(H - H_{res}\right)^2 + \left(\Delta H\right)^2}\right] \tag{3.11}$$

Where S, A_S, H_{res} and ΔH are the symmetric, antisymmetric, resonance field and linewidth of the FMR peak respectively. An example of the obtained H spectrum at f= 10 GHz and the corresponding fit with Eq. 3.11 is shown in Fig. 3.5 (a). The overall results for H_{res} values in the two set of experiments are summarized in Fig. 3.5 (b). H_{res}^{+}, $|H_{res}^{-}|$ stand for the absolute values of H_{res} with $H > 0$, $H < 0$ respectively. We found that, on average, the values of H_{res}^{+} are 35 Oe above $|H_{res}^{-}|$, this may more clearly seen in the inset of Fig. 3.5 (b). However, given the symmetries of our experiment, if our calibration procedure were perfect both values should be the same. We then infer that there must be shift of the measured values of H_{res} of magnitude $|\delta H|$=17.5 Oe respect

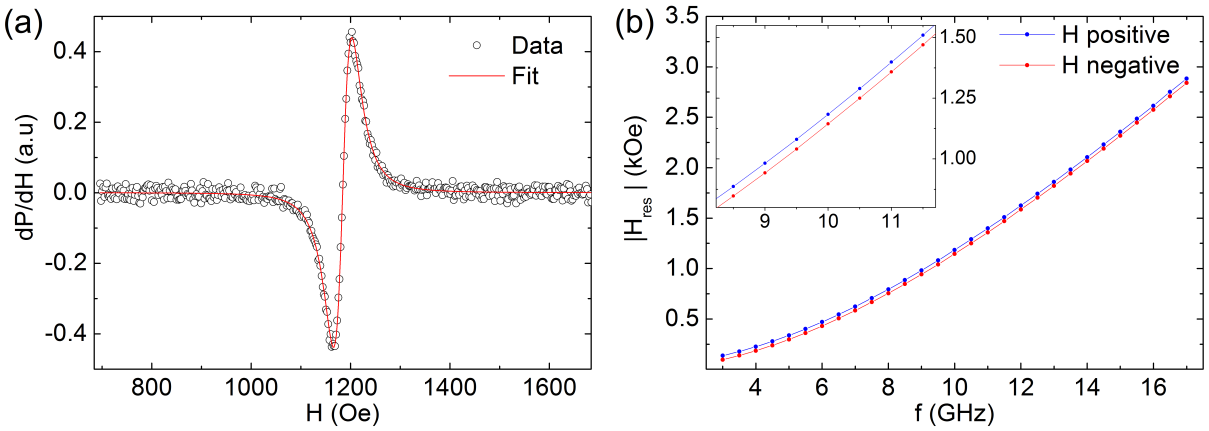

Figure 3.5: (a) Resonance spectra for f=10 GHz and the least squares fitting .(b)$|H_{res}|$ vs F for opposite directions of the magnetic field. Inset: zoom in the 8.5 to 11.5 GHz range

to their actual values, that is, the actual values of H^{+}_{res} and $|H^{-}_{res}|$ should be better approximated by H^{+}_{res}-δH and $|H^{-}_{res}| + \delta H$ respectively. Therefore there is an equal but opposite sign shift in the measured magnetic field in the two set of experiments, pretty much in the same way as the example we presented in the simulated data section .
We then did the analysis of the variation of g and M_s vs f_{up} in the same a we did for the simulated data. The results are shown in Fig. 3.6. It is observed that the values of g and M_s follows the same trends than the simulated ones confirming our predictions, though in the case of negative ΔH, the deviation is lower. We now propose a method to minimize the effect of magnetic field shift, taking the average of the values of H^{+}_{res} and $|H^{-}_{res}|$ as a more accurate value of $|H_{res}|$

$$H^{av}_{res} = \frac{H^{+}_{res} + |H^{-}_{res}|}{2} \tag{3.12}$$

We tested our method repeating the same analysis to g and M_s vs f_{up}, now using the H^{av}_{res} values in the fittings, the results are plotted on Fig. 3.6 in red squares. It can be observed that the new results showed a much smaller variation in the value of g and M_s: around only a 3 percent, in comparison with the H^{+}_{res} and $|H^{-}_{res}|$ results, which varied up to 50 percent. The average values of g and $\mu_0 M_s$ across the f_{up} variation were 2.11 and 0.87 T respectively. We expect these values to be much more close to the true values than the ones obtained from the fittings with H^{+}_{res} and $|H^{-}_{res}|$ values.
The later may be confirmed comparing our result for g with the one obtained by Nibarger et al. [49], whom measured the value $g \simeq 2.05$ for a 5nm thickness NiFe sample, despite in the later case the studied sample was fabricated in a way to produce significant in-plane magnetic anisotropy.

3.5 Inclusion of In-plane anisotropy

It is seen in Fig. 3.6, the values of g and M_s after the magnetic field correction (red filled squares) still show a slight variation on f_{up}, suggesting that there is still a source

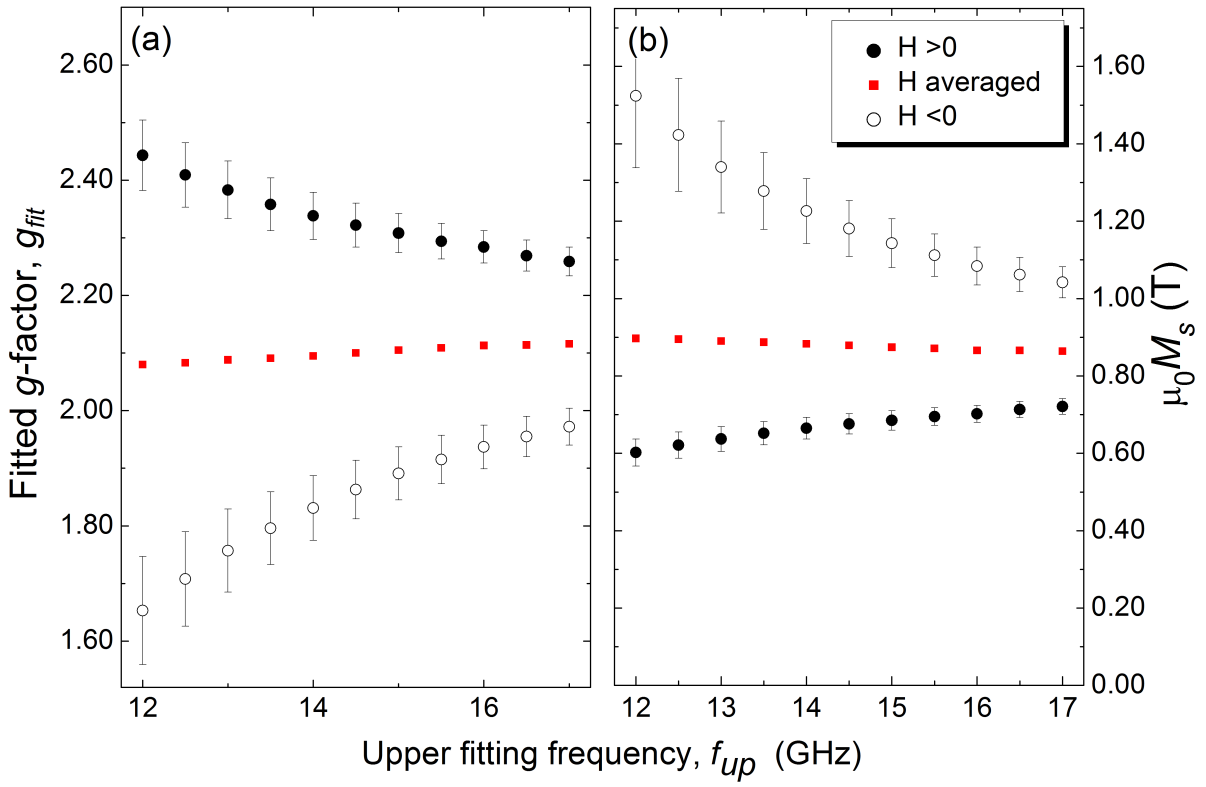

.

Figure 3.6: Fitted values of g (a) and $\mu_0 M_s$ (b) vs upper fitting frequency (f_{up}) for a 5 nm thick film of Ni_80Fe_20. The fits come from the resonance fields of 3 sets of data: the magnetic field pointing rightward (black circles), leftward (white circles) and the average of the two values (red squares)

of systematic error propagation in the results. This may be explained by the presence of in-plane anisotropy terms in the sample. Let's suppose that, for example there is uniaxial in-plane anisotropy in the sample and we apply the magnetic field along the easy axis, in such a case the Kittel equation should be

$$f = \frac{g\mu_B\mu_0}{h}\left[(H_{res} + H_u)\left(H_{res} + H_u + M_s\right)\right]^{1/2} \tag{3.13}$$

where H_u is in-plane anisotropy field. On the other side, let's suppose that we include the magnetic field shift as an extra fitting parameter in the non in-plane anisotropy, Kittel equation. We, then have

$$f = \frac{g\mu_B\mu_0}{h}\left[(H_{res} + \delta H_{res})\left(H_{res} + \delta H_{res} + M_s\right)\right]^{1/2} \tag{3.14}$$

The comparison between Eq. 3.14 with Eq. 3.13 makes clear that is impossible for the fitting routine to distinguish between the in-plane magnetic anisotropy and a negative shift in H_{res} , therefore it is evident that the effect of exclude in-plane anisotropy term in Eq. 3.2 will be the same to underestimate H_{res} by a constant magnitude H_u, i.e $\Delta H_{res} = -H_u$ when a sample has no in-plane anisotropy . Consequently, there will be a

decreasing underestimation of g and overestimation of M_s as more high frequency data is included, exactly in the same way of negative ΔH_{res} plotted in white circles on Fig. 3.2. These deviations are confirmed in the work of Shaw et al. [47]: g and M_s shows asymptotic behaviors when in-plane anisotropy terms are excluded from the Kittel equation. In the case of g (M_s) it approaches the true values from below (above) as more high frequency data is included. The work also shows that those asymptotic behaviors are largely spoiled when H_u is included in the Kittel equation, resulting in a further confirmation of our results.
In our case, our best estimation for the studied parameters are: g=2.13 ± 0.05, $\mu_0 M_s$=0.85 ± 0.01 T and $\mu_0 H_u$=0.51 ± 0.09 mT. These values were obtained applying the magnetic field along the easy axis, minimizing the magnetic field shift by the averaging methodology yet described, and fitting our data with Eq. 3.13 in all the range of frequencies (3-17GHz). The inability of the fitting routine to distinguish between a shift in the measured magnetic and in-plane anisotropy terms, also means that it is impossible to determine ΔH_{res} and H_u simultaneously, and thus at least one of the two parameters must be determined independently.

3.6 Summary

We have demonstrated theoretically and experimentally that for in-plane broadband FMR experiments, an unconsidered error in the measured value of the magnetic field of only a few Oersteds generates systematic and opposite sign deviations in the fitted values of spectroscopic g-factor (g) and the saturation magnetization (M_s) from their actual values. This difficults the determination of g and M_s with less than 1% precision in typical broadband FMR experiments. We also demonstrate that unconsidered in-plane anisotropy terms in the fittings have a comparable effect in the error propagation for those parameters.
The theoretical predictions were satisfactorily checked with simulated and real FMR data taken on a 5nm thickness $Ni_{80}Fe_{20}$ sample with a range frequencies from 3 to 17 GHz.
A simple method to minimize the error in the measured magnetic field, and thus the error propagation to g and M_s, was proposed. The method was successfully tested in the studied permalloy sample demonstrating that is possible to get high precision (less than 1%) values of both quantities using microwave excitation frequencies of only a few GHz. Our results also explain satisfactorily all the aspects of the article from Shaw et al. [47], regarding to the apparent dependence of g and M_s values on the range of frequencies used. It is also demonstrated that the asymptotic behavior of those quantities is a consequence of the decreasing f dependence of the systematic error propagation.
We believe our results will be useful to researchers interested in to measure accurate values of g and M_s using broadband FMR.

Chapter 4

Perpendicular magnetic anisotropy in CoFeB/Pd multilayers

4.1 Introduction

Materials with Perpendicular magnetic anisotropy (PMA) are promising candidates to form part of the next generation of data storage technologies. Recently, great interest in these materials has been aimed by their application as building blocks of the memory cells of the Spin Transfer Torque Magnetoresistive Random Access Memory (ST-MRAM). In this type of memory a bit of information is stored on the magnetic orientation of the free layer of a MTJ structure like the nanostructures already shown in chapters 1 and 2. The magnetic orientation of the free layer is read from changes in the TMR of the structure, and the switching of the magnetization is done by STT.
Out of plane anisotropy nanostructures offer many advantages respect to their in-plane anisotropy counterparts, like the lower switching currents, better thermal stability and better achievable areal density. The understanding of the physics behind the PMA is then a fundamental issue in the present days magnetism.
As stated in the introduction, PMA is of interfacial origin and appears in certain combinations of ferromagnetic and non-magnetic materials. In the study presented in this chapter, the ferromagnetic material is the $Co_{40}Fe_{40}B_{20}$, and the non-magnetic material is Pd. A systematic study of the variation of PMA intensity and the reversal of the magnetization in samples made of stacked repetitions of CoFeB/Pd bilayers is carried out. The parameters varied are the thickness of Pd, the thickness of the CoFeB and the number of repetitions of the bilayer structure.

4.2 Experimental methods

4.2.1 Samples fabrication

A series of thin films of Ta(20Å)/Pd(20Å)/$[Co_{40}Fe_{40}B_{20}(t_{CoFeB})$/Pd$(t_{Pd})]_n$/Pd(50Å) were deposited by DC magnetron sputtering on thermally oxidized Si(100) substrates. The base pressure of the chamber was better than 2×10^{-8}Torr and a working Ar pressure of 5×10^{-3} Torr was employed. The Ta(20Å)/Pd(20Å) bilayer serves as seed

layer whereas the Pd(50Å) is to prevent the oxidation. These layers are in all the set of samples, so in the following the will not be mentioned.
The parameters varied were the thickness of the CoFeB layer (t_{CoFeB}), the thickness of the Pd later (t_{Pd}), and the number of repetitions (n). Next is the list of the fabricated samples in each case:

- $[Co_{40}Fe_{40}B_{20}(t_{\mathrm{CoFeB}})/Pd(10Å)]_5$ with t_{CoFeB} = 2, 3, 4 and 5 Å.
- $[Co_{40}Fe_{40}B_{20}(3Å)/Pd(t_{\mathrm{Pd}})]_5$ with t_{Pd} = 2, 3, 4 and 5 Å.
- $[Co_{40}Fe_{40}B_{20}(t_{\mathrm{CoFeB}})/Pd(10Å)]_n$ with n = 5, 10, 15.

4.2.2 AGM measurements

The AGM measurements were carried out at room temperature using a commercial PMC MicroMag 2900 magnetometer. All the measurements presented in this chapter were carried out with the magnetic field applied out of plane. Results are shown in Fig. 4.1

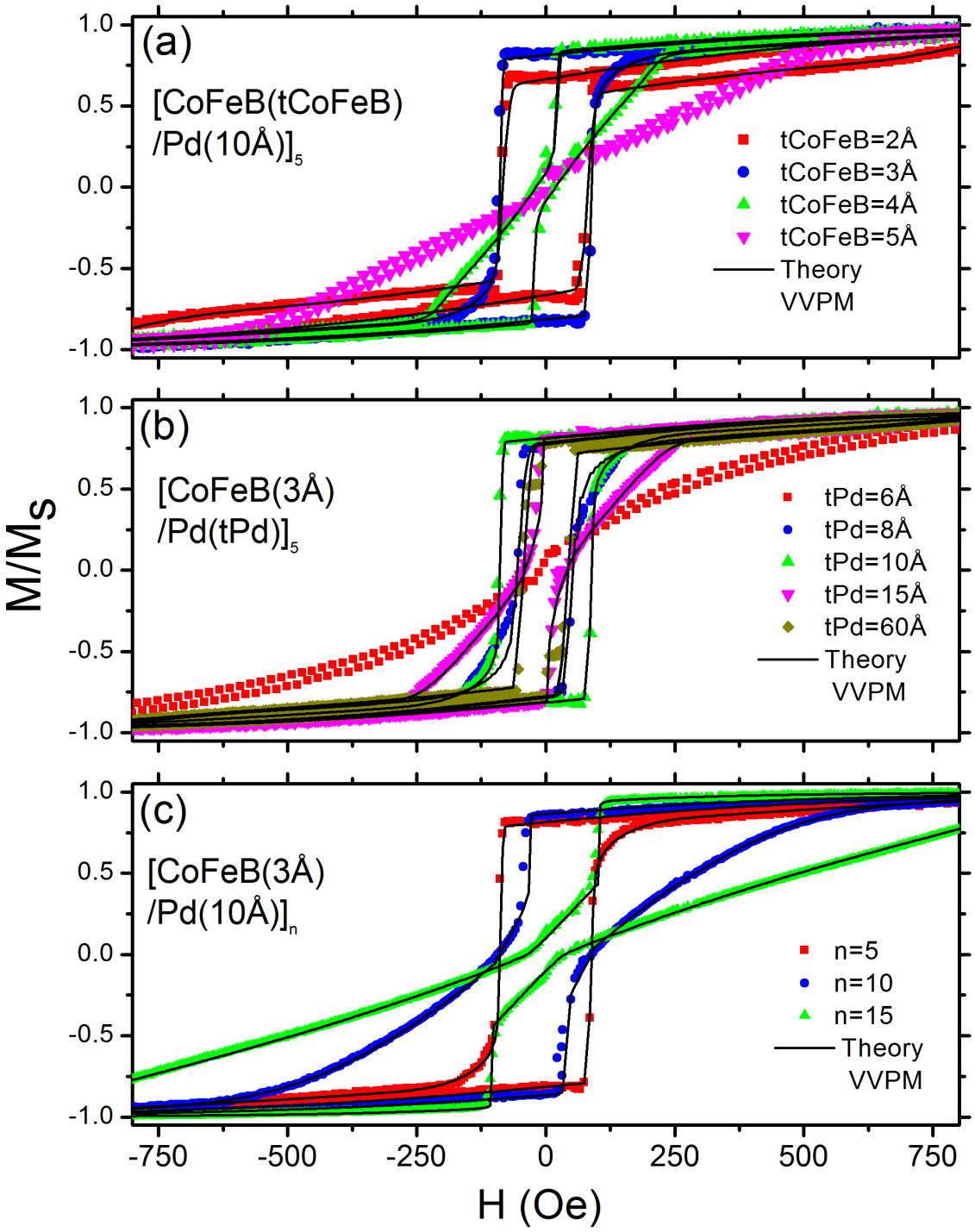

Figure 4.1: Out of plane hysteresis loops measured with AGM magnetometry and VVPM model predictions, for all the series of samples: (a) variable thickness of CoFeB, (b) variable thickness of Pd and (c) variable number of repetitions.

4.2.3 Kerr microscopy measurements

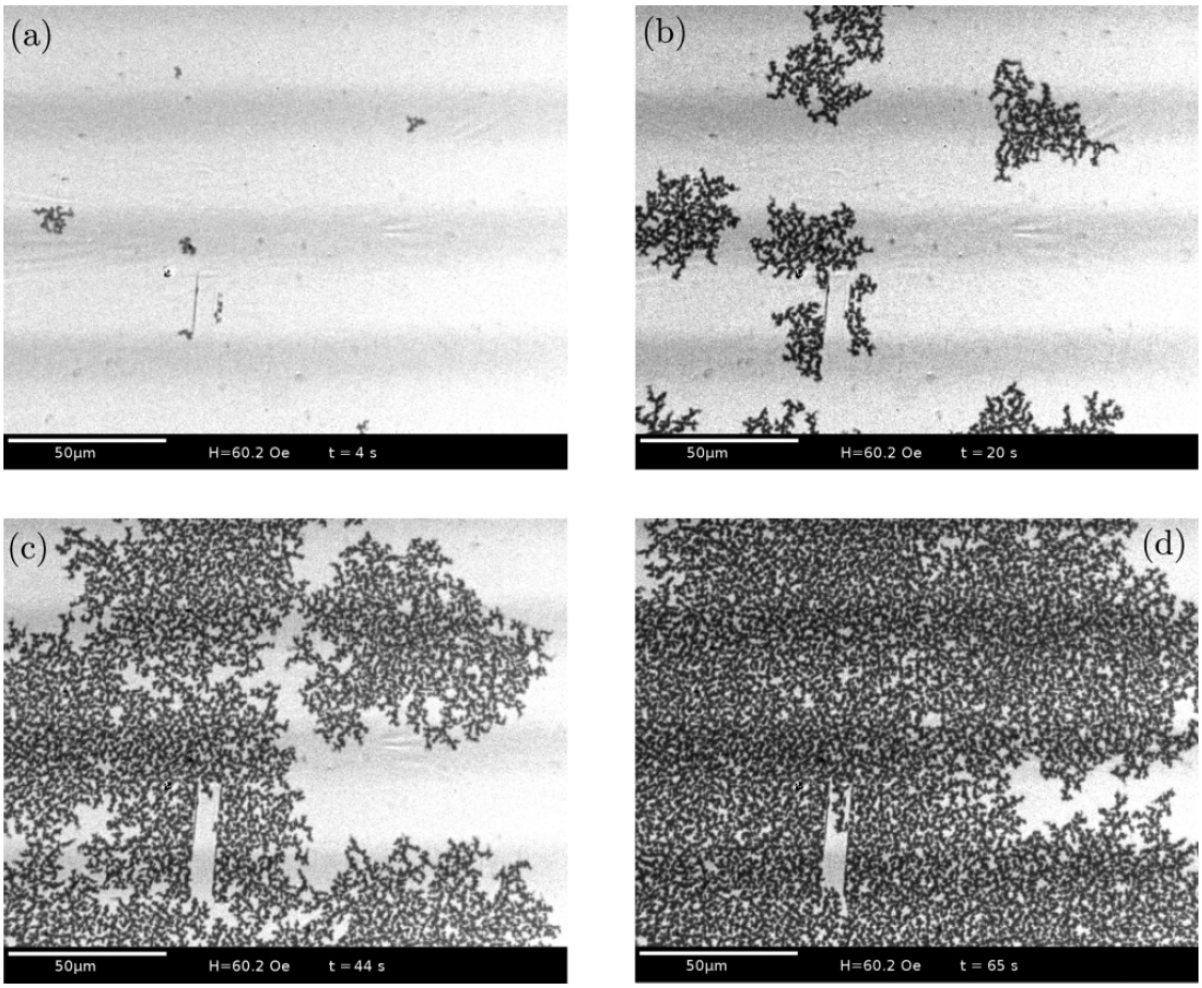

Figure 4.2: Kerr microscopy images of the evolution of labyrinth magnetic domains of the reversing $\left[\text{CoFeB(3Å)/Pd(10Å)}\right]_5$ sample for (a)t=4, (b) 20,(c) 44, and (d) 65s after the application of a perpendicular magnetic field. White and black zones indicate negative and positive saturation respectively.

Magnetic domain structure was imaged using a Evico Magnetics Kerr microscope with a highly stable and intense Xenon short arc light source. The instrument has an optical resolution down to 300nm and a maximum perpendicular magnetic field of 9200 Oe.

4.2.4 FMR measurements

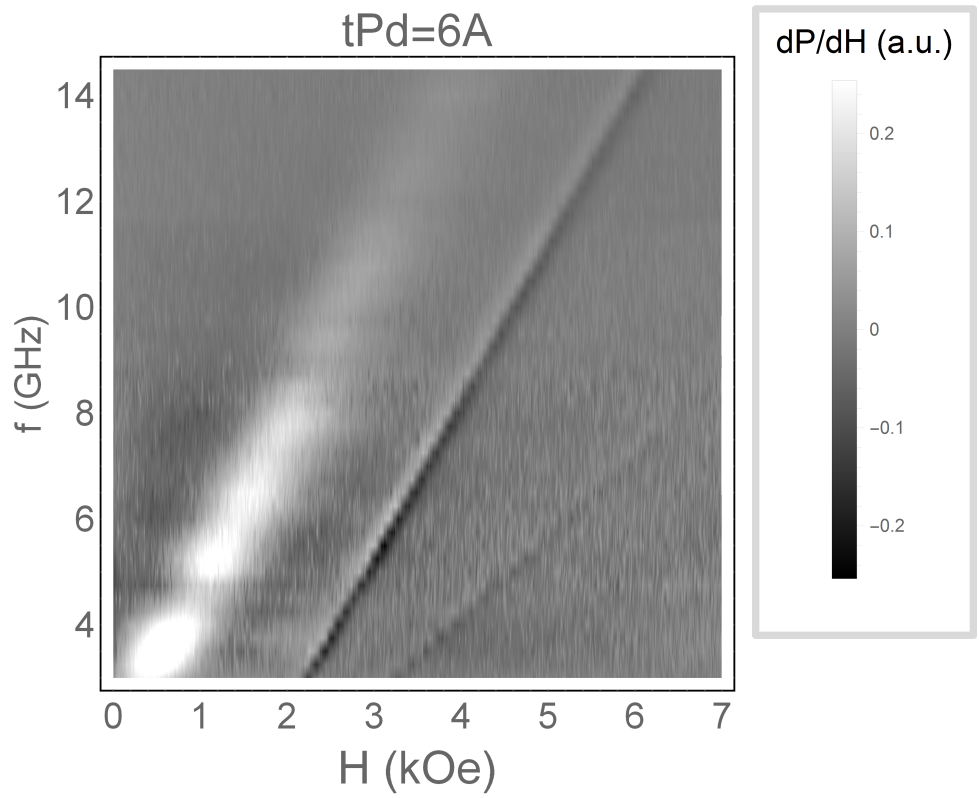

Figure 4.3: FMR spectrum for the $Co_{40}Fe_{40}B_{20}$(3Å)/Pd(6 Å)$]_5$ sample.

The measurements were carried out at the PhaseFMR spectrometer facility, using the same measurement procedures described in chapter 3. The only difference here, is that **H** was always applied perpendicular to the plane of the sample and the frequency steps smaller (every 0.1 GHz) in order to get more nice spectra. An illustrative example of the FMR spectra obtained in the set of studied samples is shown in Fig. 4.3. The resonant field vs frequency can be identified as the most intense and narrow line of the spectrum. Frequently, others and less intense secondary lines also appear (can be seen at the right inferior quadrant of the spectrum), due to the second harmonics emitted by the PhaseFMR device. These secondary peaks are not relevant for the current analysis. FMR peaks were fitted with the well known, out of plane, FMR formula:

$$f_{res} = \gamma' \left(H - M_{\text{eff}}\right)$$

where f_{res} is the resonance frequency $(\omega_R/2\pi)$, H_{res} is the resonant field. γ' and M_{eff} were left as free parameters. The results are shown in Fig. 4.4.

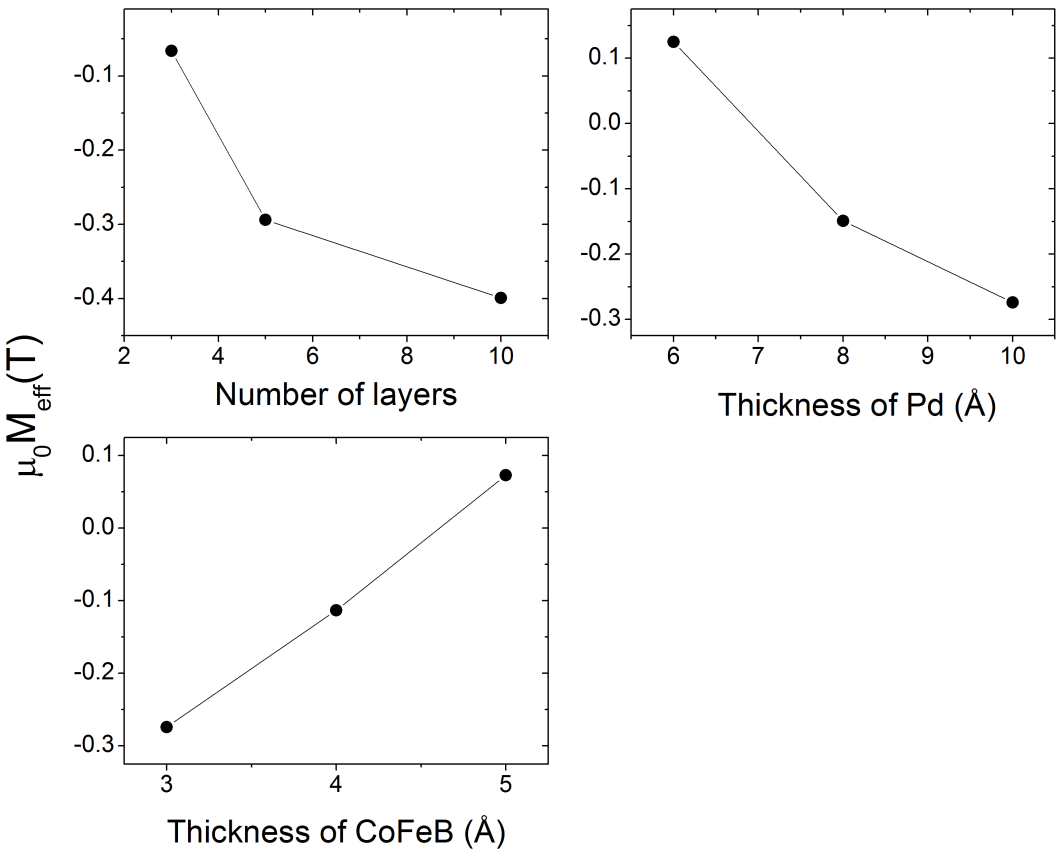

Figure 4.4: Fitted values of $\mu_0 M_{\text{eff}}$ vs: (a) number of repetitions, (b) thickness of Pd and (c) thickness of CoFeB, obtained from the FMR measurements:

4.3 Interpretation of the results

4.3.1 Preisach model

The hysteresis cycles obtained by the AGM measurements were fitted by the Preisach-type model of magnetic hysteresis. This model describes a magnetic body as were made up by an infinite set of elemental components called "hysterons". Each hysteron has a square hysteresis like the shown in Fig. 4.5 , so they can be only be in "up" or "down" state. The interaction field H_B and the coercive field H_C define the magnetic behavior of each hysteron and these parameters are assumed to follow some statistical distribution $p(H_B, H_C)$ among the hysterons, namely the Preisach distribution. The magnetization of the body for a certain value of H is the integration of the distribution of magnetic states from the hysterons for such magnetic field:

$$\frac{M}{M_s} = \int_0^{\infty} dH_C \left(\int_0^{b(H_C)} p(H_B, H_C)\, dH_B - \int_{b(H_C)}^{\infty} p(H_B, H_C)\, dH_B \right)$$

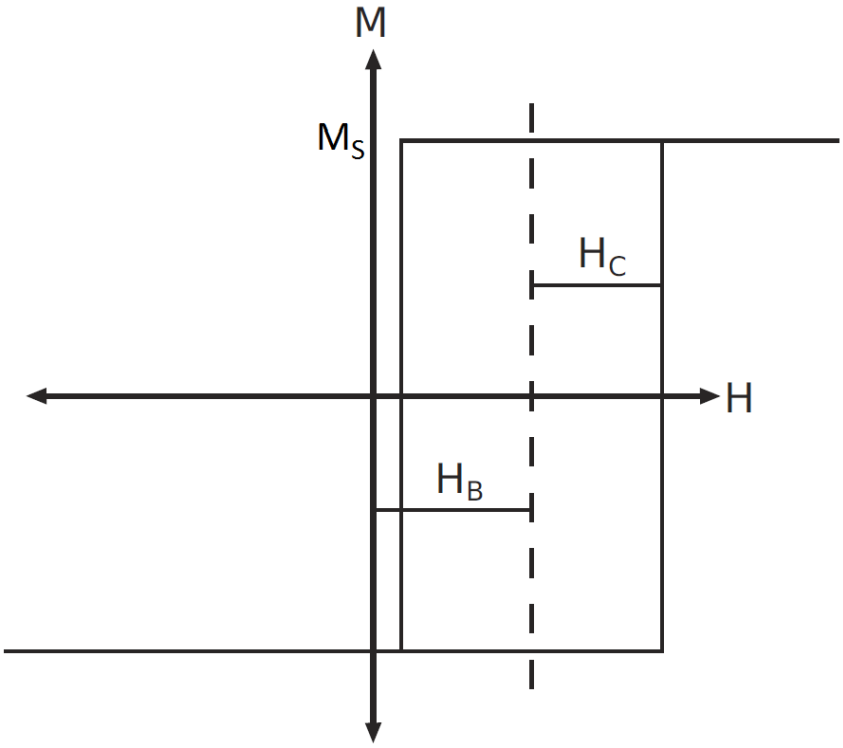

Figure 4.5: Hysteresis loop of an hysteron with interaction field H_B and coercive field H_C

where M_s is the magnetization of saturation, and:

$$b\left(H_C\right) = H \pm H_C.$$

where the $+$ and the $-$ signs stand for the up cycle and down cycle respectively. We assume that H_B and H_C are statistically independent, so the Preisach distribution is the product of the distributions of the coercive fields $f\left(H_C\right)$ and the distribution of the interaction fields $g\left(H_B\right)$.

$$p\left(H_B, H_C\right) = f\left(H_C\right) g\left(H_B\right).$$

In the classical Preisach model f and g follows well-known probabilistic distributions (gaussian for example). For the interpretation of or experiments we employed a variable variance Preisach model, in which the distributions of collectivities are given by:

$$f\left(H_C\right) = \frac{\left(1-p_d\right)}{\sqrt{2\pi}\sigma_C} \exp\left[-\frac{\left(H_C - \overline{H}_C\right)^2}{2\sigma_C^2}\right] + \frac{p_d}{\sqrt{2\pi}\sigma_D} \exp\left[-\frac{\left(H_C - \overline{H}_D\right)^2}{2\sigma_D^2}\right]$$

where H_C is the average of coercive fields and σ_C is its variance. Additionally Eq. above includes the effect of the defects within the samples. They have a proportion given by p_d, average coercive field $\overline{H}_D$ and variance σ_D. These defects may have been originated by the substrate roughness and the discontinuity of the CoFeB layers due to their thinness. On the other side, the distribution of interactions is given by:

$$g\left(H_B\right) = \frac{p_d}{\sqrt{2\pi}\sigma_B} \exp\left[-\frac{H_B^2}{2\sigma_B^2}\right]$$

We employed a variable variance Preisach model, in which the variance of is σ_B is given by:

$$\sigma_B = \sigma_a + \sigma_b |m|^k \tag{4.1}$$

The explicit functional dependence of σ_a, σ_b and k is given on Appendix A. In summary, they take specific values for each stage of the magnetization reversal. Here is a qualitative description of such stages listed sequentially as H increases:

- Small domains nucleate at random locations due to thermal stochastic magnetization reversal events.
- The above mentioned nucleation centers propagate in the form of labyrinth domains.
- The labyrinth domains propagate by the motion of domain walls.
- Finally the magnetization reversal is completed by the annihilation of the remaining labyrinth domains.

Fig. 4.2 shows the above mentioned sequence of mechanisms imaged by Kerr microscopy for the sample [CoFeB(3Å)/Pd(10Å)]$_5$. The external field was $H = 60.2$ Oe, applied to the previous negatively saturated sample.

4.3.2 FMR measurements

A.- CoFeB thickness

From Figs. 4.4 and 4.1 we can infer that the intensity of the PMA decreases with the CoFeB thickness. This is consistent with the fact that the PMA is an interfacial phenomenon. At this point is convenient to define the PMA energy density K_s:

$$K_s = \frac{\mu_0 M_s H_s}{2}$$

Where H_s is the PMA field already referred in the previous chapters. K_s follows the next relation with the thickness of the FM [50]:

$$K_s = K_b + \frac{K_i}{t_{\text{CoFeB}}} \tag{4.2}$$

where K_b are K_i the bulk and the interfacial of the PMA energy density, respectively. We can obtain the value of K_i by fitting the data with the formula:

$$M_{\text{eff}} = C_0 - \frac{C_1}{t_{\text{CoFeB}}}$$

where C_0 and C_1 are the fitting constants. Assuming a negligible contribution of K_b to K_s [50], we obtain M_s and K_i from:

$$\begin{aligned} M_s &= C_0 \\ K_i &= \frac{C_1}{t_{\text{CoFeB}}} \end{aligned}$$

The values obtained were $M_s = 4.5 \pm 0.6 \times 10^5$ A/m and $K_i = 5.7 \pm 1.4 \times 10^5$ J/m. Although the formula 4.2 does not take into account the variation of M_s with t_{CoFeB}, and the fitting was done with only 3 experimental points, the adjusted value of M_s must be quite realistic for the $t_{\mathrm{CoFeB}} = 4$Å . The later is confirmed in the work of Ngo el al. [51], which obtained a value of M_s ($\sim 4.5 \times 10^5$A/m) in CoFeB(4Å)/Pd(10Å) multilayers of similar characteristics. The obtained value K_i in the above mentioned work is quite larger than ours ($\sim 4.5 \times 10^5$A/m), however, this is given the extreme sensitivity of the PMA intensity on the fabrication conditions.

B.- Pd thickness

From Figs. 4.4 and 4.1 it can be seen an increase of the PMA with the Pd thickness in the range from 6 to 10Å. This has been attributed to the need of achieving a critical thickness of Pd to form PMA in the CoFeB/Pd interface. Our results show that the critical thickness of Pd to achieve net PMA is around 8 Å. After reach such critical thickness of Pd, the PMA increases with t_{Pd}, due to the improvement of the continuity of the CoFeB/Pd interface as more Pd is deposited.
The work of Ngo et al. [52] reports the opposite trend: PMA decreases with t_{Pd}. However, notice that the range of t_{Pd} for that study is from 10 to 60Å, thus not contradicting our results.
For $t_{\mathrm{Pd}} = 10$ Å we only account with the AGM measurements. Although, we can not quantify PMA from them, we may infer that the sample with t_{Pd}=15 Å has a PMA intensity comparable to the sample with t_{Pd}=10 Å, while for the t_{Pd}=60 Å PMA is undoubtedly smaller than for the sample with t_{Pd}=10 Å. Our results are in concordance with the ones reported by Ngo et al. [52] . We may infer from all these results, that there is an optimal value of t_{Pd} at which the PMA is maximum and decreases if t_{Pd} is above or below such value.
Unfortunately, the samples with $t_{\mathrm{Pd}} > 10$Å did not give measurable FMR signals that would have confirmed this hypothesis. This may be due to two reasons:

- For $t_{\mathrm{Pd}} = 15$Å, the PMA intensity is high enough to make $\mu_0 M_{\mathrm{eff}}$ fall out of the range of the spectrometer. Notice that the sample with $t_{\mathrm{Pd}} =$ 10Å is just on the detection limit of our FMR spectrometer ($\sim \mu_0 M_{\mathrm{eff}} = -0.4$T), so if the net PMA is slightly below that value, will not be measurable.

- For the sample with $t_{\mathrm{Pd}} = 60$ Å, the net PMA may be low enough to be detectable by our FMR spectrometer, however in this case the Pd layers are so thick that the increased damping arising from the spin sink effect of Pd extinguish the FMR signal [53, 54].

C.- Number of repetitions

We see an increment of the PMA with the number of repetitions. This behavior has also been reported recently in the work from Ngo et al. [51], also in CoFeB/Pd multilayers. We attribute this behavior to the lower intensity of the PMA of the bottom layer respect to the subsequent ones. The work of Ngo et al. [51] showed that the Ta seed layer promotes fcc structure on the adjoining Pd, while all the subsequent CoFeB layers

are amorphous. Thus, there is a difference between the value of the anisotropy constant of the bottom Pd/CoFeB interface K_s^b and the value for the rest of the interfaces: K_s. If $K_s^b < K_s$ the overall PMA intensity of the structure will increase with n, gradually approaching the limit value associated with K_s.
Currently, my group is working on a model that predicts the value of $\mu_0 M_{\text{eff}}$ from the values of K_b^s, K_b, the exchange coupling J_{EX} between the adjacent CoFeB layers and the number of repetitions. Preliminary results seems to be consistent with the experimental data. Despite this, the assumption that the PMA intensity is larger in amorphous than in structured materials deserves a more detailed analysis. This issue is very interesting from the physics point of view and new experiments must be carried out in order to get further insight about it.

4.4 Summary

A systematic study of the PMA intensity and magnetic hysteresis features have been carried out in CoFeB/Pd multilayers by means of alternating field gradient and Kerr magnetometry and broadband ferromagnetic resonance spectroscopy. The parameters varied were the thickness of both CoFeB and Pd layers as well as the number of repetitions.
Respect to the features of the hysteresis loops, a variable variance Preisach model been successful to fit the experimental curves and is consistent with a sequence of different magnetization reversal process during the reversal of the field. This was also observed by Kerr microscopy.
Respect to the PMA intensity, experimental results confirm that is of interfacial origin, demonstrated by its decreasing with the CoFeB thickness. Moreover it was found that there is a critical thickness of Pd for which net PMA appear ($\sim$ 8 Å).
More intriguing is the fact that PMA intensity increased with the number of repetitions. This has been attributed to the lower interfacial anisotropy of the first deposited CoFeB/Pd interface respect to the subsequently ones. A theoretical model that accounts this and the exchange coupling between the CoFeB layers seems to be consistent with the experimental data, however new experiments must be carried out to further validate this hypothesis.

Appendix A

Definition of the VVPM variances

Each stage follows the general expression given by and the continuity of σ_B is ensured for $-1 < m < 1$. Then σ_B is given by:

$$\sigma_B^u = \begin{cases} \sigma_a^L + \sigma_b^L m & m < m_{LW}, \\ \sigma_a^W + \sigma_b^W |m|^{0.1} & m_{LW} < m < m_{WA}, \\ \sigma_a^A + \sigma_b^A |m|^5 & m > m_{WA}, \end{cases}$$

for the up cycle, and:

$$\sigma_B^u = \begin{cases} \sigma_a^L + \sigma_b^L m & m < -m_{LW}, \\ \sigma_a^W + \sigma_b^W |m|^{0.1} & m_{LW} > m > -m_{WA}, \\ \sigma_a^A + \sigma_b^A |m|^5 & m < -m_{WA}, \end{cases}$$

for the down cycle. $\sigma_a^{L,W,A}$ and $\sigma_b^{L,W,A}$ are given by:

$$\begin{aligned} \sigma_a^L &= \sigma_0,\ \sigma_b^L = \sigma_1, \\ \sigma_a^W &= \sigma_0 + \sigma_1 m_{LW} - \sigma_1 s(m_{LW}) |m_{LW}|^{0.1} \Delta_u m_{LW}^{WA}, \\ \sigma_b^W &= \sigma_1 s(m) \Delta m_{LW}^{WA}, \\ \sigma_a^A &= \sigma_0 + \sigma_1 - \sigma_2 (m_{WA}) |m_{WA}|^5 \Delta_u m_{WA}^1, \\ \sigma_b^A &= \sigma_2 s(m) \Delta m_{WA}^1, \end{aligned}$$

with

$$\begin{aligned} \Delta m_{LW}^{WA} &= \frac{(1 - m_{LW})}{s(m_{WA}) |m_{WA}|^{0.1} - s(m_{LW}) |m_{LW}|^{0.1}} \\ \Delta m_{LW}^1 &= \frac{1}{1 - s(m_{WA}) |m_{LW}|^5}, \end{aligned}$$

where $s(x)$ is the sign function and the variances are:

$$\sigma_1 = \sigma_0 - \sigma_{st},\ \sigma_2 = -2\sigma_0 + \sigma_{st} + \sigma_{nd}.$$

Appendix B

DC magnetron sputtering

Sputtering is a physical vapor deposition method in which the particles of the material to deposit are ejected by momentum transfer in collisions with gas ions.
The experimental setup is depicted in figure B.1. The target of the material to be sputtered is located onto a plate (cathode) which contains a set of magnets arranged to maximize the intensity of the magnetic field close to the surface of the target. All of the above is inside a UHV vacuum chamber, which is pumped down to pressure levels around $\sim 10^{-}8$ Torr, and then filled with a noble gas, typically Ar at pressures in the order of mTorr. When the cathode is put at a negative voltage, a chain of processes starts to occur:

- B.1(a):the always present free electrons on the chamber accelerate away from the cathode and in the way the collide with the neutral Ar atoms.
- B.1(b): these collisions make the Ar atoms lose one of their outer shell electrons, turning them into positively charged Ar^+ ions. This process also leaves two available electrons to participate in new collisions, therefore a plasma of charged particles is formed above the target.
- B.1(c): the Ar^+ ions accelerate to the target and collide with it.
- B.1(d): neutral atoms of the target are ejected, following a straight path up to the first surface they encounter on their way or colliding with other Ar atoms. As result, many of the ejected atoms will go directly from the target to the substrate, forming the desired capping layer.

Additionally, some of the Ar^+ ions trap free electrons and emit a photon in the process B.1(e), generating the characteristic glow of the plasma. Notice that, in order that the process be efficient, the role of the magnetic field is fundamental: the electrons describe much larger trajectories than without it, increasing the time that the they are close to the target, and consequently the chances of the above described process be triggered.

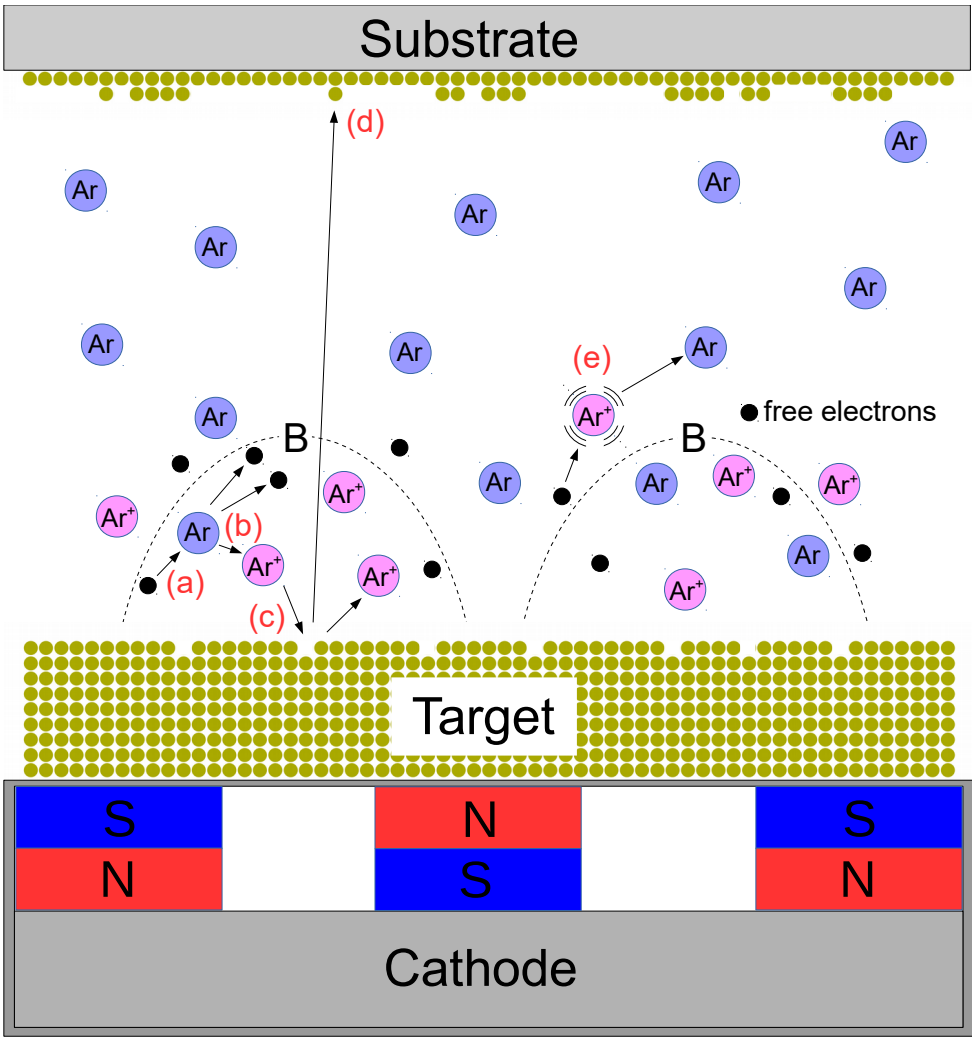

Figure B.1: Sketch of the magnetron sputtering deposition technique.

Appendix C

System for thermal evaporation of multilayers

Thermal evaporation is one of the simplest PVD deposition methods. The material to evaporate is heated in a vacuum chamber until the atoms on its surface get sufficient energy to leave it. Then, the material starts to irradiate such atoms and they travel in straight paths until they collide with another atoms or find a surface to settle down, like the wall of the chambers or the substrate were the sample is growth.
In order to avoid the atoms of the material to collide with other particles, the chamber must be at pressure levels low enough so that the mean free path for the atoms be fairly larger than the distance between the material and the substrate. This is typically achieved at 10^{-4} torr.
During the realization of my thesis I designed and built a system that permits to fabricate thin films of multilayers of different material by thermal deposition without break the vacuum.
The system is depicted in figure C.1. The whole system is pumped by a turbomolecular pump supported by a membrane pump. Typical final pressures after one night pump-down starting from atmosphere, are below 2×10^{-7} Torr.
Thermal evaporation is carried out on tungsten baskets connected to a DC power supply model 2260B-30-72, capable of deliver up to 72A at 720W. The two materials to evaporate is put directly on their respective tungsten baskets, which can be uncoated or coated with Al_2O_3 depending on whether the material form alloys with W during the evaporation or not. The current is raised up to the value at which the material begins to deposit on the substrate and then, the deposition rate is controlled by varying the value of the DC current.
The sample holder is fixed to a moving arm that can be moved forward and backward so that the substrate can be in the line of sight of one or other of the W baskets. Thickness is monitored with quartz micro-balances, conveniently located in places that are not obstructed by the sample holder during evaporation.
The sample holder is also a hot plate than permits to make in-situ annealing and depositions with variable substrate temperature. To accomplish this, the arm has a tunnel inside, which allows to drive 4 cables to the sample holder, two of them are for electrical feeding of the hot plate and the other two are for temperature measurement.
The system includes two right angle and two gate UHV valves, letting us open any of

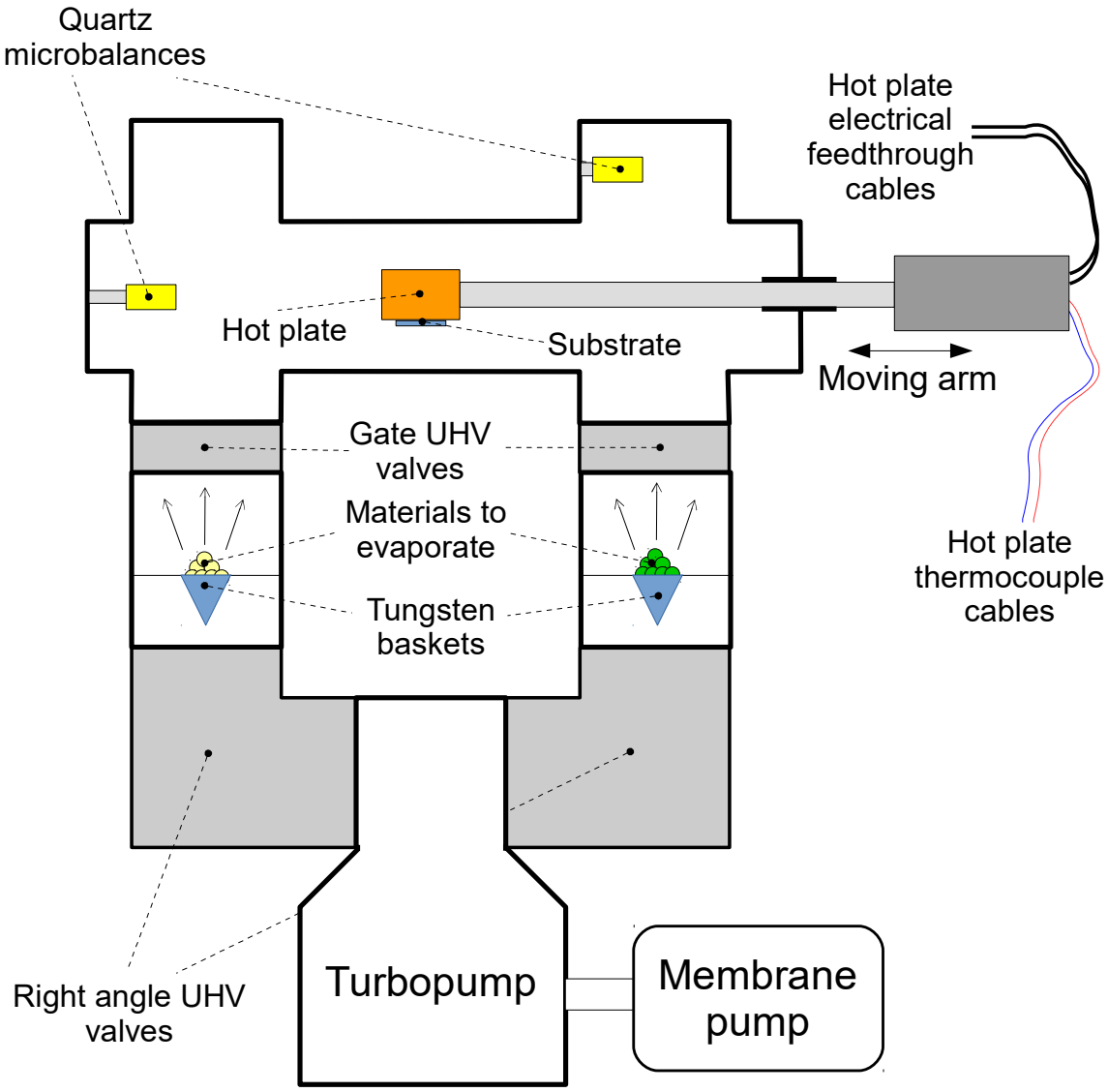

Figure C.1: Sketch of the 2-material thermal evaporation chamber built during my thesis.

the 3 sub-chambers (W basket 1, W basket 2 and moving arm) to the atmosphere without breaking the vacuum in the other 2. This allows to deposit more than 2 materials on a single substrate or also fabricate a set of samples without exposing the materials to atmosphere.
The system has been employed successfully to deposit Au/Cr bilayers on Mica with variable substrate temperature, which have been employed in studies of the electron scattering mechanisms on thin films. The possibility to fabricate Au/Cr bilayers, have opened the possibility to study the electron-surface scattering mechanisms in more detail, since these films reach the electrical percolation at lower thickness than the monolayers of Au.

Appendix D

Alternating field gradient magnetometry

Typical experimental set-up of an AGM is depicted in Fig. D.1. The sample is attached to the extreme of a semi-rigid bar, placed between the magnetic poles and subjected to two simultaneous and parallel magnetic fields: an uniform, continuous magnetic field generated by the electromagnet and an oscillating gradient magnetic field generated from a pair of coils attached to the poles of the electromagnet. The DC field magnetizes the sample, while the AC field generates an oscillating force on it, thus making the system bar- sample oscillate. The force is proportional to the total magnetic moment of the sample and hence to the amplitude of the oscillations of the bar, which are sensed at the other extreme by a piezoelectric sensor that transforms such movements into an electric voltage v_Ω.
The frequency of the oscillating magnetic field gradient is set to Ω, the natural mechanic frequency of oscillation of the system bar-sample, which is usually at few hundreds of Hz. At this condition, the system bar-sample enters in resonance, enhancing greatly the amplitude of the oscillations and thus improving the sensitivity of the magnetic moment. Furthermore, the voltage captured by the piezoelectric transducer is injected into a lock-in amplifier tuned to Ω , to further to increase the signal to noise ratio.
In case one wants to obtain absolute values of the magnetic moment, rather than simply proportional to it, a reference sample of known magnetic moment must be previously measured for calibration.

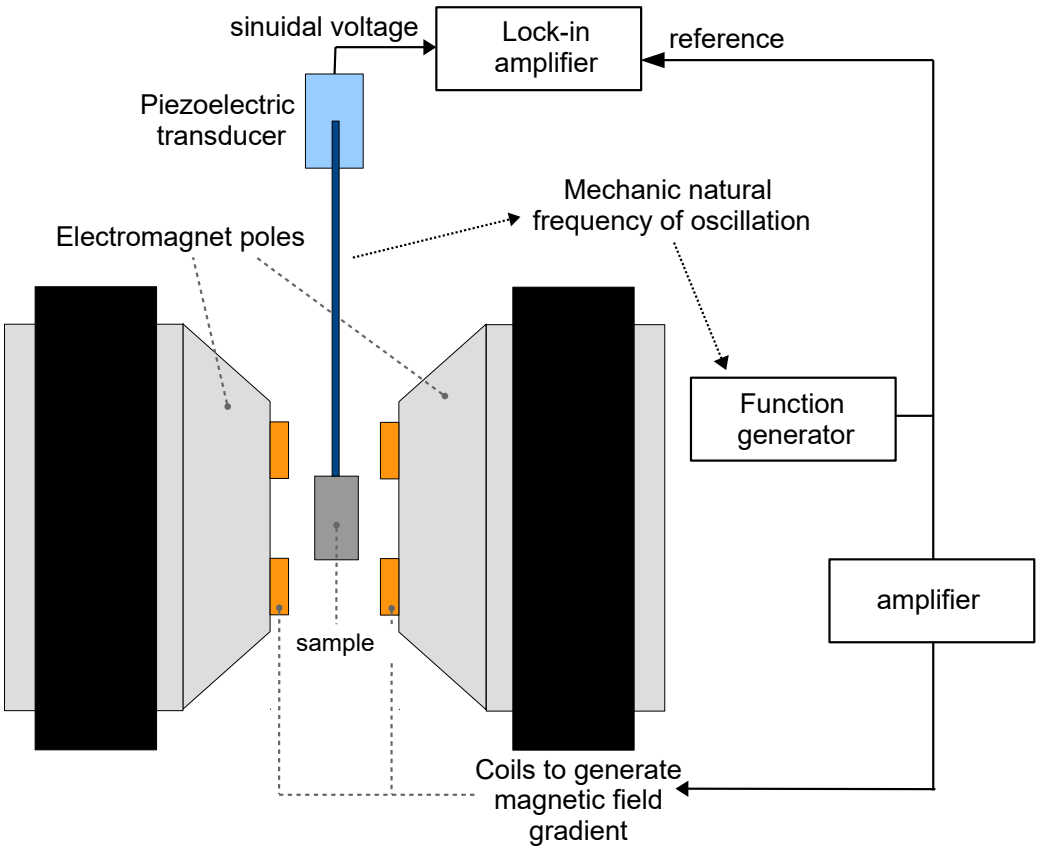

Figure D.1: Experimental setup of the alternating field gradient magnetometer.

Appendix E

Generalized magneto-optical ellipsometry

E.1 Introduction

Generalized magneto-optical ellipsometry (GME) [55] is a powerful, nondestructive technique that combines in a single experimental setup and sequence magneto-optical Kerr effect (MOKE) magnetometry and ellipsometry. It is therefore capable of determining by means of a single measurement sequence the complex index of refraction $N = n + ik$, the magneto-optical coupling constant $Q = Q_r + iQ_i$, as well as the magnetization orientation of a ferromagnetic material [56, 57].
It was also demonstrated that GME can be extended to variable wavelength and temperature dependent measurement types [58, 59]. Some recent works have furthermore improved the efficiency of data acquisition [60]. and used GME to characterize purely optical anisotropy effects [61].
It is known that the sensitivity of a conventional, non-magneto-optical ellipsometer is in general better for higher incidence angles [62] (as measured from the sample normal), with recommended angles being typically larger than 40°. Until now, no significant attention has been given to the incidence angle of the light in GME experiments, which could affect the precision and accuracy of results in a significant way.
In this work we present a thorough study of error propagation for N and Q at different incidence angles of the light φ_0 and we compare these theoretical results with GME measurements on polycrystalline cobalt films for different values of φ_0 .

E.2 Theory

For simplicity, we restrict our analysis here to the assumption of a bulk material, that is optically isotropic and has isotropic magneto-optical response in that it can be described by a single magneto-optical coupling constant Q. The light used in the GME experiment is assumed to be a fully polarized plane wave. The electric field of such a light wave can be expressed as the superposition of components that are perpendicular and parallel to the plane of incidence, as shown in Fig. E.1.

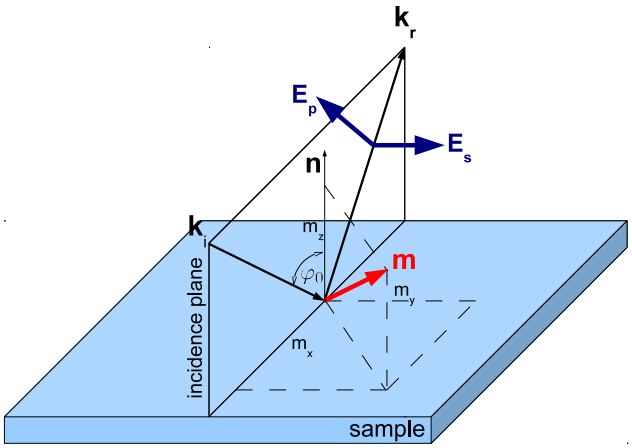

Figure E.1: Reflection of light at the surface of a magnetized medium with arbitrary direction of the magnetization. **m** represents the unit vector of the magnetization. **n** is vector normal to plane and lies in POI. m_x, m_y, m_z are the longitudinal, longitudinal and polar components of **m** respectively

$$\mathbf{E} = \begin{pmatrix} \mathbf{E}_s \\ \mathbf{E}_p \end{pmatrix}. \tag{E.1}$$

The surface acts as a transformation matrix

$$\mathbf{R} = \begin{pmatrix} r_{ss} & r_{sp} \\ r_{ps} & r_{pp} \end{pmatrix} \tag{E.2}$$

for the incoming beam. The diagonal components of **R**, r_{ss} and r_{pp} are the conventional, nonmagnetic reflection coefficients of the perpendicular and parallel components, respectively, i. e. the Fresnel reflection coefficients, which are known to follow [63]

$$\widetilde{r}_s = \frac{r_{ss}}{r_{pp}} = -\frac{\cos(\varphi_0 - \varphi_1)}{\cos(\varphi_0 + \varphi_1)}, \tag{E.3}$$

with

$$\tan(\varphi_1) = \cot(\varphi_0)\left(\frac{\widetilde{r}_s + 1}{\widetilde{r}_s - 1}\right), \tag{E.4}$$

where φ_1 is the complex angle of refraction. The non-diagonal components of matrix **R** are terms that appear if the sample material is magnetized. In the case studied here, we restrict ourselves to magnetization orientations along the longitudinal axis only, so that

$$\mathbf{R} = r_{pp}\begin{pmatrix} \widetilde{r}_s & \widetilde{\alpha} \\ -\widetilde{\alpha} & 1 \end{pmatrix} \tag{E.5}$$

with[57]

$$\widetilde{\alpha} = -\frac{ibQ\sin(2\varphi_0)\sin^2(\varphi_1)}{\sin(\varphi_0 + \varphi_1)\cos(\varphi_1)\left[\sin(2\varphi_0) - \sin(2\varphi_1)\right]} \tag{E.6}$$

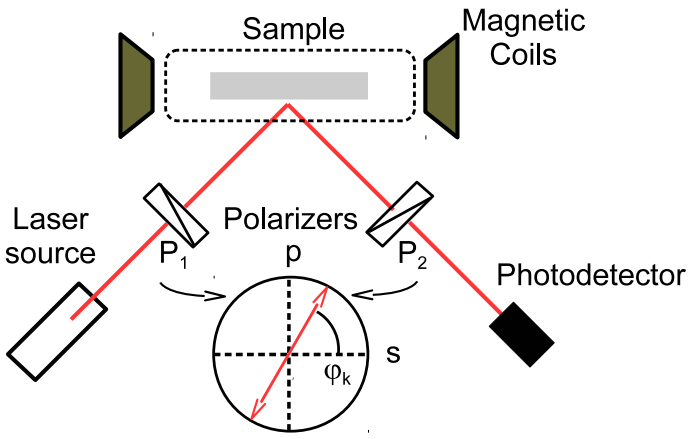

Figure E.2: Scheme of the GME setup

for a bulk like sample, where Q is defined via the dielectric tensor

$$\varepsilon = \varepsilon_r \begin{pmatrix} 1 & 0 & 0 \\ 0 & 1 & 0 \\ 0 & 0 & 1 \end{pmatrix} + iQ\varepsilon_r \begin{pmatrix} 0 & m_z & -m_y \\ -m_z & 0 & m_x \\ m_y & -m_x & 0 \end{pmatrix}, \tag{E.7}$$

with ϵ_r being the permittivity of the medium in the absence of magnetization. For a GME set-up like the one shown[60] in Fig. E.2, the polarizers are described by the transformation matrix

$$\mathbf{P} = \begin{pmatrix} \cos^2(\theta) & \sin(\theta)\cos(\theta) \\ \sin(\theta)\cos(\theta) & \sin^2(\theta) \end{pmatrix} \tag{E.8}$$

acting upon the incoming electric field vector. Hereby, θ is the angle between the polarizer transmission axis and the s-polarization orientation. The electric field vector $\mathbf{E}_D$ arriving at the photodetector is then given by

$$\mathbf{E}_D = \mathbf{P}(\theta_2) \cdot \mathbf{R} \cdot \mathbf{P}(\theta_1) \cdot \mathbf{E}_0, \tag{E.9}$$

with $\mathbf{E}_0$ being the electric light field produced by the laser. Correspondingly, the intensity of the light at the photodetector is

$$I_D = \mathbf{E}_D \cdot \mathbf{E}_D^*. \tag{E.10}$$

The analysis of light intensity changes at the detector upon magnetization state inversion, while varying the angles of the polarizers θ_1 and θ_2 , enables now the determination of $\mathbf{R}$, which in turn allows for the extraction of N and Q, in both their real and imaginary parts. We define here the fractional intensity change

$$\frac{\delta I}{I}(\theta_1, \theta_2) = 2\frac{I_\uparrow - I_\downarrow}{I_\uparrow + I_\downarrow}, \tag{E.11}$$

where $I_\uparrow$ and $I_\downarrow$ are the light intensities for inverted magnetization states of the sample. It has been shown[55] that

$$\frac{\delta I}{I} = \frac{B_1 f_1 + B_2 f_2}{B_5 f_5 + 2B_6 f_4 + f_3} \tag{E.12}$$

with

$$\begin{aligned} B_1 &= \Re\left(\widetilde{\alpha}\right), \\ B_2 &= \Re\left(\widetilde{r_s}\alpha^*\right), \\ B_5 &= \left|\widetilde{r_s}\right|^2, \\ B_6 &= \Re\left(\widetilde{r_s}\right) \end{aligned} \tag{E.13}$$

and[1]

$$\begin{aligned} f_1 &= \sin\theta_2 \cos\theta_2 \sin^2\theta_1 - \sin\theta_1 \cos\theta_1 \sin^2\theta_2, \\ f_2 &= \sin\theta_1 \cos\theta_1 \cos^2\theta_2 - \sin\theta_2 \cos\theta_2 \sin^2\theta_1, \\ f_3 &= \sin^2\theta_1 \sin^2\theta_2, \\ f_4 &= \sin\theta_1 \cos\theta_1 \sin\theta_2 \cos\theta_2, \\ f_5 &= \cos^2\theta_1 \cos^2\theta_2. \end{aligned} \tag{E.14}$$

From Eq. (13) we obtain

$$\widetilde{r_s} = B_6 + i\sqrt{B_5 - B_6^2} \tag{E.15}$$

The relation between r_s and the index of refraction is given by[63]

$$\widetilde{r_s} = \frac{\sin^2\left(\varphi_0\right) + \cos\left(\varphi_0\right)\sqrt{N^2 - \sin^2\left(\varphi_0\right)}}{\sin^2\left(\varphi_0\right) - \cos\left(\varphi_0\right)\sqrt{N^2 - \sin^2\left(\varphi_0\right)}}. \tag{E.16}$$

Thus we obtain

$$\begin{aligned} N = \tan(\varphi_0) \Bigg(& 2\left(B_5 + i\sqrt{B_5 - B_6^2}\right)\cos(2\varphi_0) \\ & + 1 + \left(B_5 + i\sqrt{B_5 - B_6^2}\right)^2\Bigg)^{1/2} \\ & \times \left(i\sqrt{B_5 - B_6^2} + B_5 + 1\right)^{-1}. \end{aligned} \tag{E.17}$$

We derive an expression for Q as a function of B_i by replacing Eqs. (E.4), (E.13) and (E.15) in Eq. (E.6). We find

$$Q = i\left(B_1 + \frac{i\left(B_2 - B_1 B_6\right)}{\sqrt{B_5 - B_6^2}}\right) q_0 \tag{E.18}$$

[1] If the orientation of magnetization is arbitrary, the numerator in right part of Eq. (E.12) will have four additional terms describing the transversal and polar components of magnetization[59]

with

$$
\begin{aligned}
q_0 = \tan(\varphi_0)\sec(\varphi_0)&\frac{\left(i\sqrt{B_5 - B_6^2} + B_5 - 1\right)}{\left(i\sqrt{B_5 - B_6^2} + B_5 + 1\right)^2} \\
&\times \left(2\left(1 + \left(B_5 + i\sqrt{B_5 - B_6^2}\right)^2\right)\cos(2\varphi_0)\right. \\
&\left. + \left(B_5 + i\sqrt{B_5 - B_6^2}\right)\left(\cos(4\varphi_0) + 3\right)\right) \\
&\times \left(2\left(B_5 + i\sqrt{B_5 - B_6^2}\right)\cos(2\varphi_0)\right. \\
&\left. + \left(B_5 + i\sqrt{B_5 - B_6^2}\right)^2 + 1\right)^{-1}.
\end{aligned} \tag{E.19}
$$

E.3 Error Analysis

E.3.1 Error propagation for the refractive index N

Using Eqs. (E.15) and (E.16) we derive the error propagation from the measured $B_{5,6}$ values to the analyzed

$$
\begin{aligned}
\frac{\partial N}{\partial B_5} &= g_n g_5, \\
\frac{\partial N}{\partial B_6} &= g_n g_6
\end{aligned} \tag{E.20}
$$

with

$$
\begin{aligned}
g_n &= \frac{\sqrt{N^2 - \sin^2(\varphi_0)}}{2N\cos\varphi_0} \\
&\quad \times \left(\sin\varphi_0 - \cot\varphi_0\sqrt{N^2 - \sin^2(\varphi_0)}\right)^2, \\
g_5 &= \frac{1}{2\sqrt{B_5 - B_6^2}}, \\
g_6 &= 1 - \frac{B_6}{2\sqrt{B_5 - B_6^2}}.
\end{aligned} \tag{E.21}
$$

N is given in terms of $B_{5,6}$ by Eq. (E.17). The total variance in N is then

$$
\Delta N = \sqrt{\left(\frac{\partial N}{\partial B_5}\Delta B_5\right)^2 + \left(\frac{\partial N}{\partial B_6}\Delta B_6\right)^2}, \tag{E.22}
$$

where $\Delta B_{5,6}$ are the corresponding variances in each of the experimentally accessible B_i-factors. As a way to sketch the variance amplification from $B_{5,6}$ to N as function of

incidence angle, . Fig. E.3a shows the variance in N assuming a 1% variance of $B_{5,6}$ each, which are reasonable values based upon our exemplary experimental study of Co. As is evident from Fig. E.3a, all curves show a very pronounced growth of the variance as φ_0 decreases.

E.3.2 Error propagation for the magneto-optical constant Q

Using Eqs. (E.18) and (E.19) we derive the error propagation of the measured $B_{1,2,5,6}$ values to the analyzed magneto-optical coupling constant Q. Here, we find

$$\begin{aligned}
\frac{\partial Q}{\partial B_5} &= q_s g_5 + q_5 q_0, \\
\frac{\partial Q}{\partial B_6} &= q_s g_6 + q_6 q_0, \\
\frac{\partial Q}{\partial B_1} &= q_1 q_0, \\
\frac{\partial Q}{\partial B_2} &= q_2 q_0
\end{aligned} \tag{E.23}$$

with

$$\begin{aligned}
q_s = & \\
& \Big((\widetilde{r_s} - 3) \left((\widetilde{r_s} - 1)^4 \tan(\varphi_0) \sec(\varphi_0) - \widetilde{r_s}^{\,2} \sin(5\varphi_0) \right) \\
& + (\widetilde{r_s}(\widetilde{r_s}(\widetilde{r_s}(-2(\widetilde{r_s} - 6)\widetilde{r_s} - 43) + 63) - 29) + 3) \sin(\varphi_0) \\
& + (\widetilde{r_s}(9 - 2\widetilde{r_s}((\widetilde{r_s} - 6)\widetilde{r_s} + 7)) + 1) \sin(3\varphi_0) \Big) \\
& \times 2 \left((\widetilde{r_s} + 1)^3 \left(\widetilde{r_s}^{\,2} + 2\widetilde{r_s} \cos(2\varphi_0) + 1 \right)^2 \right)^{-1}, \\
q_1 = & \; i + \frac{B_6}{\sqrt{B_5 - B_6^2}}, \\
q_2 = & \; \frac{-1}{\sqrt{B_5 - B_6^2}}, \\
q_5 = & \; \frac{B_2 - B_1 B_6}{2 \left(B_5 - B_6^2 \right)^{3/2}}, \\
q_6 = & \; \frac{B_1 B_5 - B_2 B_6}{\left(B_5 - B_6^2 \right)^{3/2}}.
\end{aligned} \tag{E.24}$$

The total variance in Q is correspondingly given by

$$\begin{aligned}
\Delta Q = \Bigg(& \left(\frac{\partial Q}{\partial B_1} \Delta B_1 \right)^2 + \left(\frac{\partial Q}{\partial B_2} \Delta B_2 \right)^2 \\
& + \left(\frac{\partial Q}{\partial B_5} \Delta B_5 \right)^2 + \left(\frac{\partial Q}{\partial B_6} \Delta B_6 \right)^2 \Bigg)^{1/2}
\end{aligned} \tag{E.25}$$

with $B_{1,2,5,6}$ being the variances of each of the GME parameters B_i. Fig. E.3b shows the variance in Q as function of incidence angle, assuming a constant variance of 1 % for all coefficients $B_{1,2,5,6}$. Again there is a very strong growth in variance as the incidence angle decreases. An analysis of each individual term contributing to the sum under the square root in Eq. (E.25) (not showed here) shows that the main contributions to Q are the two terms with $B_{5,6}$, namely the GME parameters related to the conventional Fresnel coefficients, which are not related to magneto-optical activity.

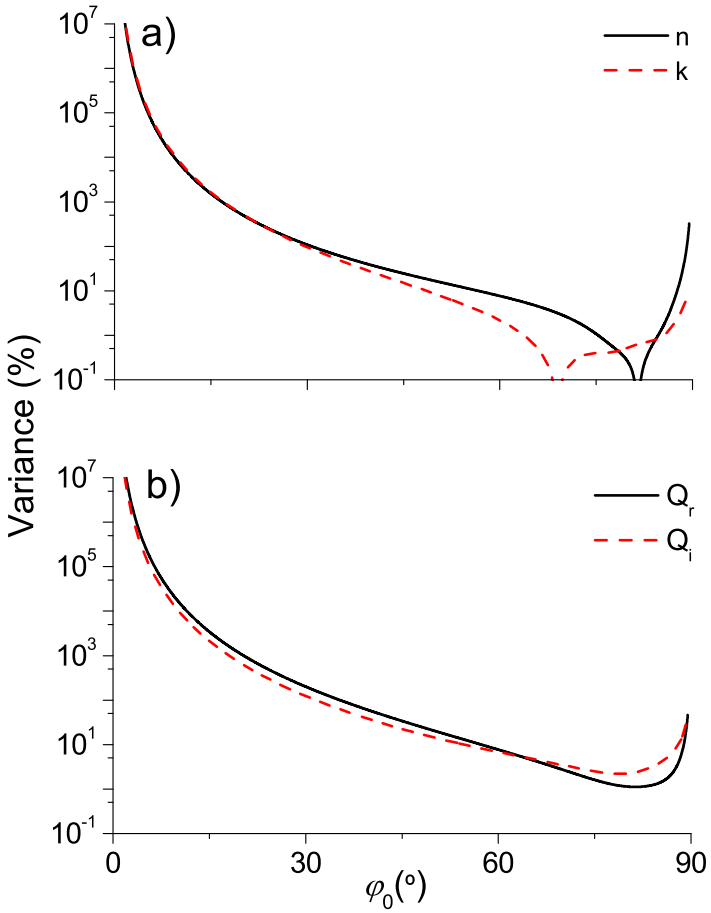

Figure E.3: Variance of the complex index of refraction N (a), and the complex magneto-optical constant Q (b) as a function of the angle of incidence. The specific values used for this calculation are $n = 2.20$, $k = 3.42$, $Q_r = 2.25 \times 10^{-2}$ and $Q_i = 0.80 \times 10^{-2}$, which are typical values for Co.

E.4 Meassurements and Discussion

In order to test our theoretical results, we performed measurements on a 150 nm thick cobalt film in longitudinal geometry for four distinct values of φ_0: 15°, 30°, 45° and 60°. As a light source, we used a polarization stabilized He-Ne laser (λ=633nm). We

measured the experimental $\delta I/I$ values following the work of Arregi et al [60] using a diagonal grid of (θ_1, θ_2)-pairs around the light extinction condition. The intensities of the light $I_\uparrow$ and $I_\downarrow$, were taken at the largest experimentally accessible magnetic field values (approx. +/- 2500 Oe) in order to saturate the magnetization in the longitudinal direction. We repeated this grid of measurements at least 20 times for each of the four φ_0 values and analyzed all experimental data by least-squares fitting of the $\delta I/I$ maps to Eq. (E.12). From the collection of these multiple data sets, we then obtained the averages and variances of the fitting constants B_1,B_2, B_5, and B_6. The corresponding results are shown in Table E.1. Table E.2 lists the average and the variance of the

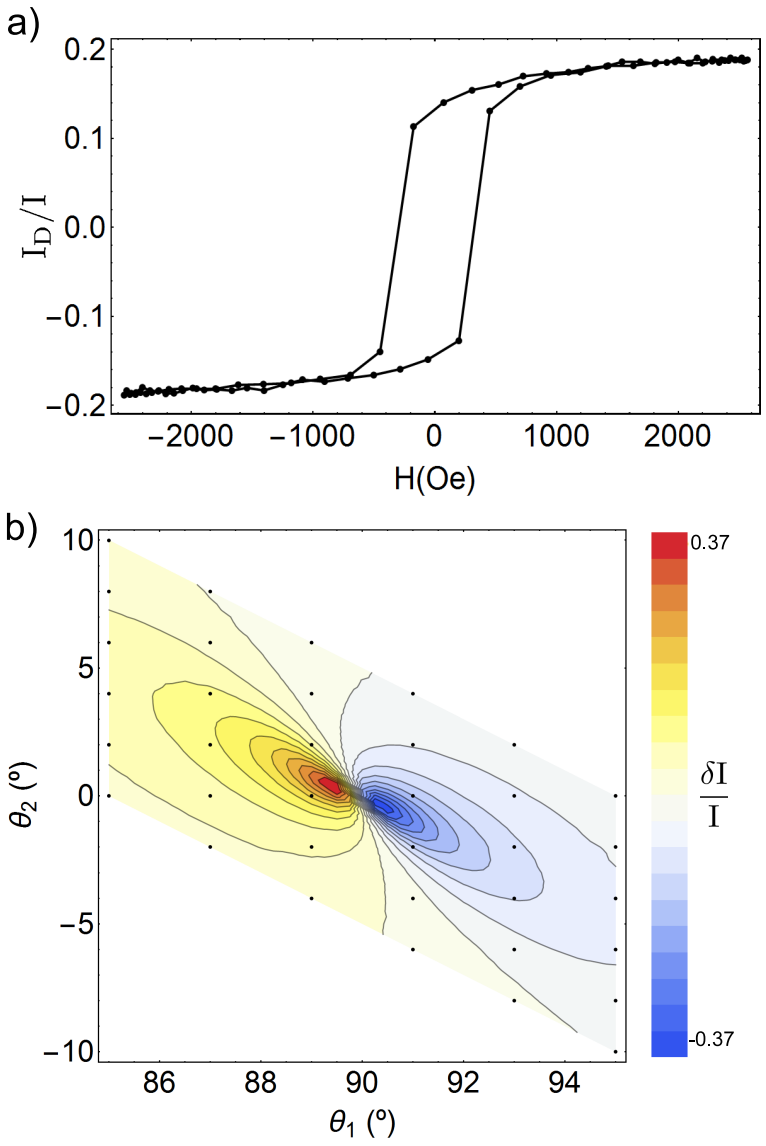

Figure E.4: (a) Hysteresis loop for a fixed set of polarizer angles θ_1, θ_2. The field dependent light intensity is normalized to $I = (I_\uparrow + I_\downarrow)/2$. (b) Color-coded $\delta I/I(\theta_1, \theta_2)$-plot for experimental data obtained at φ_0=60° via hysteresis cycles such as the one shown as in (a). The grid of black points shows the polarizer pair orientations, for which the repeat measurements were done to perform the statistical data analysis of Table E.1

complex index of refraction and magneto-optical constant Q for each angle of incidence, derived from the fitted GME parameters.
In Table E.1 we see that the uncertainty for the $B_{5,6}$ values is roughly the same for both parameters independent from the incidence angle φ_0. However, in Table E.2 we observe that the uncertainty for the optical and magneto-optical constants becomes significantly lower as φ_0 increases. At φ_0=15°, the error propagation is actually so problematic that even small statistical errors cause a complete lack of reliability for the deduced optical and magneto-optical constants.
On the other side, the uncertainly in the $B_{1,2}$ parameters has acceptable variances even for the 15° incidence angle. This means that at 15° it is still possible to measure hysteresis cycles with good statistics. However, the measurements are not suitable for the determination of Q, in exactly the same way, in which they are not suitable for the determination of N anymore. This is because B_5 and B_6 already produce such large inaccuracies in Q, that its measurement becomes meaningless. We expect very similar results for materials with comparable values of N, such as for example bulk permalloy [55] ($N = 2.4 + 3.7i$; $Q = (7.3 + 7.8i) \times 10^{-3}$), even if Q differs significantly, because the variances of $B_{1,2}$ do not make an important contribution to the uncertainty of Q, which is dominated by the constants $B_{5,6}$. So, we can conclude that in general the accuracy of magneto-optical constant measurements decreases as φ_0 becomes smaller.

Table E.1: Fit parameters $B_{1,2}$ and $B_{7,8}$ of experimental $\delta I/I$ data sets, at each value of φ_0.

	$\varphi_0 = 15°$	$\varphi_0 = 30°$	$\varphi_0 = 45°$	$\varphi_0 = 60°$
$B_1(10^{-4})$	-2.400±4.5%	-4.372±1.4%	-5.621 ± 1.4%	-4.588 ± 2.6%
$B_2(10^{-4})$	2.517±4.7%	5.310±1.5%	9.031 ± 1.5%	16.05 ± 1.5%
B_5	1.035±1.1%	1.153±0.3%	1.395 ± 0.7%	2.019 ± 0.8%
B_6	-1.016±0.5%	-1.066±0.2%	-1.140 ± 0.3%	-1.15 ± 0.3%
R^2	0.998	0.998	0.999	1.000

Table E.2: Material constants derived from Table E.1.

	$\varphi_0 = 15°$	$\varphi_0 = 30°$	$\varphi_0 = 45°$	$\varphi_0 = 60°$
n	0.950 ± 46%	2.233 ± 3.3%	2.203 ± 1.1%	2.203 ± 1.5%
k	2.568 ±9.9%	3.587 ± 2.1%	3.364 ± 1.4%	3.423 ± 1.0%
$Q_r\,(10^{-2})$	0.876 ± 33%	2.317 ± 3.6%	2.176 ± 1.8%	2.249 ±1.3%
$Q_i\,(10^{-2})$	0.262 ± 120%	-0.703 ± 12%	-0.791 ± 4.0%	-0.804 ±3.8%

Summary

In this study, we have demonstrated that the light incidence angle affects the GME measurement precision for the complex index of refraction N and magneto-optical

constant Q in a very significant way, similar to the case of conventional ellipsometry of nonmagnetic material. If GME-data are used for simple Kerr magnetometry and not for the purpose of complex magneto-optical constant determination, this incidence angle sensitivity still exists, but is far less crucial, because no data interpretation based on the diagonal reflection matrix elements is being done in this case.
In our experimental study of cobalt, GME gives especially reliable results at light incidence angles of 45° and 60°, while it becomes clearly impracticable for the determination of optical and magneto-optical constants at 15° and below. Thus, we find the light incidence angle to be very relevant, so that it must be taken in consideration for the design of optimized measurement strategies for optical and magneto-optical constants by means of GME.

Bibliography

[1]M. N. Baibich, J. M. Broto, A. Fert, F. N. Van Dau, F. Petroff, P. Etienne, G. Creuzet, A. Friederich, and J. Chazelas, "Giant magnetoresistance of (001)fe/(001)cr magnetic superlattices", Phys. Rev. Lett. **61**, 2472–2475 (1988).

[2]G. Binasch, P. Grünberg, F. Saurenbach, and W. Zinn, "Enhanced magnetoresistance in layered magnetic structures with antiferromagnetic interlayer exchange", Phys. Rev. B **39**, 4828–4830 (1989).

[3]J. Slonczewski, "Current-driven excitation of magnetic multilayers", Journal of Magnetism and Magnetic Materials **159**, L1–L7 (1996).

[4]L. Berger, "Emission of spin waves by a magnetic multilayer traversed by a current", Phys. Rev. B **54**, 9353–9358 (1996).

[5]M. Tsoi, A. G. M. Jansen, J. Bass, W.-C. Chiang, M. Seck, V. Tsoi, and P. Wyder, "Excitation of a magnetic multilayer by an electric current", Phys. Rev. Lett. **80**, 4281–4284 (1998).

[6]E. B. Myers, D. C. Ralph, J. A. Katine, R. N. Louie, and R. A. Buhrman, "Current-induced switching of domains in magnetic multilayer devices", Science **285**, 867–870 (1999).

[7]J. A. Katine, F. J. Albert, R. A. Buhrman, E. B. Myers, and D. C. Ralph, "Current-driven magnetization reversal and spin-wave excitations in co /cu /co pillars", Phys. Rev. Lett. **84**, 3149–3152 (2000).

[8]T. Kawahara, K. Ito, R. Takemura, and H. Ohno, "Spin-transfer torque {ram} technology: review and prospect", Microelectronics Reliability **52**, Advances in non-volatile memory technology, 613–627 (2012).

[9]I. S. Maksymov and M. Kostylev, "Broadband stripline ferromagnetic resonance spectroscopy of ferromagnetic films, multilayers and nanostructures", Physica E **69**, 253–293 (2015).

[10]P. Tekely, "Spin dynamics: basics of nuclear magnetic resonance", Magnetic Resonance in Chemistry **40**, 800–800 (2002).

[11]C. Kittel, "On the gyromagnetic ratio and spectroscopic splitting factor of ferromagnetic substances", Phys. Rev. **76**, 743–748 (1949).

[12]A. Aharoni, *Introduction to the theory of ferromagnetism*, International series of monographs on physics (Clarendon Press, 1996).

[13]J. Zhu, J. A. Katine, G. E. Rowlands, Y.-J. Chen, Z. Duan, J. G. Alzate, P. Upadhyaya, J. Langer, P. K. Amiri, K. L. Wang, and I. N. Krivorotov, "Voltage-induced ferromagnetic resonance in magnetic tunnel junctions", Phys. Rev. Lett. **108**, 197203 (2012).

[14]J. Slonczewski, "Currents and torques in metallic magnetic multilayers", J. Magn. Magn. Mater. **247**, 324–338 (2002).

[15]J. C. Slonczewski, "Currents, torques, and polarization factors in magnetic tunnel junctions", Phys. Rev. B **71**, 024411 (2005).

[16]J. Slonczewski and J. Sun, "Theory of voltage-driven current and torque in magnetic tunnel junctions", J. Magn. Magn. Mater. **310**, 169–175 (2007).

[17]M. Beleggia, M. D. Graef, Y. T. Millev, D. A. Goode, and G. Rowlands, "Demagnetization factors for elliptic cylinders", Journal of Physics D: Applied Physics **38**, 3333 (2005).

[18]R. G. Ayoub, "Paolo ruffini's contributions to the quintic", Archive for History of Exact Sciences **23**, 253–277 (1980).

[19]Z. Zeng, G. Finocchio, B. Zhang, P. K. Amiri, J. A. Katine, I. N. Krivorotov, Y. Huai, J. Langer, B. Azzerboni, K. L. Wang, and H. Jiang, "Ultralow-current-density and bias-field-free spin-transfer nano-oscillator", Sci. Rep. **3**, 1426 (2013).

[20]G. Bertotti, C. Serpico, I. D. Mayergoyz, A. Magni, M. d'Aquino, and R. Bonin, "Magnetization switching and microwave oscillations in nanomagnets driven by spin-polarized currents", Phys. Rev. Lett. **94**, 127206 (2005).

[21]M. Gmitra and J. Barna ś, "Current-driven destabilization of both collinear configurations in asymmetric spin valves", Phys. Rev. Lett. **96**, 207205 (2006).

[22]O. Boulle, V. Cros, J. Grollier, L. G. Pereira, C. Deranlot, G. Petroff F. Faini, J. Barnas, and A. Fert, "Shaped angular dependence of the spin-transfer torque and microwave generation without magnetic field", Nat. Phys. **3**, 492–497 (2007).

[23]Y. Zhou, S. Bonetti, C. L. Zha, and J. Akerman, "Zero-field precession and hysteretic threshold currents in a spin torque nano device with tilted polarizer", New J. Phys. **11**, 103028 (2009).

[24]K. Bernert, V. Sluka, C. Fowley, J. Lindner, J. Fassbender, and A. M. Deac, "Phase diagrams of mgo magnetic tunnel junctions including the perpendicular spin-transfer torque in different geometries", Phys. Rev. B **89**, 134415 (2014).

[25]C. Gonzalez-Fuentes, R. A. Gallardo, and P. Landeros, "Role of polarizer-tilting-angle in zero-field spin-transfer nano-oscillators with perpendicular anisotropy", Applied Physics Letters **107**, 142402 (2015) http://dx.doi.org/10.1063/1.4932548.

[26]K. Nakamura, R. Shimabukuro, Y. Fujiwara, T. Akiyama, T. Ito, and A. J. Freeman, "Giant modification of the magnetocrystalline anisotropy in transition-metal monolayers by an external electric field", Phys. Rev. Lett. **102**, 187201 (2009).

[27]K. Nakamura, R. Shimabukuro, T. Akiyama, T. Ito, and A. J. Freeman, "Origin of electric-field-induced modification of magnetocrystalline anisotropy at fe(001) surfaces: mechanism of dipole formation from first principles", Phys. Rev. B **80**, 172402 (2009).

[28]K. Nakamura, T. Akiyama, T. Ito, M. Weinert, and A. J. Freeman, "Role of an interfacial feo layer in the electric-field-driven switching of magnetocrystalline anisotropy at the fe/mgo interface", Phys. Rev. B **81**, 220409 (2010).

[29]T. Maruyama, Y. Shiota, T. Nozaki, K. M. Ohta, N. Toda, M. Mizuguchi, A. A. Tulapurkar, T. Shinjo, M. Shiraishi, S. Mizukami, Y. Ando, and Y. Suzuki, "Large voltage-induced magnetic anisotropy change in a few atomic layers of iron", Nat Nano **4**, 158–151 (2009).

[30]W.-G. Wang, M. Li, S. Hageman, and C. L. Chien, "Electric-field-assisted switching in magnetic tunnel junctions", Nat Mater **11**, 64–68 (2012).

[31]M. Endo, S. Kanai, S. Ikeda, F. Matsukura, and H. Ohno, "Electric-field effects on thickness dependent magnetic anisotropy of sputtered mgo/co40fe40b20/ta structures", Applied Physics Letters **96**, 212503 (2010) http://dx.doi.org/10.1063/1.3429592.

[32]A. A. Tulapurkar, Y. Suzuki, A. Fukushima, H. Kubota, H. Maehara, K. Tsunekawa, D. D. Djayaprawira, N. Watanabe, and S. Yuasa, "Spin-torque diode effect in magnetic tunnel junctions", Nature **438**, 339–342 (2005).

[33]J. C. Sankey, P. M. Braganca, A. G. F. Garcia, I. N. Krivorotov, R. A. Buhrman, and D. C. Ralph, "Spin-transfer-driven ferromagnetic resonance of individual nanomagnets", Phys. Rev. Lett. **96**, 227601 (2006).

[34]T. Nozaki, Y. Shiota, S. Miwa, S. Murakami, F. Bonell, S. Ishibashi, H. Kubota, K. Yakushiji, T. Saruya, A. Fukushima, S. Yuasa, T. Shinjo, and Y. Suzuki, "Electric-field-induced ferromagnetic resonance excitation in an ultrathin ferromagnetic metal layer", Nat. Phys. **8**, 491–496 (2012).

[35]J. C. Sankey, Y.-T. Cui, J. Z. Sun, J. C. Slonczewski, R. A. Buhrman, and D. C. Ralph, "Measurement of the spin-transfer-torque vector in magnetic tunnel junctions", Nat. Phys. **4**, 67–71 (2008).

[36]C. Wang, Y.-T. Cui, J. Z. Sun, J. A. Katine, R. A. Buhrman, and D. C. Ralph, "Bias and angular dependence of spin-transfer torque in magnetic tunnel junctions", Phys. Rev. B **79**, 224416 (2009).

[37]J. Sun and D. Ralph, "Magnetoresistance and spin-transfer torque in magnetic tunnel junctions", Journal of Magnetism and Magnetic Materials **320**, 1227–1237 (2008).

[38]N. Mecking, Y. S. Gui, and C.-M. Hu, "Microwave photovoltage and photoresistance effects in ferromagnetic microstrips", Phys. Rev. B **76**, 224430 (2007).

[39]J. C. Slonczewski, "Conductance and exchange coupling of two ferromagnets separated by a tunneling barrier", Phys. Rev. B **39**, 6995–7002 (1989).

[40]A. M. Sahadevan, K. Gopinadhan, C. S. Bhatia, and H. Yang, "Parallel-leaky capacitance equivalent circuit model for mgo magnetic tunnel junctions", Applied Physics Letters **101**, 162404 (2012) http://dx.doi.org/10.1063/1.4760279.

[41]M. A. Subramanian, R. D. Shannon, B. H. T. Chai, M. M. Abraham, and M. C. Wintersgill, "Dielectric constants of beo, mgo, and cao using the two-terminal method", Physics and Chemistry of Minerals **16**, 741–746 (1989).

[42]H. Kubota, A. Fukushima, K. Yakushiji, T. Nagahama, S. Yuasa, K. Ando, H. Maehara, Y. Nagamine, K. Tsunekawa, D. D. Djayaprawira, N. Watanabe, and Y. Suzuki, "Quantitative measurement of voltage dependence of spin-transfer torque in mgo-based magnetic tunnel junctions", Nat Phys **4**, 37–41 (2008).

[43]Y. Shiota, S. Miwa, S. Tamaru, T. Nozaki, H. Kubota, A. Fukushima, Y. Suzuki, and S. Yuasa, "Field angle dependence of voltage-induced ferromagnetic resonance under {dc} bias voltage", Journal of Magnetism and Magnetic Materials, (2015).

[44]B. Fang, M. Carpentieri, X. Hao, H. Jiang, J. A. Katine, I. N. Krivorotov, B. Ocker, J. Langer, K. L. Wang, B. Zhang, B. Azzerboni, P. K. Amiri, G. Finocchio, and Z. Zeng, "Giant spin-torque diode sensitivity in the absence of bias magnetic field", Nature Communications **7**, 11259 (2016).

[45]J. H. E. Griffiths, "Anomalous high-frequency resistance of ferromagnetic metals", Nature **158**, 670–671 (1946).

[46]M. Farle, "Ferromagnetic resonance of ultrathin metallic layers", Reports on Progress in Physics **61**, 755 (1998).

[47]J. M. Shaw, H. T. Nembach, T. J. Silva, and C. T. Boone, "Precise determination of the spectroscopic g-factor by use of broadband ferromagnetic resonance spectroscopy)", Journal of Applied Physics **114**, 243906 (2013) http://dx.doi.org/10.1063/1.4852415.

[48]C. Kittel, "On the theory of ferromagnetic resonance absorption", Phys. Rev. **73**, 155–161 (1948).

[49]J. P. Nibarger, R. Lopusnik, Z. Celinski, and T. J. Silva, "Variation of magnetization and the landé g factor with thickness in ni-fe films", Applied Physics Letters **83**, 93–95 (2003).

[50]S. Ikeda, K. Miura, H. Yamamoto, K. Mizunuma, H. D. Gan, M. Endo, S. Kanai, J. Hayakawa, F. Matsukura, and H. Ohno, "A perpendicular-anisotropy cofeb-mgo magnetic tunnel junction", Nat. Mater. **9**, 721–724 (2010).

[51]D.-T. Ngo, D.-T. Quach, Q.-H. Tran, K. Møhave, T.-L. Phan, and D.-H. Kim, "Perpendicular magnetic anisotropy and the magnetization process in cofeb/pd multilayer films", Journal of Physics D: Applied Physics **47**, 445001 (2014).

[52]D.-T. Ngo, Z. Meng, T. Tahmasebi, X. Yu, E. Thoeng, L. Yeo, A. Rusydi, G. Han, and K.-L. Teo, "Interfacial tuning of perpendicular magnetic anisotropy and spin magnetic moment in cofe/pd multilayers", Journal of Magnetism and Magnetic Materials **350**, 42–46 (2014).

[53]Y. Tserkovnyak, A. Brataas, and G. E. W. Bauer, "Spin pumping and magnetization dynamics in metallic multilayers", Phys. Rev. B **66**, 224403 (2002).

[54]J. Foros, G. Woltersdorf, B. Heinrich, and A. Brataas, "Scattering of spin current injected in pd(001)", Journal of Applied Physics **97** (2005) http://dx.doi.org/10.1063/1.1853131.

[55]A. Berger and M. R. Pufall, "Generalized magneto-optical ellipsometry", Applied Physics Letters **71**, 965–967 (1997).

[56]A. Berger and M. R. Pufall, "Quantitative vector magnetometry using generalized magneto-optical ellipsometry", Journal of Applied Physics **85**, 4583–4585 (1999).

[57]K. Mok, N. Du, and H. Schmidt, "Vector-magneto-optical generalized ellipsometry", Review of Scientific Instruments **82**, 033112, 1–9 (2011).

[58]G. Neuber, R. Rauer, J. Kunze, T. Korn, C. Pels, G. Meier, U. Merkt, J. Bäckström, and M. Rübhausen, "Temperature-dependent spectral generalized magneto-optical ellipsometry", Applied Physics Letters **83**, 4509–4511 (2003).

[59]R. Rauer, G. Neuber, J. Kunze, J. Bäckström, and M. Rübhausen, "Temperature-dependent spectral generalized magneto-optical ellipsometry for ferromagnetic compounds", Review of Scientific Instruments **76**, 023910, (2005).

[60]J. A. Arregi, J. B. Gonzalez-Diaz, E. Bergaretxe, O. Idigoras, T. Unsal, and A. Berger, "Study of generalized magneto-optical ellipsometry measurement reliability", Journal of Applied Physics **111**, 103912, (2012).

[61]J. González-Díaz, J. Arregi, E. Bergaretxe, M. Fertin, O. Idigoras, and A. Berger, "Anomalous magneto-optical behavior of uniaxial co/coo bilayer films", Journal of Magnetism and Magnetic Materials **325**, 147–151 (2013).

[62]T. E. Jenkins, "Multiple-angle-of-incidence ellipsometry", Journal of Physics D: Applied Physics **32**, R45 (1999).

[63]A. Zvezdin and V. Kotov, *Modern magnetooptics and magnetooptical materials*, Condensed Matter Physics (Taylor & Francis, 1997).